North Carolina State University

Final Technical Report:

Device Design and Periodic Motion Control of an Ocean Kite System for Hydrokinetic Energy Harvesting

Principal Investigators:

Chris Vermillion – Associate Professor (NC State)
Kenneth Granlund – Associate Professor (NC State)
Andre Mazzoleni – Professor (NC State)
Hosam Fathy – Professor (University of Maryland)
Mike Muglia – Research Assistant Professor (East Carolina University/Coastal Studies Institute)
Gabriel Alsenas – Director (Florida Atlantic Univ. SE National Marine Renewable Energy Ctr.)

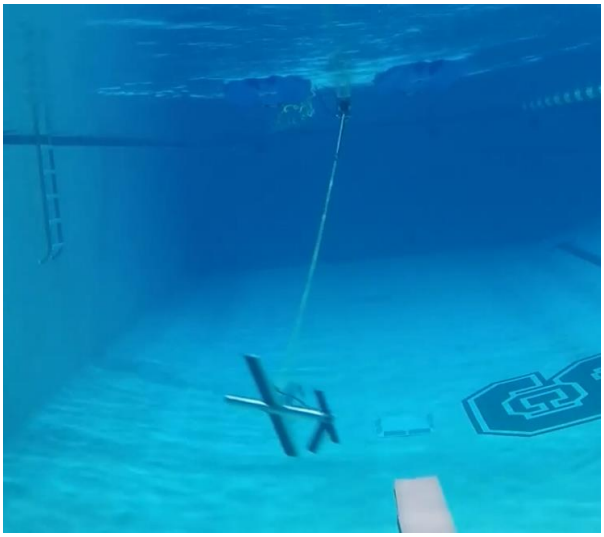

Acknowledgment:
This material is based upon work supported by the U.S. Department of Energy's Office of Energy Efficiency and Renewable Energy (EERE) under the Water Power Technologies Office (WPTO) Award Number DE-EE0008635.

Executive Summary

This project focused on the modeling, device design, control system design, and progressive experimental validation of an energy-harvesting underwater kite harvesting energy through cyclic spooling motion. This adds to the portfolio of the DoE Water Power Technologies Office has resulted in several key outcomes that will further the development of energy-harvesting kites:

- The team has developed a detailed, open-source kite dynamic model that characterizes both the flight behavior and techno-economic performance projections for the kite, which were evaluated extensively throughout the project. The model can characterize kites that are deployed off of either seabed or floating platforms, in the presence of waves (which impact the floating platform) and turbulence.
- The team has developed flight control strategies for following a prescribed flight path and angle of attack profile using control surfaces on-board the kite.
- The team has developed cyclic optimal control strategies, most notably leveraging economic iterative learning control, for optimally modulating the kite's flight path, angle of attack profile, and spooling speed profile over the course of operation. The team has developed both decoupled (where each of the three aforementioned goals is treated separately) and coupled variants for accomplishing optimization of the kite's flight path, angle of attack profile, and spooling speed profile, with the latter being restricted to work off a simplified model at present.
- The team has validated its dynamic model and iterative learning control strategies at three experimental scales – very small-scale water channel testing (dynamic model only with a simple tether-based control strategy), pool-based scaled tow testing (dynamic model and flight controller, with no online optimization via iterative learning), and open-water scaled tow testing (full validation of the dynamic model, flight controller, and iterative learning-based optimization).
- The team has utilized its model and control strategies to perform a combined device, control, and site selection co-design, which resulted in techno-economic projections for several candidate tidal and current deployments.
- The team has engaged in a technology-to-market effort that has resulted in initial discussions with Minesto, Ltd. and a multi-million dollar follow-on project with PacMar Technologies, the latter of which focuses on the Blue Economy application of using underwater kites to recharge an autonomous underwater vehicle when a vehicle is parked at the seabed.

Based on the results of the project, kite technology has the capability of delivering marine hydrokinetic energy for under $0.10/kWh in appropriately selected ocean current sites from an existing floating platform, in addition to delivering energy at approximately $0.10/kWh for appropriate remote tidal sites. Kite technology also is projected to yield levelized cost of energy below $0.15/kWh for deep-water seabed deployments in appropriate Gulf Stream sites. By comparison, the DoE Reference Model 4 Ocean Current Turbine was projected to have a levelized cost of energy of approximately $0.25/kWh for a similar site [1], and most tidal and ocean current turbines are projected to have levelized costs significantly exceeding $0.15/kWh. This is further discussed in the detailed techno-economic analyses within the report. These projections are based on the design pursued in this project effort. However, several lessons learned throughout the project effort points to design improvements that can further improve the techno-economic prospects for kite technology. Detailed in the body of the report, these lessons learned are briefly summarized here:

- Improvements in generator and motor efficiency via a direct drive system are critical for economical full-scale implementation. These improvements, if substantial, can significantly reduce costs of energy through an increase in annual energy production that outweighs any corresponding increase in capital expenses. Alternatively, mechanisms such as flywheels for short-term mechanical energy storage to power the spool-in phase of operation, are highly desirable in order to avoid regular switching between motoring and generation.
- Because of stricter-than-expected structural requirements (in particular, relating to required safety factors) on the tether, tether drag played a more pronounced role than expected in kite performance projections. This is particularly true on very long tethers (even if those tethers contain a substantial faired portion), which are necessarily the case with seabed deployments in deep waters. The optimal design and control strategies on a long, "draggy" tether differ from the optimal design and control strategies for a short tether. This is because tether drag begins to dominate kite drag on long tethers, demanding an emphasis on pure lift, rather than efficiency, in the kite design. The team has explored the performance implications of morphing designs, which can adjust the kite geometry based on the tether length and flow speed, and these performance implications are discussed in detail in the body of the report.

In addition to lessons learned that if appropriately addressed in future work will further improve techno-economic performance, a third lesson learned relates to the limitations of scaled testing. While the team stands by its progressive scaled testing approach, the team also initially overestimated the amount by which very small-scale test results could extrapolate to full-scale behavior (which had been validated to an extent in the team's prior work in [2] but had only been validated at different lab scales). On one hand, the very small-scale results acted as an excellent platform for model validation and diagnostics. On the other hand, size limitations mean that geometric sacrifices must be made in order to accommodate all of the electronics, thereby limiting performance relative to that of a full-scale system.

Contents

1 Underwater Kites: How and Why?

The core goal of underwater kite operation is to harness a very substantial amount of power using very little material. A basic understanding of how this is possible is important to identifying (i) the key design and control challenges that must be addressed and (ii) the circumstances under which underwater kite systems serve as a viable alternative or complement to stationary tidal and ocean current turbines. While the literature outlining the basic functionality, detailed modeling, and detailed control design of energy-harvesting kites (see [3] for a review from an airborne wind energy perspective, noting that airborne kites follow the same basic principles of operation as underwater kites) is vast, we summarize some basic concepts here before delving into the technical details of the work.

Central to the operation of underwater (or airborne) kites is the principle of ***cross-current motion***. This is illustrated in a top-down view in Figure 1, for the simple case where the kite is not being spooled in or out and where the tether is parallel to the ground plane. In a quasi-static scenario, where the kite is directly down-current and is neither accelerating nor decelerating, the resolved fluid dynamic forces on the kite must align with the tether (otherwise, there would be a component of force either accelerating or decelerating the kite). Given that lift is (by definition) perpendicular to the apparent flow velocity and drag is (by definition) parallel to the apparent flow velocity, the ratio of a kite's achievable velocity to the flow velocity is equal to the ratio of its lift to drag in a quasi-static case when the kite is directly downwind (or down-current in the ocean). The consequence of this fact is that even relatively modest lift-to-drag ratios can allow kites to fly much faster than the prevailing flow.

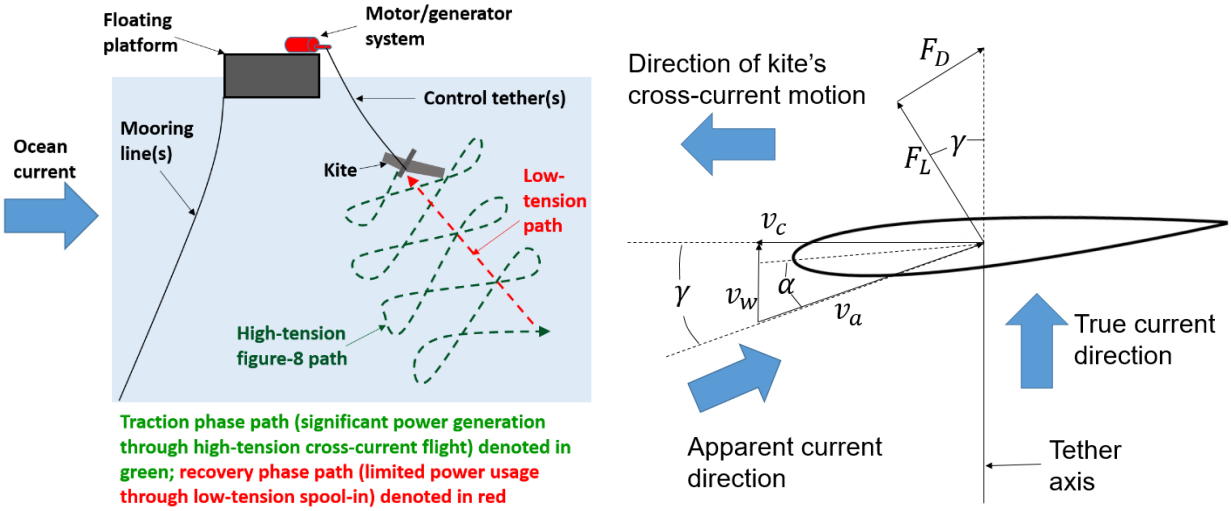

Figure 1: Kite concept of operations under cyclic spooling (left) and diagram illustrating key velocity and force vectors at play in a quasi-static case (right).

A natural follow-on question is: How does the high speed that kites are capable of translate into power generation? To answer that question, one must consider possible modes of power generation. In general, there are two available modes: on-board generators and cyclic spooling. In the first mode of power generation, small turbines on-board the kite harvest energy, which is converted to AC power (and sometimes transformed and rectified, such that high-voltage DC power can be transmitted down the cable) and transmitted down a conductive tether. In the second mode, power is generated by spooling tether out under high tension, under cross-current kite motion, then spooling tether in under very low

tension. Because it eliminates all of the rotating machinery required for the first mode of power generation, we have focused on the second mode of power generation in this work. As it turns, out, in the limit, both modes of power generation yield the same theoretical available power output, which can be derived from the basic principles in Figure 1 (for a detailed derivation and discussion, see [3]) and is given by:

$$P = \frac{2}{27}\rho v_{flow}^3 A \frac{C_L^3}{C_D^2}(\cos\theta)^3(\cos\phi)^3$$

where ρ, v_{flow}, A, C_L, C_D, θ, and ϕ refer to the fluid density, flow speed, common reference area, aggregate lift coefficient, aggregate drag coefficient (including the contribution of the tether and fuselage), elevation angle (between the horizontal plane and tether; effectively the latitude that the kite is flying at on an imaginary sphere with radius defined by the tether length) and azimuth angle (the longitude on that imaginary sphere). From this expression alone, several conclusions become apparent:

- It is critical to employ a ***design*** with high lift and low drag, as well as a ***control system*** that maintains the kite's attitude in such a way that these features are realized in dynamic flight;
- The position of the kite in spherical coordinates is critical to its power output.
- Both the flow speed ***and*** tether length (the latter of which impacts C_D) are important to performance, and they should be considered together in site selection for any system deployed off the seabed.

Furthermore, the aforementioned performance equation is derived based on a quasi-static analysis, which indicates the level of power that is achievable but does not indicate how to design a controller to achieve that level of power. Furthermore, a detailed investigation into the derivation of the power equation will reveal that it makes highly simplifying assumptions, such as an idealized rotor in the on-board rotor case and infinite spool-in speeds in the cyclic spooling case. Given the impracticality of these (particularly the latter), it is critical to design real-time optimal control strategies that maximize power output and get as close to this theoretical limit as possible, taking into account the more detailed realities of the kite's dynamics. In the following chapters, we describe our team's efforts to address these needs.

2 System Modeling

2.1 Dynamic Model Overview

As a precursor to the extension of its dynamic modeling tools, the team refined its existing kite geometry, scaled the geometry to produce a peak power output of 100 kW at approximately 1.4 m/s flow speed, and characterized the hydrodynamics of the lifting body using XFLR-5. Model validation and associated simulations were based on the kite of **Figure 2**, with key design parameters indicated in **Table 1**. The kite employs an aircraft design (consistent with the original proposal) with standard control surfaces, namely ailerons, elevators, and a rudder. The tether is attached to a rigid bridle. This kite design is scalable for the purposes of smaller-scale testing, to the extent that the physical dimensions are sufficient for packaging. For example, in the very small-scale water channel-based testing (approximately 1/100-scale), it is impossible to package control surfaces and associated actuators into the models – thus, water channel testing focused on model validation using tethers for actuation, thereby preventing a validation of the control system at that scale. Furthermore, 1/10-scale pool-based and lake testing required an enlarged

fuselage to accommodate all of the electronics but did enable the incorporate of control surfaces for the validation of the team's control designs.

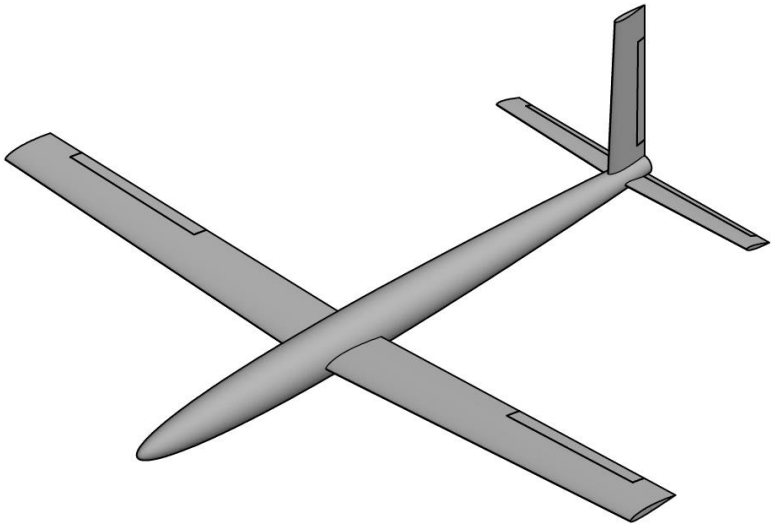

Figure 2: Kite geometry for use in model evaluation/validation.

Design parameter	**Value**
Fuselage length	8m
Wing dimensions	10m span x 1m chord
Horizontal stabilizer dimensions	4m span x 0.5m chord
Vertical stabilizer dimensions	2m span x 0.5m chord
Mass	945kg
Theoretical peak steady-state power output at 1.5 m/s	126kW
Presently attained (un-optimized) average power output at 1.5 m/s	38.6kW
Presently attained (un-optimized) peak power output at 1.5 m/s	122kW

Table 1: Kite design parameters for initial hydrodynamic and dynamic modeling studies. Parameters have been refined over the course of the design process.

In performing the hydrodynamic characterization, the kite was partitioned into four components: the wing (modeled as two separate surfaces in order to account for roll damping), horizontal stabilizer, vertical stabilizer, and fuselage. Lift and drag coefficients for each surface were characterized as a function of that surface's local angle of attack. The fuselage simply contributes a single parasitic drag to the overall kite. Within the dynamic model, these forces are aggregated to compute the net forces and moments (using the component forces and the corresponding moment arms).

In the original proposal, the team performed initial simulation studies and techno-economic performance estimates based on a relatively simple dynamic model, termed the *unifoil model*, which makes the following simplifying assumptions:

- The tether is modeled as a rigid kinematic link of controllable length.

- The kite is constrained to move in the direction that it is pointing. This no-slip assumption is commonly referred to as a "unicycle" assumption.

While this model provided a basis for initial estimates of the performance that *could* be achieved, the reasonableness of the above assumptions is highly dependent on the design and the flight control system. In order to provide an accurate prediction of how the design and flight control system will behave when the kite is actually implemented, it is essential that the team move to a higher-fidelity six degree-of-freedom kite model as part of its development process. **During the first project quarter, the team developed a modular dynamic modeling environment with a six degree-of-freedom kite model, along with a corresponding path-following flight controller, which has so far been evaluated under constant flow conditions consistent with those specified in Milestone 1.2.1**.

Dynamic model structure:

The dynamic model consists of three main modules:

- The platform, which can be a fixed platform on the seabed or a floating platform. Inputs to the model include, at minimum, the tether tension vector. For the floating platform model, the dynamics are also driven by the current and wave resource. The model predicts the orientation and position of the platform, which in turn provides the locations of the tether attachment points relative to the ground coordinate system.
- The tether(s). Note that while the target design includes a single tether, the model can also account for multiple tethers. This has been critically important for comparing the model output against data from water channel testing, where for aforementioned practical reasons it was impossible to instrument the kite with control surfaces (and tethers needed to be used for actuation). The tethers are modeled using a lumped mass approach, where each tether is modeled as a series of spring-damper links and nodal masses. All hydrodynamic drag and gravitational forces are applied at the nodes. The tether model receives attachment point locations as inputs from the platform and kite model, and outputs tension vectors at both the base and the attachment to the kite.
- The kite, which is a six degree-of-freedom rigid aircraft model whose hydrodynamic parameters have been determined based on the aforementioned XFLR-5 analysis. Inputs to the kite model include the tether tensions(s), control surface deflections, and current profile. The kite model predicts three-dimensional position, orientation (Euler angles), velocities, and angular velocities.

The dynamic model has been implemented in a Simulink environment, which enables (i) graphical in-simulation diagnostic capabilities, (ii) straightforward integration of new control designs into the modeling environment, and (iii) modularity through the use of variant subsystems. Because of the clearly defined interface between the three components of the model, it is quite straightforward to plug and play different platform models (e.g., floating or fixed), tether models (e.g., lumped mass vs. PDE models), and kite models into the simulation. Furthermore, the model features one-click dynamic scaling, based on dimensional analysis for predicting behavior at different scales (see [2], [4]), including the water channel scale that was be used in Task 5 for dynamic model validation.

2.2 Kite Hydrodynamic Characterization

In performing the hydrodynamic characterization, the kite is partitioned into four components: the wing (modeled as two separate surfaces in order to account for roll damping), horizontal stabilizer, vertical

stabilizer, and fuselage. The fuselage simply contributes a single parasitic drag to the overall kite. Lift and drag coefficients for each surface have been characterized using three different analysis software, the capabilities and limitations of which are listed below:

1. XFOIL, which is a 2D airfoil analysis software accounts for viscous effects and accounts for stall behavior but does not characterize induced drag effects.
2. AVL uses an inviscid tool for the analysis of 3D aerodynamic surfaces, which accounts for induced drag effects but does characterize viscous effects.
3. XFLR5 combines the features of XFOIL and AVL, providing the most accurate hydrodynamic characterization but requires comparatively more person-hours for setting up and running the analysis for any given surface geometry.

Owing to the benefits and drawbacks outlined above, the team elected to move to using XFLR5 to compute the hydrodynamic coefficients to use the more accurate characterization. The hydrodynamic coefficients of the kite (C_L and C_D) were characterized using XLFR5 as a reference software. XFLR5 has capabilities to simulate 3-D aircraft bodies while considering viscous effects, a feature absent in previously used software, AVL. This characterization was accomplished by determining a parametric fit for the lift and drag curves by running a batch analysis of wings with various aspect ratios (AR). The parameterized equations for lift and drag are as follows:

$$C_{Li} = C_{Lai} \cdot \alpha + C_{L0} \; ; \; C_{Lai} = \frac{2\pi\gamma_i}{1+\frac{2\pi\gamma_i}{\pi \cdot e_i \cdot AR}}$$

$$C_D = \left(\frac{1}{\pi e_{D,i} \cdot AR} + K_{visc}\right) \cdot (C_{L,i} - C_{LD,i})^2 + C_{D0,i}$$

where the parameters marked in red are empirical values that vary with flight conditions, airfoil geometry and 3-D shape of the craft. These parameters were tuned to best fit our flight conditions and geometry. Figure 3 compares the lift and drag curves obtained from the parametric model and XFLR post fitting:

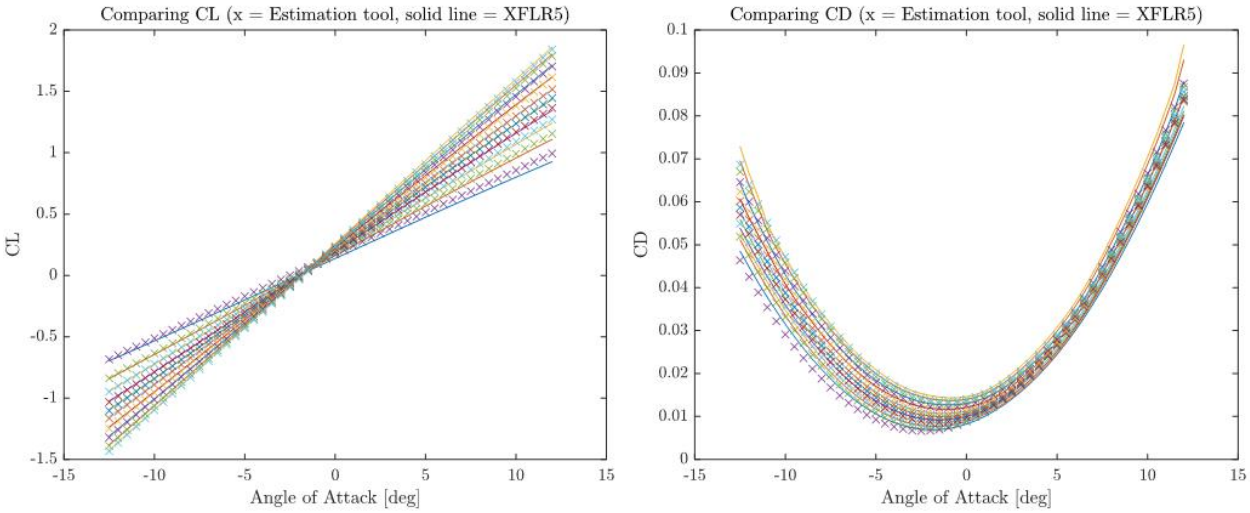

Figure 3: Lift and drag curves obtained from the co-design tool (estimation tool) and XFLR for 10 aspect ratios varying from 4 to 25.

In addition to using XFLR-5 to characterize steady hydrodynamic parameters, the team also refined the added mass characterization within its dynamic model, in particular developing elegant code that computes the 6x6 added mass/inertia matrix for the kite and corresponding Coriolis terms, using strip theory. A detailed description of this formulation is given here.

Define the hydrodynamic force in the X/Y/Z direction of the body frame due to the apparent mass effect as $X_A/Y_A/Z_A$ and the moment about the X/Y/Z axis as $K_A/M_A/N_A$. Then define the hydrodynamic derivatives as the contribution to the apparent mass force/moment in each body direction due to the body-frame acceleration. More formally, the added mass matrix is defined as:

$$\boldsymbol{M_A} = -\begin{bmatrix} X_{\dot{u}} & X_{\dot{v}} & X_{\dot{w}} & X_{\dot{p}} & X_{\dot{q}} & X_{\dot{r}} \\ Y_{\dot{u}} & Y_{\dot{v}} & Y_{\dot{w}} & Y_{\dot{p}} & Y_{\dot{q}} & Y_{\dot{r}} \\ Z_{\dot{u}} & Z_{\dot{v}} & Z_{\dot{w}} & Z_{\dot{p}} & Z_{\dot{q}} & Z_{\dot{r}} \\ K_{\dot{u}} & K_{\dot{v}} & K_{\dot{w}} & K_{\dot{p}} & K_{\dot{q}} & K_{\dot{r}} \\ M_{\dot{u}} & M_{\dot{v}} & M_{\dot{w}} & M_{\dot{p}} & M_{\dot{q}} & M_{\dot{r}} \\ N_{\dot{u}} & N_{\dot{v}} & N_{\dot{w}} & N_{\dot{p}} & N_{\dot{q}} & N_{\dot{r}} \end{bmatrix} = \begin{bmatrix} \boldsymbol{M_{A,T}} & \boldsymbol{M_{A,TR}} \\ \boldsymbol{M_{A,RT}} & \boldsymbol{M_{A,R}} \end{bmatrix}$$

where $X_{\dot{u}} = \frac{\partial X_A}{\partial \dot{u}}$, $X_{\dot{v}} = \frac{\partial X_A}{\partial \dot{v}}$, etc. and u, v, w, p, q, and r are the coefficients of the linear and angular velocity vectors expressed in the body frame. Assuming the hydrodynamic derivatives are constant, the added mass matrix may be combined with the inertia matrix in the state equations. Because we are working in the body frame, an additional matrix is necessary to describe the Coriolis-centripetal terms in the force and moment expressions. The Coriolis-centripetal added mass matrix may be computed directly from the hydrodynamic derivatives in the same way that the rigid body Coriolis-centripetal matrix may be computed from the mass and inertia.

Computing added mass coefficients: There are several methods that may be employed to compute values for the hydrodynamic derivatives. The underwater kite may be represented by a composition of slender bodies, which led to the team's choice of strip theory as the method of choice for computing added mass coefficients.

The acceleration of a two-dimensional section located by point a in body frame $\bar{B}$ may be written as:

$${}^{\bar{O}}\vec{a}_{a/O} = {}^{\bar{B}}\vec{a}_{a/O} + {}^{\bar{O}}\vec{\omega}^{\bar{B}} \times {}^{\bar{O}}\vec{v}_{B/O} + {}^{\bar{O}}\vec{\alpha}^{\bar{B}} \times \vec{r}_{a/B} + {}^{\bar{O}}\vec{\omega}^{\bar{B}} \times \left({}^{\bar{O}}\vec{\omega}^{\bar{B}} \times \vec{r}_{a/B}\right)$$

where, in matrix notation:

$$\left\{\vec{r}_{a/B}\right\}_{\bar{B}} = \begin{bmatrix} x_a \\ y_a \\ z_a \end{bmatrix}$$

$$\left\{{}^{\bar{B}}\vec{a}_{B/O}\right\}_{\bar{B}} = \begin{bmatrix} \dot{u} \\ \dot{v} \\ \dot{w} \end{bmatrix}$$

$$\left\{{}^{\bar{O}}\vec{\alpha}^{\bar{B}}\right\}_{\bar{B}} = \begin{bmatrix} \dot{p} \\ \dot{q} \\ \dot{r} \end{bmatrix}$$

Then the inertial linear acceleration of the section expressed in the section frame is:

$$\left\{{}^{\bar{O}}\vec{a}_{a/O}\right\}_{\bar{a}} = {}^{\bar{a}}[C]^{\bar{B}}\left\{{}^{\bar{O}}\vec{a}_{a/O}\right\}_{\bar{B}}$$

Likewise, the inertial angular acceleration expressed in the section frame is:

$$\left\{{}^{\bar{O}}\vec{\alpha}^{\bar{B}}\right\}_{\bar{a}} = {}^{\bar{a}}[C]^{\bar{B}}\left\{{}^{\bar{O}}\vec{\alpha}^{\bar{B}}\right\}_{\bar{B}}$$

Combine these into a single expression by defining a 6x6 rotation matrix

$${}^{\bar{a}}[R]^{\bar{B}} = \begin{bmatrix} {}^{\bar{a}}[C]^{\bar{B}} & \mathbf{0_3} \\ \mathbf{0_3} & {}^{\bar{a}}[C]^{\bar{B}} \end{bmatrix}$$

where $\mathbf{0_3}$ is a 3x3 zero matrix. Then

$$\begin{bmatrix} \left\{{}^{\bar{O}}\vec{a}_{a/O}\right\}_{\bar{a}} \\ \left\{{}^{\bar{O}}\vec{\alpha}^{\bar{B}}\right\}_{\bar{a}} \end{bmatrix} = {}^{\bar{a}}[R]^{\bar{B}} \begin{bmatrix} \left\{{}^{\bar{O}}\vec{a}_{a/O}\right\}_{\bar{B}} \\ \left\{{}^{\bar{O}}\vec{\alpha}^{\bar{B}}\right\}_{\bar{B}} \end{bmatrix}$$

In slender-body strip theory, the apparent mass loads per unit length of a section are related to the acceleration in the section plane by the section added mass matrix.

$$\boldsymbol{a_A} = -\begin{bmatrix} 0 & 0 & 0 & 0 & 0 & 0 \\ 0 & a_{22} & a_{23} & a_{24} & 0 & 0 \\ 0 & a_{32} & a_{33} & a_{34} & 0 & 0 \\ 0 & a_{42} & a_{43} & a_{44} & 0 & 0 \\ 0 & 0 & 0 & 0 & 0 & 0 \\ 0 & 0 & 0 & 0 & 0 & 0 \end{bmatrix} = \begin{bmatrix} \boldsymbol{a_A^{11}} & \boldsymbol{a_A^{12}} \\ \boldsymbol{a_A^{21}} & \boldsymbol{a_A^{22}} \end{bmatrix}$$

The added mass coefficients for a slender body may be computed by integrating the contributions of each section over the length of the slender body. Typically, the section and slender body frames are chosen such that the axis along the length of the body is coincident with the axis that is normal to the section plane so that the kinematics of the section as the result of body motion are easily intuited. However, to combine multiple slender bodies into one composite body it is necessary to relax the conventional colocation of the body long axis and the section normal axis. In matrix form, the force per unit length of the section due to a unit acceleration may be written as:

$$\begin{bmatrix} \left\{\vec{f}_a\right\}_{\bar{a}} \\ \left\{\vec{\tau}_a\right\}_{\bar{a}} \end{bmatrix} = \boldsymbol{a_A} \begin{bmatrix} \left\{{}^{\bar{O}}\vec{a}_{a/O}\right\}_{\bar{a}} \\ \left\{{}^{\bar{O}}\vec{\alpha}^{\bar{B}}\right\}_{\bar{a}} \end{bmatrix} = \boldsymbol{a_A}\,{}^{\bar{a}}[R]^{\bar{B}} \begin{bmatrix} \left\{{}^{\bar{O}}\vec{a}_{a/O}\right\}_{\bar{B}} \\ \left\{{}^{\bar{O}}\vec{\alpha}^{\bar{B}}\right\}_{\bar{B}} \end{bmatrix}$$

The total hydrodynamic force on the body due to the apparent mass is then the summation over all of the constituent sections of the force per unit length times the differential length of each section. In order to sum these contributions, they must be converted to the body frame:

$$\begin{bmatrix} \left\{\vec{F}_A\right\}_{\bar{B}} \\ \left\{\vec{\mathrm{T}}_A\right\}_{\bar{B}} \end{bmatrix} = \begin{bmatrix} X_A \\ Y_A \\ Z_A \\ K_A \\ M_A \\ N_A \end{bmatrix} = \sum_{i=1}^{N} {}^{\bar{B}}[R]^{\bar{a}_i} \begin{bmatrix} \left\{\vec{f}_{a_i}\right\}_{\bar{a}_i} \\ \left\{\vec{\tau}_{a_i}\right\}_{\bar{a}_i} \end{bmatrix} \Delta l + \begin{bmatrix} 0 \\ \left\{\vec{r}_{a_i/B}\right\}_{\bar{B}} \times {}^{\bar{B}}[C]^{\bar{a}_i}\left\{\vec{f}_{a_i}\right\}_{\bar{a}_i} \end{bmatrix} \Delta l$$

$$= {}^{\bar{B}}[R]^{\bar{a}_i}\boldsymbol{a_A}\,{}^{\bar{a}_i}[R]^{\bar{B}} \begin{bmatrix} \left\{{}^{\bar{O}}\vec{a}_{a_i/O}\right\}_{\bar{B}} \\ \left\{{}^{\bar{O}}\vec{\alpha}^{\bar{B}}\right\}_{\bar{B}} \end{bmatrix} \Delta l_i$$

where N is the number of sections. It may be easier to conceptualize as two equations, one for force and one for torque. To do that, we divide the 6x6 section added mass matrix into four 3x3 matrices.

$$\{\vec{f}_a\}_{\bar{a}} = \boldsymbol{a_A^{11}}\{^{\bar{O}}\vec{a}_{a/O}\}_{\bar{a}} + \boldsymbol{a_A^{12}}\{^{\bar{O}}\vec{\alpha}^{\bar{B}}\}_{\bar{a}}$$

$$\{\vec{\tau}_a\}_{\bar{a}} = \boldsymbol{a_A^{21}}\{^{\bar{O}}\vec{a}_{a/O}\}_{\bar{a}} + \boldsymbol{a_A^{22}}\{^{\bar{O}}\vec{\alpha}^{\bar{B}}\}_{\bar{a}}$$

Then

$$\{\vec{F}_A\}_{\bar{B}} = \sum_{i=1}^{N} {}^{\bar{B}}[C]^{\bar{a}_i}\,\boldsymbol{a_A^{11\bar{a}_i}}[C]^{\bar{B}}\{^{\bar{O}}\vec{a}_{a_i/O}\}_{\bar{B}}\Delta l_i + {}^{\bar{B}}[C]^{\bar{a}_i}\boldsymbol{a_A^{12\bar{a}_i}}[C]^{\bar{B}}\{^{\bar{O}}\vec{\alpha}^{\bar{B}}\}_{\bar{B}}\Delta l_i$$

$$\{\vec{\mathrm{T}}_A\}_{\bar{B}} = \sum_{i=1}^{N} {}^{\bar{B}}[C]^{\bar{a}_i}\,\boldsymbol{a_A^{21\bar{a}}}[C]^{\bar{B}}\{^{\bar{O}}\vec{a}_{a/O}\}_{\bar{B}}\Delta l_i + {}^{\bar{B}}[C]^{\bar{a}_i}\boldsymbol{a_A^{22\bar{a}}}[C]^{\bar{B}}\{^{\bar{O}}\vec{\alpha}^{\bar{B}}\}_{\bar{a}}\Delta l_i + \{\vec{r}_{a_i/B}\}_{\bar{B}}$$
$$\times\, {}^{\bar{B}}[C]^{\bar{a}_i}\boldsymbol{a_A^{11\bar{a}_i}}[C]^{\bar{B}}\{^{\bar{O}}\vec{a}_{a_i/O}\}_{\bar{B}}\Delta l_i + \{\vec{r}_{a_i/B}\}_{\bar{B}} \times {}^{\bar{B}}[C]^{\bar{a}_i}\boldsymbol{a_A^{12\bar{a}_i}}[C]^{\bar{B}}\{^{\bar{O}}\vec{\alpha}^{\bar{B}}\}_{\bar{B}}\Delta l_i$$

For a symmetric section, $\boldsymbol{a_A^{12}} = \boldsymbol{a_A^{21}} = \boldsymbol{0_3}$ and the hydrodynamic force due to apparent mass reduces to:

$$\{\vec{F}_A\}_{\bar{B}} = \sum_{i=1}^{N} {}^{\bar{B}}[C]^{\bar{a}_i}\,\boldsymbol{a_A^{11\bar{a}}}[C]^{\bar{B}}\{^{\bar{O}}\vec{a}_{a/O}\}_{\bar{B}}\Delta l_i$$

Likewise, the hydrodynamic moment reduces to:

$$\{\vec{\mathrm{T}}_A\}_{\bar{B}} = \sum_{i=1}^{N} {}^{\bar{B}}[C]^{\bar{a}_i}\,\boldsymbol{a_A^{22\bar{a}}}[C]^{\bar{B}}\{^{\bar{O}}\vec{\alpha}^{\bar{B}}\}_{\bar{a}}\Delta l_i + \{\vec{r}_{a_i/B}\}_{\bar{B}} \times {}^{\bar{B}}[C]^{\bar{a}_i}\boldsymbol{a_A^{11\bar{a}}}[C]^{\bar{B}}\{^{\bar{O}}\vec{a}_{a/O}\}_{\bar{B}}\Delta l_i$$

Finally, from the definition of the added mass matrix, we can take the partial derivative of each body force component with respect to each body frame acceleration coefficient to determine the expressions for the elements of the added mass matrix.

2.3 Tether Characterization

The tethers are modeled using a lumped mass approach, where each tether is modeled as a series of spring-damper links and nodal masses and accounts for hydrodynamic drag and gravitational forces which are applied at the nodes. Note that while the target design includes a single tether, the model can also account for multiple tethers which allows for simulations representative of the water channel environment where three tethers are used for closed-loop control.

Alternatively, the team has developed a three-dimensional continuum mechanics-based model of the tether model and implemented model order reduction techniques to further simplify the model to strike a balance between fidelity and complexity. This model has been tested under several scenarios and has been included as a variant in the team's integrated Simulink model.

2.4 Flow Models

The goal of the flow model within the environmental module of the overall Simulink model is to characterize the local flow velocity at each spatial point in the kite's domain, at each time instant. This

requires the superposition of low-frequency models with high-frequency turbulence characterization. To do this, the model fuses flow speed characterizations from two sources:

- *Low-frequency ADCP or hind cast model:* ADCP data made available by PI Mike Muglia provides flow speeds at 4m spatial resolution and 10-minute temporal resolution for one fixed location along the Gulf Stream transect. Alternatively, the Mid Atlantic Bight (MAB), South Atlantic Bight (SAB) Regional Ocean Modeling system (RCM), termed the MAB-SAB-RCMs model, characterizes the flow resource at 42 locations along a Gulf Stream transect, at 1-hour temporal intervals, with a spatial resolution of 25 meters. The hindcasting mechanism used for the MAB-SAB-RCMs model is fundamentally similar to the Coupled Northwest Atlantic Prediction System (CNAPS) model developed by Ruoying He's group and suggested in the original proposal; however, the MAB-SAB-RCMs data is available in a much more accessible form for use by the team. In all simulations, **either** the ADCP data **or** the MAB-SAB-ROMs model is used to generate low-frequency spatiotemporally varying flow, which in turn drives the dynamic simulation. The benefit of the ADCP data is that it consists of real measurements, not just a model. However, because it is only available at a single location and is not valid near the surface (due to surface reflections), MAB-SAB-RCMs data is used to supplement ADCP data. Example MAB-SAB-RCMs model output is shown in Figure 4 (left).
- *Higher-frequency spectral turbulence modeling:* The team has leveraged a spectral turbulence model developed at Florida Atlantic University [5], which outputs a spatiotemporally varying 3-dimensional turbulent velocity profile based on a prescribed turbulence intensity and mean flow velocity.

The result of the fused low-frequency/high-frequency spatiotemporal flow environment model is a look-up table that outputs the flow velocity vector at any time (t) and spatial location in the $y-z$ plane (the plane perpendicular to the prevailing flow), as depicted in Figure 4.

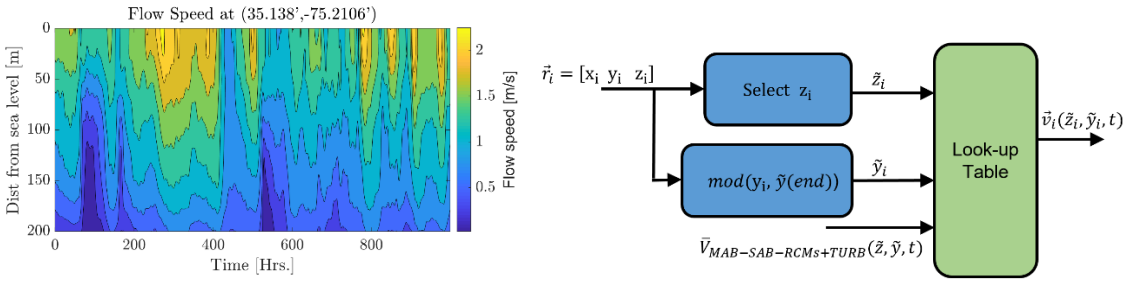

Figure 4: Sample MAB-SAB-RCMs model output (left) and manner by which the model picks off flow data at relevant locations (i.e., the locations of the kite and tether).

2.5 Floating Platform and Wave Characterization

The team has developed an initial conceptual floating platform design, along with a corresponding model that (i) integrates with the kite dynamic model and (ii) is adaptable to a multitude of different platform designs. The floating platform model has been validated under (i) constant flow conditions without waves (where only the tether forces cause motion of the platform), (ii) variable flow conditions, and (iii) the combination of variable flow conditions alongside waves with specified significant height and period.

In the code, the floating platform is implemented as a lumped mass model, illustrated conceptually in Figure 5. This lumped mass model design is inspired by work done modeling the ocean forces on WECs to

characterize anchor tether loading [6]. The anchor tethers attached to the floating platform are three in number and are modeled as lumped mass spring damper systems in the same way as the tether attaching the kite to the floating platform.

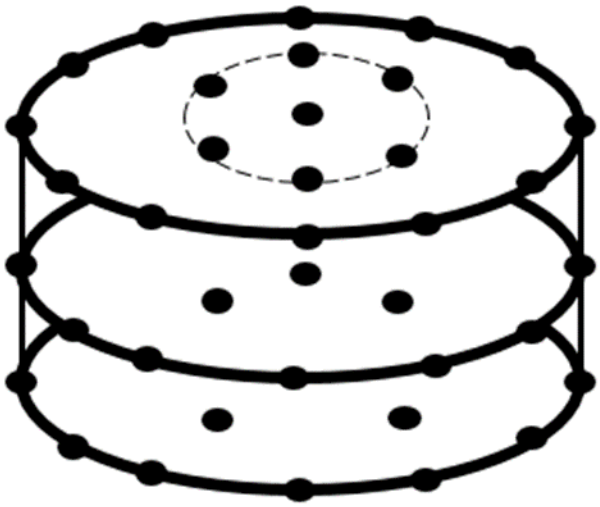

Figure 5: Lumped mass floating platform representation. Masses, hydrodynamic forces, and buoyant forces are concentrated at the centers of the nodes, which possess nonzero volume in order to avoid jump discontinuities in buoyancy that occur when nodes exit/re-enter the water.

Using a lumped mass model allows for the hydrodynamic and net buoyancy forces to be calculated at each lumped mass position. In the case of the hydrodynamic force calculations, because the flow profile differs spatiotemporally, this simplifies the calculations greatly by discretizing the force calculation on the surfaces of the floating platform. For the net buoyancy force calculation, the lumped mass model allows for the center of buoyancy, which would change as a function of the platform's orientation, to not need to be computed, because the net buoyancy is computed per lumped mass. In our model, each lumped mass has a radius, which allows for its force contribution to change linearly with its distance from the surface and cropped when the sphere formed by each lumped mass's radius is either completely in or out of the water. This is illustrated in Figure 6.

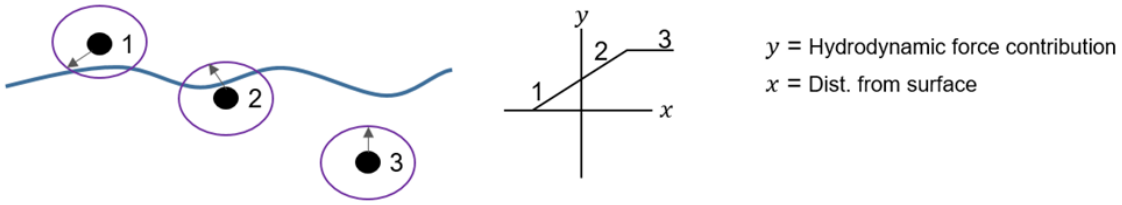

Figure 6: Illustration of the use of a lumped mass approach, where each node has nonzero volume for the purposes of retaining continuity in the dynamic model.

An initial analysis was run in the absence of waves. In this restricted scenario, simulations characterize the dynamic coupling between platform motion and kite motion, which can be extremely important, but do not yet characterize the (likely smaller) impact of waves. The results shown in Table 2 (below) demonstrate, intuitively, that increasing the anchor tension (obtained by reducing the unstretched anchor line lengths) results in net power production that approaches that of a stationary platform.

Maximum anchor tension after initial transients (kN)	Average net power production (kW) – Assumed 1 m/s flow speed
237	3.47
248	6.62
253	8.67
273	8.85
Stationary platform	9.67

Table 2: Net power under the integrated floating platform/kite model for a variety of anchor line tensions (obtained by varying the unstretched length of the anchor tether).

To incorporate waves into the model, the team has created a wave model using the combination of linear two-dimensional waves as shown in "*Marine Hydrokinetics*" by Paul Newman. This allows wave velocities as a function of spatial position and time to be computed easily for each lumped mass position of the floating platform. Additionally, this model fits cleanly into the team's environmental module within the overall Simulink model, which prescribes velocities at each spatial location in the kite's domain, at each time step. The superposition of many linear two dimensional waves allows for complex wave velocities. This is represented in one dimension in Figure 7.

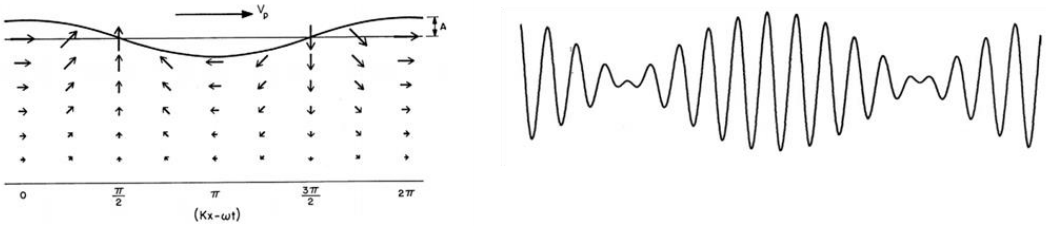

Figure 7: One-dimensional representation of a linear wave (left) and multiple linear waves (right).

The team performed an extensive analysis of the kite's performance flying off a floating platform, in the presence of superimposed waves and current (considering both constant current and variable current emulated by the flow model presented in Section 2.4), which have been detailed in [7] and [8]. Note that a fully coupled approach, rather than a superposition approach, remains a topic of future work (outside of the original scope of this project). Figure 8 shows a selection of these results, demonstrating consistent power output as wave period and amplitude vary over typical ranges, along with a clear increase in peak-to-average power ratio as wave energy increases.

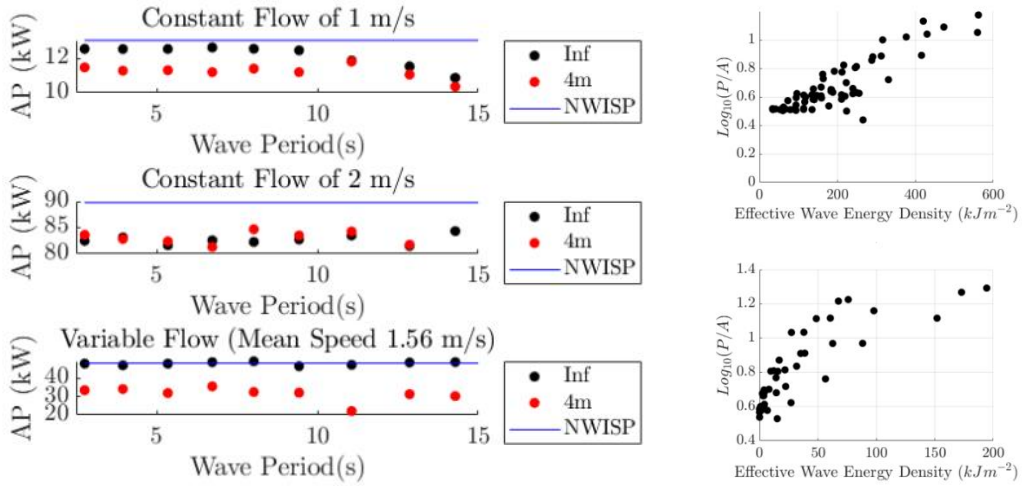

Figure 8: Left: Simulation results in the presence of waves and current, with differently sized floating platforms (Inf = fixed/infinite-sized platform, 4m = 4m diameter, and NWISP = no waves, fixed (infinitely sized) platform). Right: Trends in peak/average power with no turbulence (top) and with turbulence (bottom), as a function of wave energy density.

2.6 Power Take-Off Characterization

While the closed-loop time constants of the PTO system will in fact be extremely fast relative to the time constants associated with the kite's flight, thereby allowing the team to utilize a static efficiency map for characterizing the PTO system in several circumstances, it was nevertheless identified as important to create a more detailed model of the PTO system for the following purposes:

- It was necessary to design a PTO system and corresponding controller for Subtask 2.3 (and for successful fulfilment of electrical power production in tow testing), which will be facilitated by an accurate dynamic model that can integrate with the existing dynamic model for the kite.
- While the kite's flight dynamics are on the order of ~10 seconds, reflecting a large time scale separation relative to PTO dynamics on the order of ~0.1 seconds, the tether exhibits faster, higher-frequency modes that may interact with the PTO dynamics.

Herein, we provide a brief description of our initial PTO ***design efforts*** and corresponding ***modeling efforts*** (Subtask 1.3), which culminated in fulfillment of milestone 1.3.

The ***design process*** of the PTO system has three main parts:

1) The overall topology of the system.
2) The choice of electric machines.
3) The type of electricity transmission.

PTO topology: The team has selected a non-reversing topology where two electric machines are used to separately generate electricity and provide the torque necessary for the reel-in of the kite. This topology allows for the two machines to be sized for their appropriate torque/speed range. The two machines are connected to a tether drum via clutches as illustrated in Figure 9. This topology will be implemented in both the large and small scales systems.

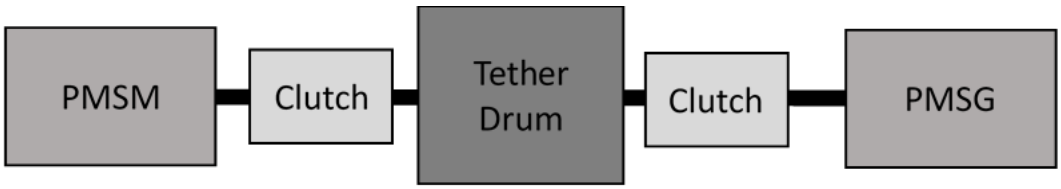

Figure 9: Basic proposed PTO topology.

Electric machine choices: There multiple potential types of electric machines for energy generation. Induction type machines are very common in large power plants and in fixed speed operating wind turbines. They are cheap but are cannot easily operate with varying speed. The team has selected permanent magnet synchronous machines (PMSM) instead. These can operate with varying speed, are more reliable, and more efficient due to the use of a permanent magnet for self-excitation. In fact, permanent magnet synchronous generators (PMSG) advantages over induction machines are causing the wind energy industry to transition to these types of generators.

Electricity transmission: For the 1kW two test demo, initial maritime market systems, and full-scale grid-connected systems, the team has chosen to use simple diode-based rectifiers to convert the AC power from the PMSG to DC, where the DC power is either (i) used to power a simple load (tow test demo), (ii) used to charge a battery (maritime applications such as AUVs), (iii) used to directly power a floating platform, or (iv) sent to shore and converted (via inverter) back to AC to be supplied to the grid (utility-scale). High voltage DC (HVDC) will be used in case (iv).

PTO modeling: For the purpose of simulation and control, the dynamic model of the PTO system is dominated by the tether drum dynamics, with much faster motor dynamics that can be treated as instantaneous.

The tether drum dynamics are given by:

$$J_d \ddot{\theta}_d = T_{tether} - T_{motor/generator}$$

where J_D is the drum inertia, $\ddot{\theta_d}$is the drum angular acceleration, T_{tether} is the torque exerted by the tether on the drum, and $T_{motor/generator}$ is the torque exerted by either the generator or the motor.

The motor dynamics are given by:

$$\frac{di_d}{dt} = \frac{v_d - Ri_d + \omega_s L_q i_q}{L_d}$$
$$\frac{di_q}{dt} = \frac{v_q - Ri_q - \omega_s\left(L_d i_d + \lambda_f\right)}{Lq}$$

where i_d and i_q area the d −(direct) and q-(quadrature) axis components of stator current, v_d and v_q are stator voltages in the d- and q- axis, R is the stator resistance, L_d and L_q are stator inductances in the d- and q- axis, λ_f is the flux linkage due to the permanent magnets and ω_s is the inverter frequency.

The electromagnetic torque is given by:

$$T_e = \frac{3}{2} p(\lambda_f i_q + (L_d - L_q) i_d i_q)$$

Here, p is the number of pole pairs per phase in the stator.

There are two main losses in an electric machine: the resistive losses in the stator, and the friction losses. The efficiency of the electric machines is given by:

$$\eta = \frac{P_{out}}{P_{in}}$$

where:

$$P_{out} = T_l \omega_r$$
$$P_{in} = \frac{3}{2} i_q^2 R + T_e \omega_r$$

The direct current i_d is typically forced to zero, thus the electromagnetic torque can be written as:

$$T_e = \frac{3}{2} p \lambda_f i_q$$

The power consumed by the motor is thus:

$$P_{in} = \frac{3}{2} \left(\frac{T_e}{\frac{3}{2} \lambda_f p} \right)^2 R + T_e \omega_r$$

The electromagnetic torque has to overcome the load torque and the friction torque:

$$T_e = T_l + T_f$$

where the friction torque can be approximated as:

$$T_f = b\ \omega_r$$

The efficiency can be finally written in terms of the load torque and the rotor speed as follows:

$$\eta = \frac{T_l \omega_r}{\frac{3}{2} \left(\frac{T_l + b\ \omega_r}{\frac{3}{2} \lambda_f p} \right)^2 R + (T_l + b\ \omega_r) \omega_r}$$

When the system is operating in generation mode, the power generated is thus: $P_{gen} = \eta T_l \omega_r$. During reel-in, the power consumed is thus: $P_{gen} = \frac{1}{\eta} T_l \omega_r$.

PTO integration with the kite model: The PTO model uses as inputs the tether tension and a tether release speed command. It then outputs the actual tether speed and the power generated by the system. A Simulink diagram of the system is shown in Figure 10.

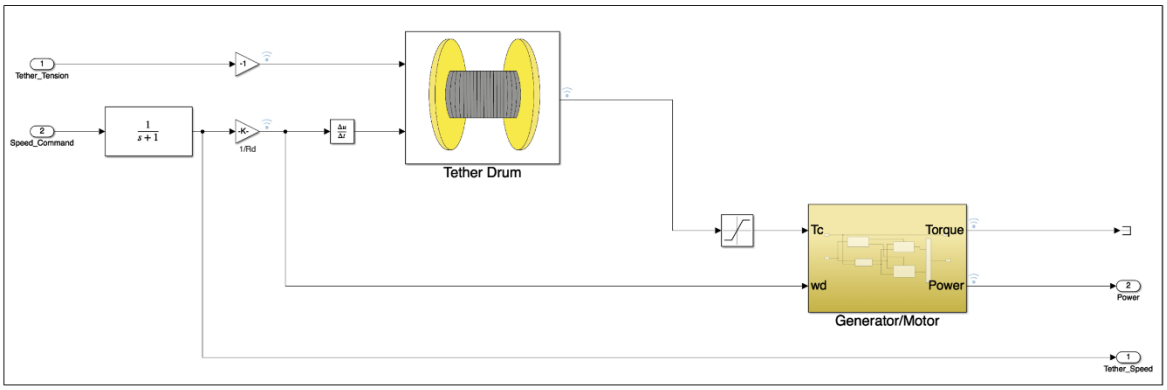

Figure 10: Simulink diagram of the PTO model.

Milestone 1.3 required the team to (i) develop a PTO model, (ii) integrate it into the dynamic model, and (iii) show that the dynamic model behaves robustly with the PTO and flight dynamic models integrated together.

The PTO model has been integrated with the master kite dynamic model, and simulations have been run over a full representative set of constant and spatiotemporally varying flow environments. Table 3 provides resulting average electrical power, mechanical power, and calculated efficiency over a representative set of constant-speed and variable-speed simulations. The results indicate that ***(i) the model executes robustly with the PTO model integrated, as required by the milestone, and (ii) conversion efficiencies of the present design are approximately 85 percent over the full operational envelope of the kite***.

Flow speed (m/s)	**Path shape**	**Electrical power (kW)**	**Mechanical power (kW)**	**Efficiency**
1	Figure-8	8.03	9.33	0.84
1.5	Figure-8	22.9	26.9	0.85
2	Figure-8	55.2	64.8	0.85
1	Ellipse	8.16	9.41	0.87
1.5	Ellipse	25.4	29.3	0.87
2	Ellipse	55.2	60.5	0.86
Variable (MSR model + turbulence, floating platform deployment) – Ave. flow speed = 1.58 m/s	Figure-8	24.1	28.5	0.84
Variable (ADCP data + turbulence, seabed deployment) –	Figure-8	12.9	15.2	0.84

Ave. flow speed = 1.26 m/s				

Table 3: Electrical power, mechanical power, and calculated efficiency over a representative set of constant- and variable-flow simulations with the PTO model and kite dynamic model integrated.

Figure 11 shows mechanical and electrical power vs. time under a constant flow speed of 2 m/s and a variable flow environment averaging 1.58 m/s. Results demonstrate robust, sensible operation of the dynamic model with the PTO model integrated.

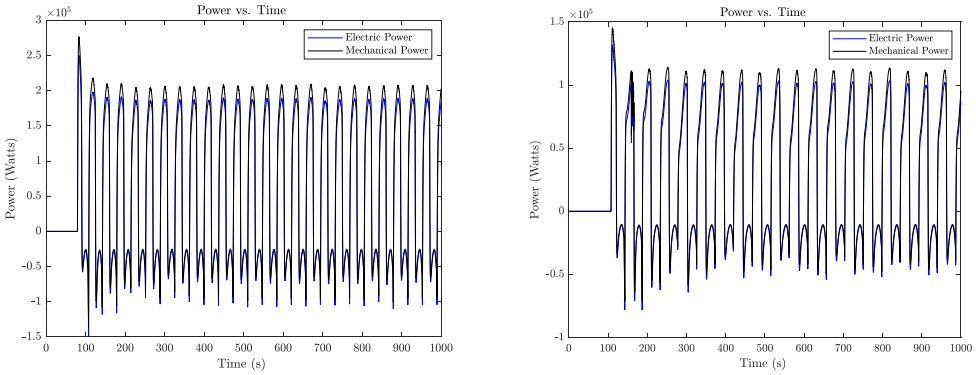

Figure 11: Mechanical and electrical power vs. time for a constant flow speed of 2 m/s (left) and variable flow environment averaging 1.58 m/s (right.

2.7 Techno-Economic Modeling

The team was tasked with creating and refining an economic model for estimating the levelized cost of energy, annual energy production, power/weight ratio, and peak to average power. An economic reference model has been created to estimate the total costs of the system over a 20-year period. This model was created using quotations from companies providing services required, costs of similar products to what the system will use, and data from Sandia National Lab's Reference Model Project.

This model accounts for:

Capital expenses ("Capex"):

- Development (permitting, siting and scoping)
- Infrastructure (subsea cables, connectors)
- Mooring (anchors, mooring line, hardware)
- Structural components and PTO system (electronics, kite and ground station structure)
- Subsystem integration (grid connection)
- Installation, decommissioning, and contingencies

Operational expenses ("Opex"):

- Insurance
- Environmental monitoring and regulatory compliance
- Marine repair operations
- Shore side repair operations
- Replacement parts
- Consumables

To capture the techno-economics of the kite system in a compact worksheet that took into account the aforementioned features, the team relied on and adapted the ARPA-E SHARKS Metrics Spreadsheet, which was originally designed for the estimation of techno-economic performance (in terms of levelized cost of energy, capacity factor, and annual energy production, in addition to "surrogate metrics" related to an adjusted power-per-unit-mass and efficiency metric). While the candidate sites were pre-specified for the ARPA-E SHARKS spreadsheet, candidate kite deployment sites were identified internally as part of the present project, and flow resource data was obtained via either NOAA (for candidate tidal sites), acoustic Doppler current profiler (ADCP) data (for candidate ocean current energy sites where ADCP data was in fact available), or the Mid-Atlantic Bight, South-Atlantic Bight (MAB-SAB) Regional Ocean Model (for instances when ADCP data was not in fact available). Mass data was obtained through CAD renderings generated by the team, incorporating structural elements deemed to be sufficient based on the team's structural modeling tool, and a "power surface" (power vs. tether length vs. flow speed) was obtained via the team's dynamic model. Note that Chapter 5 provides significantly more detail regarding the optimization of the kite geometry, structure, controller, and site selection based on techno-economic considerations.

3 High-Level Device Sizing

The flight performance and the structural performance are optimized by minimizing the structural mass of the (i) wing and (ii) fuselage, while simultaneously to (iii) optimizing the flight performance. These three optimizations are performed through three tools, namely:

1. *Steady flight optimization tool* (SFOT), which selects wing and stabilizer geometric properties to minimize the kite's displaced volume (a surrogate for mass), subject to geometric and power constraints.
2. *Structural wing design tool* (SWDT), which selects spar and skin properties to minimize wing mass, subject to wingtip deflection and buoyancy considerations.
3. *Structural fuselage design tool* (SFDT), which selects the fuselage thickness to minimize fuselage mass, subject to hoop stress, sheer stress, and buckling constraints.

The process diagram of the co-design tool is shown in Figure 12 and detailed in [9] and [10].

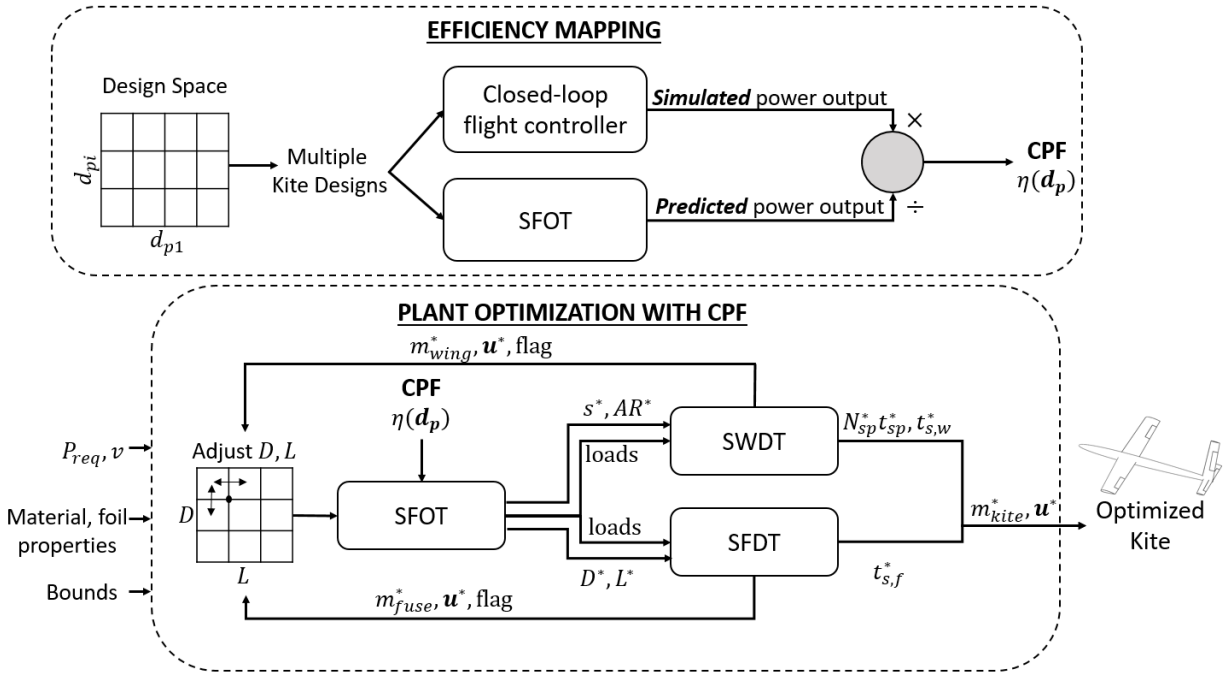

Figure 12: A schematic showing the working of the co-design tool. The efficiency mapping is done prior to the optimization, which uses the efficiency as a CPF to estimate $\boldsymbol{P_{act}}$ in SFOT.

3.1 Geometric Sizing Tool

The geometric sizing tool, termed the "steady flight optimization tool" (SFOT), performs a steady-state flight performance optimization by adjusting the geometric properties of the wing and fuselage. The tool seeks to obtain the most compact wing design that can produce the required power for a rated flow speed. This is done is by minimizing a surrogate for mass while meeting the performance and geometric constraints:

$$\min_{s,AR,D,L} \quad f_{\text{surr}}(\boldsymbol{u})$$

$$\text{subject to:} \quad \max_{\boldsymbol{u}} \frac{2}{27} \cdot \frac{\eta \rho v^3}{AR^2} \left(\max_{\alpha} \frac{C_L^3}{C_D^2} \right) \geq P_{req}$$

$$u_{min} \leq \boldsymbol{u} \leq u_{max}$$

where are $\boldsymbol{u} \in [s, AR, D, L]$ is the set of decision variables, $f_{\text{surr}}(\cdot)$ is the objective function that acts as a surrogate to minimizing wing mass (can be wing volume or wing span), ρ is the density of water, P_{req} is the $\eta(s, AR)$ is the flight efficiency that accounts for the difference between the dynamic and steady-flight estimates of power, v is the rated flow speed, C_L and C_D are the lift and drag coefficients of the whole kite, and α is the angle of attack. The generated mechanical power estimate shown in the inequality constraint is based on the seminal work of Miles Loyd, referenced throughout the AWE and MHK kite literature. SFOT optimizes the kite geometry to maximize hydrodynamic performance.

3.2 Structural Sizing Tool

The structural sizing tool consists of: (i) the structural wing design tool (SWDT), and (ii) the structural fuselage design tool (SFDT). Each tool aims to minimize the respective structural masses of the kite's section being designed through the respective support structures.

Structural wing sizing:

The wing structural design tool minimizes the structural support mass required to support the wing. The structure is designed as a combination of spars and a shell. The SWDT solves the mixed-integer constrained optimization problem, formulated as:

$$\min_{t_{sp}, t_{sw}, N_{sp}} \quad m_{wing}(\boldsymbol{u})$$

$$\text{subject to:} \quad I_{wing} \geq I_{req} \mid \delta_{max}$$

$$u_{min} \leq \boldsymbol{u} \leq u_{max}$$

where $\boldsymbol{u} \in [t_{sp}, N_{sp}, t_{sw}]$ is the set of decision variables (which respectively are spar thickness, number of spars, and wing thickness), I is the bending moment of inertia and m_{wing} is the mass of the wing. The wing cross-section consists of rectangular spars (0-3 in number) and an airfoil-shaped outer shell. The first constraint ensures the designed wing has the required bending inertia subject to a maximum wing tip deflection of ($\delta_{max} = 5\%$) of wing's half-span due to hydrodynamic loading.

Structural Fuselage Sizing:

The structural fuselage design tool (SFDT) minimizes the mass of the fuselage while meeting several structural constraints. A simplifying assumption is made to design the fuselage as a cylindrical shell. The SFDT solves the optimization problem formulated as:

$$\min_{t_{sp}, t_{sw}, N_{sp}} \quad m_{fuse}(\boldsymbol{u})$$

$$\text{subject to:} \quad \frac{\sum F_z}{t_{sf} L} \leq \zeta \sigma_y$$

$$\frac{PD}{2t_{sf}} \leq \zeta \sigma_{0.5}$$

$$\frac{|M_{max}|}{S(\boldsymbol{u})} \leq \zeta \sigma_y$$

$$u_{min} \leq \boldsymbol{u} \leq u_{max}$$

where $\boldsymbol{u} \in [D, L, t_{sf}]$ is the set of decision variables (which respectively are fuselage diameter, length, and shell thickness). The three constraint equations respectively represent the following stress inequalities:

1. Shear stress: The first constraint models the shear behavior due tangential loads at the wing and stabilizer attachment points. F_z are the loads in the direction normal to the wing, ζ is the factor of safety, and the σ_y is the yield stress of the material.

2. Hoop stress: The fuselage of the kite is assumed to be a thin-walled pressure vessel. The difference in the external and internal pressures, P, causes circumferential stresses. The variable $\sigma_{0.5}$ is the stress at 0.5% elongation.
3. Buckling: The lift forces of the wings and the horizontal stabilizer induce buckling loads about the tether attachment point. $|M_{max}|$ is the maximum buckling moment calculated for a set of hydrodynamic forces, and $S(\boldsymbol{u})$ is the section modulus of the fuselage.

4 Control Design

4.1 Basic Path-Following Control (and Simplified Variants)

The lower level controller is a hierarchical controller that enables the kite to fly cross-current to the path in figure-eight motions. A full, detailed, mathematical summary of the lower-level path-following controller is available in [11].

This path-following controller manipulates the control surfaces (ailerons, elevator, and rudder) to make the kite follow a prescribed figure-eight path. The structure of this controller was modeled after hierarchical controllers commonly used in the airborne wind energy community [12]. This controller, shown in Figure 13, is composed of four parts:

1. A desired velocity angle calculation, which computes a target orientation of the kite's velocity vector based on a prescribed flight path and the kite's measured position.
2. A desired tangent roll angle calculator, which calculates a target value of the kite's roll angle relative to the tangent plane to the instantaneous sphere that the kite is flying on. By rolling the kite, the lift vector is oriented in order to adjust the kite's velocity angle.
3. A desired control moment calculator, which inputs the tangent roll command, the kite's azimuth angle, elevation angle, Euler angles, velocity, and the flow velocity at the kite's center of mass to output a desired roll and yaw moment.
4. A control allocation module, which computes control surface deflections based on target moments.

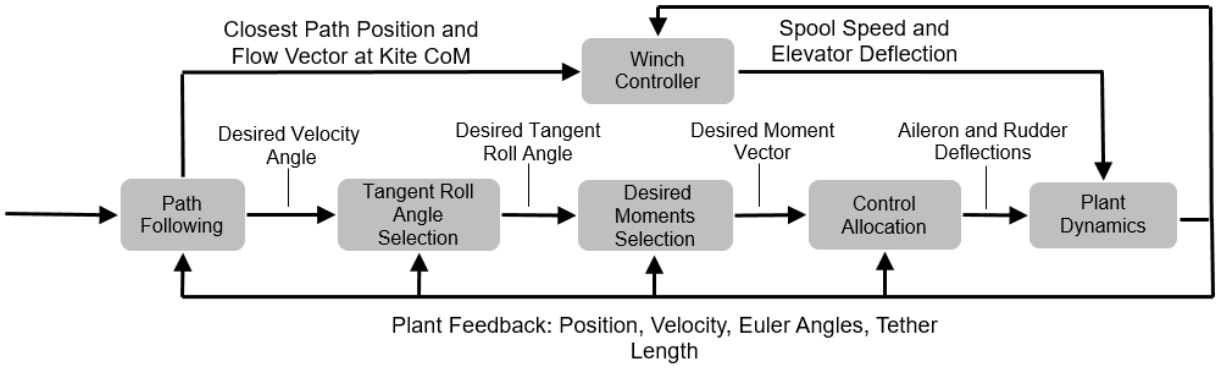

Figure 13: Hierarchical path-following controller structure

This hierarchical controller structure is ultimately responsible for commanding the control surface deflections, whereas a state machine, described in the following section, regulates the switching between different spooling modes, where the spooling control is handled within each mode.

4.2 Spooling State Machine

As mentioned in the previous section, to reduce the amount of tether tension during spool-in, the spooling method was reformulated from an intra-cycle approach to a multi-cycle spooling approach. In this new approach, the kite is spooled out in continuous figure-eights until a maximum tether length threshold is met, and then spooled in radially towards the base station. To accomplish this, a transition controller was created, which governs the transition between spooling out in crosscurrent flight and spooling in non-crosscurrent flight. This transition controller consists of four modes of operation:

1. *Non-crosscurrent spool-in*, where the kite is commanded to be maneuvered such that it has a roll Euler angle of zero, and is spooled in radially towards the base-station at a low angle of attack,
2. *Crosscurrent flight initialization,* where the controlled equilibrium from the previous mode is released, creating velocity without the need for control surface deflections,
3. *Crosscurrent flight,* where the kite gains velocity while approaching the path, and once the path is reached, generates power by spooling out while flying perpendicular to the flow in figure-eight motions, and
4. *Exiting Crosscurrent flight*, where the kite exits the figure-eight path and achieves a low angle of attack to prepare for the non-crosscurrent spool-in phase.

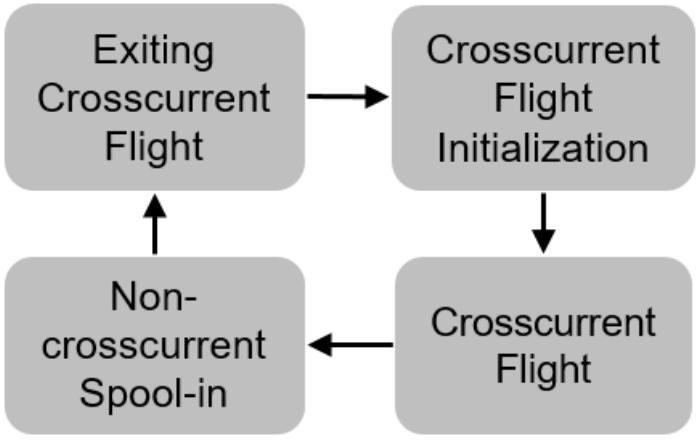

Figure 14: Transition controller state machine

Operation Mode	Transition condition
1 - 2	Magnitude of the kite's velocity is less than the magnitude of the flow velocity multiplied by a user selected gain
2 - 3	The magnitude of the kite's velocity is greater than the flow velocity
3 – 4	The maximum tether length threshold is reached, and the kite is on one of the edges of the path
4 – 1	The velocity of the kite is less than the velocity of the flow

Table 4: The table above describes the transition conditions between the four operation modes, where 1 is non-crosscurrent spool-in, 2 is crosscurrent flight initialization, 3 is crosscurrent flight, and 4 is exiting crosscurrent flight.

This transition controller state machine is shown in Figure 14, and the conditions for entering and exiting each mode is shown in Table 4.

Elevation Angle and Spool Speed Optimization

The goal in this optimization is to pick the spooling speeds and path center elevation angles that maximize the average power production for multi-cycle spooling. The flow changes most dramatically as a function of depth. With this knowledge, as the kite spools in and out over a large depth range, it can catalog the flow speeds as a function of depth to create a lookup table of flow speed by depth. What also makes this possible is the fact that the time constants associated with multi-cycle cycle are much smaller than the time constants of the ocean currents. Using this knowledge, the optimization algorithm picks path center elevation angles and spool speeds such that the power is maximized. It is worth noting that this optimization of the elevation angle profile is only needed in a variable flow environment.

To perform this optimization, we used a sequential quadratic programming approach. In this optimization, the states were the elevation angle and time, the stages were discretized lengths of tether, and the control inputs were the change in elevation angle between stages and the mean spool speed. Figure 15 graphically depicts this optimization problem.

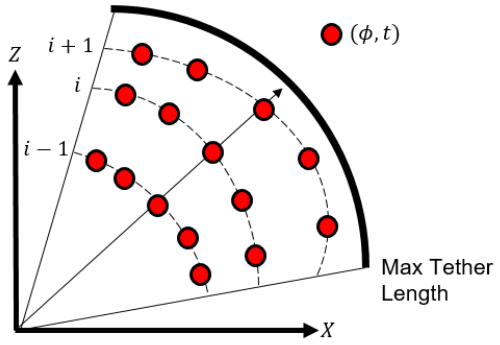

Figure 15: Optimization for picking spool speeds and path center elevation angles. In the above figure, the variable i, denotes the stages, **ϕ**, denotes the elevation angle, and t denotes time.

The objective function that we seek to maximize can be written as

$$J_{cost} = \frac{1}{T}\sum_{i=0}^{N-1}\left(\left(v_f - \mathrm{v}_{\mathrm{spoolMean},i}\cos(\phi_i)\right)^2 \cos^2\phi_i\right),$$

where v_f is the flow speed, ϕ_i is the elevation angle at each stage, i refers to the stage number, and T refers to the total time. Ultimately, this objective function acts as a surrogate for the power over one multi-cycle cycle.

For a 3000-second simulation, in a spatiotemporally varying flow profile, Figure 16 shows simulation results for a baseline control strategy (which maintains a constant spool-out speed and elevation angle) and an optimized strategy according to the optimization procedure described above. These results indicate an approximately 20 percent performance improvement from the optimization of the elevation angle and spooling speed profile between successive spooling iterations.

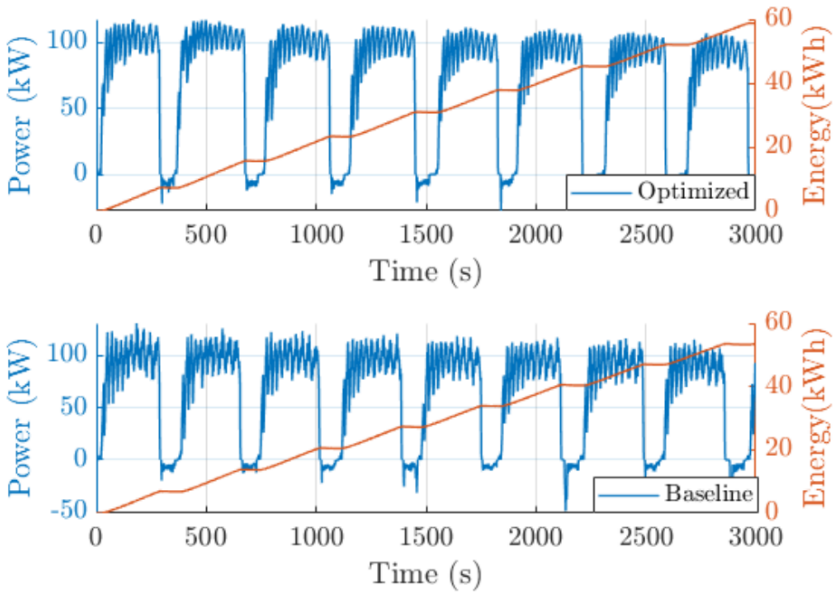

Figure 16: Performance comparison between baseline (constant spool-out speed and elevation angle) and optimized spooling profiles in a variable flow environment.

4.3 Economic Iterative Learning for Online Path Optimization

Iterative learning control (ILC) learns from previous repetitions of a task to inform future control decisions. To illustrate what iterative learning control is, picture a basketball player shooting free-throws. The cycles/iterations (where one cycle/iteration is one repetition of a task), are the basketball shots. The control input that the player uses, is their muscle movements. What the player learns from is how far off the shot is.

Our kite system performs repetitive operations (spooling cyclically as well as flying in figure-eight cycles). Using this cyclic behavior, we attempted to learn the optimal set of path parameters based on the kite's past performance. The path can be defined using two parameters (a width and a height) if the path is defined by the Lemniscate of Booth, or if a path is being performed by tracking roll and yaw Euler angle sinewave setpoints, the control parameters are the period of the sinewaves, the phase of the sinewaves, the offset, and the amplitude of the sinewaves.

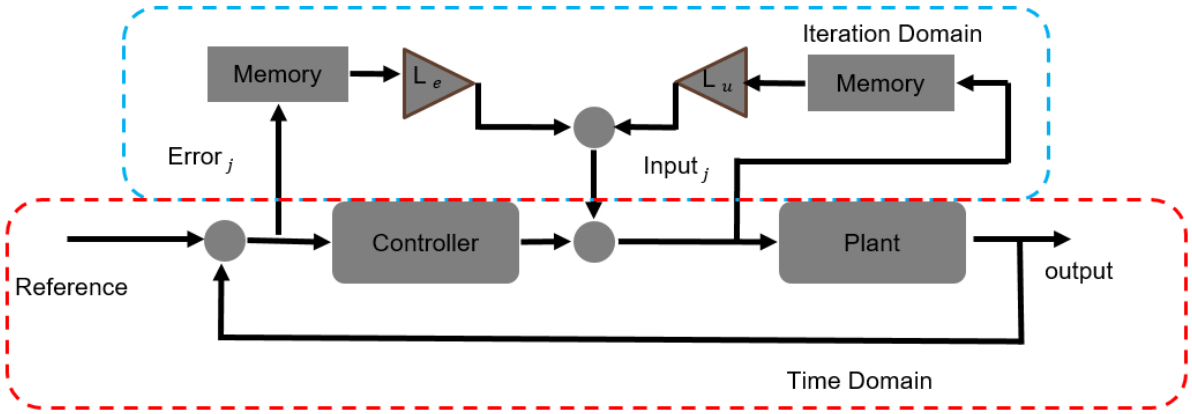

Figure 17: Traditional iterative learning control for tracking applications.

Traditional iterative learning control, shown in Figure 17, is used to optimize the tracking performance of a system. Unfortunately, for our system, what we care about is not the tracking performance, but the cycle-averaged power production of the kite system. Because of this, we re-tailored the traditional iterative learning control formulation to optimize economic objectives (which for our case is cycle-averaged power production). A block diagram of this formulation is shown in Figure 18.

While a brief review of the economic ILC strategy is given here, further details can be found in publications resulting from this project, including [13], [14], and [15].

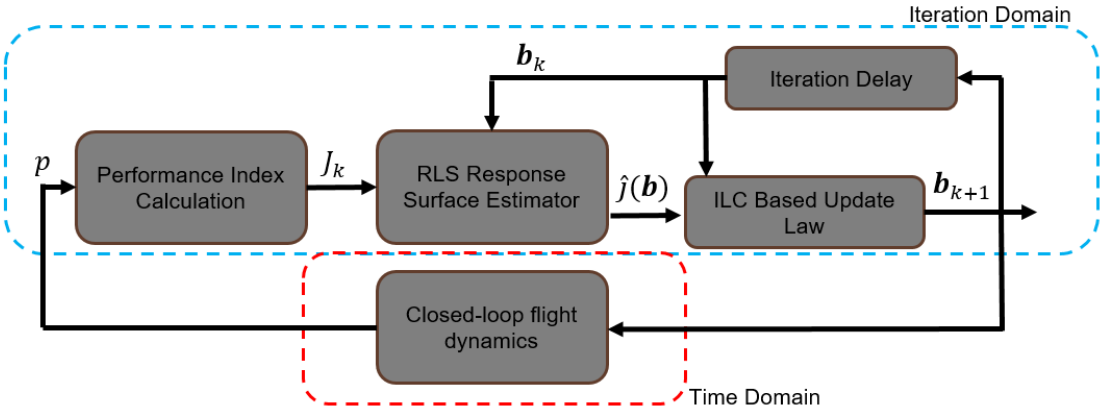

Figure 18: Economic iterative learning control

This ILC formulation operates in real time, taking in the performance of the system over a cycle as a function of the control parameters present at that cycle. From Figure 18, p represent a vector of plant signals determining the performance level, given by J_k, from the k^{th} iteration, under the control parameters $\boldsymbol{b}_k$. Based on this mapping, a hyper-surface is formed mapping control parameters to performance, and the gradient of the surface, $\nabla\tilde{J}(\boldsymbol{b}_k)$, is estimated by a recursive least squares (RLS) estimator. The ILC update law then uses this gradient along with persistent excitation $\mathbf{p_k}$ to calculate a set of control parameters for the next trial. This update law is given by:

$$\boldsymbol{b}_{k+1} = \boldsymbol{b}_k + K_e\nabla\tilde{J}(\boldsymbol{b}_k) + \mathbf{p_k}$$

where K_e is a learning gain. Using this economic iterative learning control, we are able to greatly improve the cycle-averaged power performance of the kite. Results using this control strategy can be seen in Section 9.3.

4.4 Economic Iterative Learning for Online Elevator Profile Optimization

Economic ILC can also be used to optimize the elevator profile for the kite. One option is to use the meta-model-based ILC strategy and add a constant elevator deflection parameter to the set of control parameters being optimized online.

The second option is to implement a flexible-time economic ILC strategy, where the entries in the elevator deflection sequence for the next figure-eight cycle are indexed as a function of the position of the kite about the path but implemented as a function of time. A flexible time-economic ILC strategy is necessary when using the system dynamic model to inform an ILC optimization because the time for each figure-eight lap is not constant.

The economic ILC for the elevator profile is performed by linearizing the time domain model at N at discrete points and then implementing the control using the path parameter s versus time-step map from the previous cycle. This is shown graphically in Figure 19.

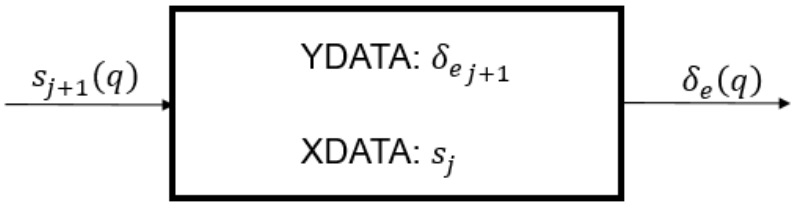

Figure 19: Flexible-time implementation. In the figure, $\boldsymbol{s_{j+1}(q)}$ is the path position for $\boldsymbol{q^{th}}$ time step, $\boldsymbol{\delta_{e_{j+1}}}$ is the elevator deflection profile calculated as a function of the path for the next figure-eight cycle $\boldsymbol{j+1}$, and $\boldsymbol{\delta_e(q)}$ is the elevator deflection computed to be used at the $\boldsymbol{q^{th}}$ time step.

To select the elevator deflection profile calculated as a function of the path for the next figure-eight cycle the objective function

$$J_{j+1} = \left(U_{j+1} - U_j\right)^T R\left(U_{j+1} - U_j\right) - Y_{j+1}^T Q Y_{j+1}$$

is minimized where $U_j = \delta_{e\,j}$ and Y_{j+1} is the kite's cycle averaged speed at the next trial. This objective function effectively maximizes the kite's speed, and in turn the mechanical power, while also penalizing large potentially destabilizing control changes. To minimize this objective function, the resulting control law is used:

$$U_{j+1} = -(G^T Q G - R)^{-1}\left(R U_j + G^T Q D\right)$$

where the matrices G, D are the system matrices resulting from linearizing the system from the elevator deflection to the kite's velocity, and then lifting the system. The matrices R, Q are weighting matrices. This control law is derived by setting the gradient of the objective function equal to zero and then solving for U_{j+1}. Additionally, to track a rated speed, which can be necessary if the flow speed is high enough that the system producing power above the rated power which constitutes no economic gain but increases the fatigue to the system, the objective function

$$J_{j+1} = (U_{j+1} - U_j)^T R(U_{j+1} - U_j) + (-Y_{j+1} + \mathbf{1}S_{\text{rated}})^T W(-Y_{j+1} + \mathbf{1}S_{\text{rated}})$$

is used, where S_{rated} is the rated speed. Deriving the control law in the same was as before results in

$$U_{j+1} = (G^T WG + R)^{-1}(G^T WG + R)U_j + (G^T WG + R)^{-1}(G^T W)E_j$$

where $E_j = -Y_{j+1} + \mathbf{1}S_{\text{rated}}$.

An initial assessment of this control strategy was done on a *wind* energy application, owing to the fact that the variations in wind speed happen more rapidly than those of underwater current, thereby demanding faster adaptation. However, the same principles hold with an underwater system. The effectiveness of this control law is demonstrated for two cases below for an airborne wind energy system with a 7m span in Figures 20 and 21.

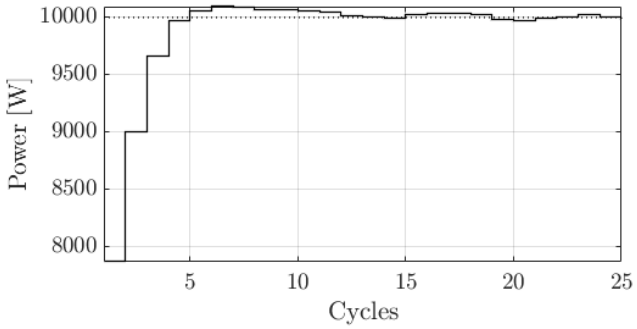

Figure 20: Cycle-averaged mechanical power as a function of cycles for the kite experiencing a 10 m/s wind speed. The dotted line is the system rated mechanical power.

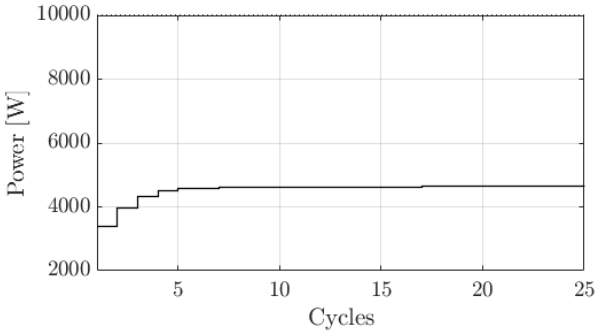

Figure 21: Cycle-averaged mechanical power as a function of cycles for the kite experiencing a 7 m/s wind speed. The dotted line is the system rated mechanical power.

4.5 Continuous-Time Optimal Control for Spooling Optimization

The team has developed optimal, non-adaptive periodic spooling strategies (pertaining to Subtasks 3.1 and 3.2). In particular, the team has examined the use of Pontryagin's Maximum Principle (PMP) to generate an optimal spooling speed profile based on a simplified model of tension as a function of spooling speed over the course of a figure-8 or elliptical path. PMP is applied such that we can choose spooling speeds by maximizing a function created by combining the equation for maximizing power with the equation representing the winch model. We use this to select spooling speeds at every location along the path, updating the optimization between path iterations until the kite begins and ends each lap at the

desired tether length. This is done by selecting the spooling speeds from a surface generated mapping tension to spool speed for each path discretization, an example of which is shown in Figure 22. Details of the continuous-time optimal control approach can be found in [16].

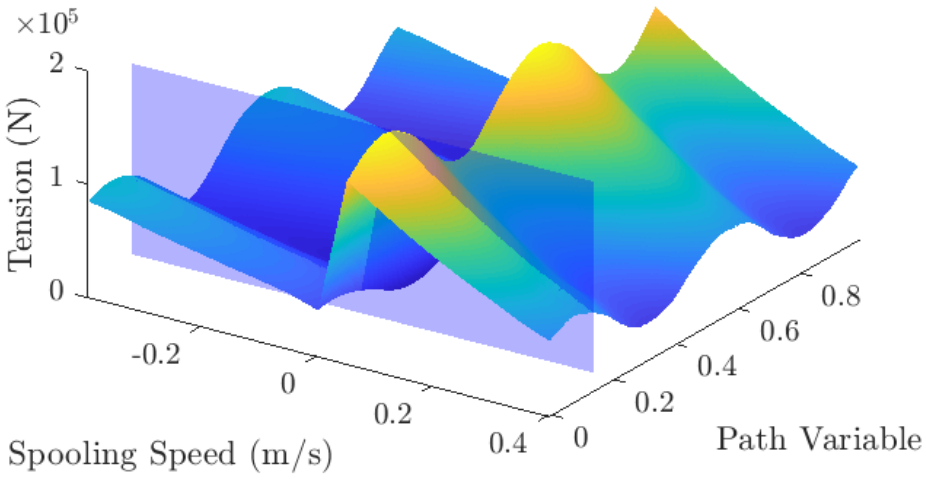

Figure 22: Spooling speed vs tension at each path discretization.

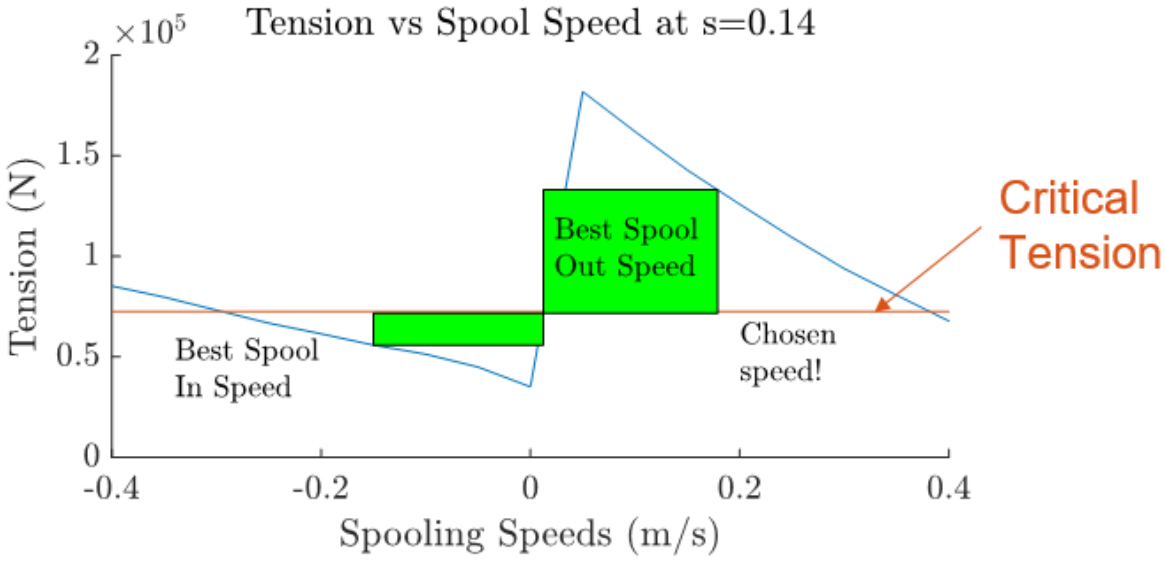

Figure 23: Slice of Figure 22 shown to illustrate how spool speeds are selected.

The slice from Figure 22 can be seen in Figure 23, which shows how the optimal spool in and spool out speeds are selected. From Figure 23, the critical tension is parameter that dictates at what tension to switch between spooling in and spooling out. It is selected such that the kite has a net zero amount of tether spooled.

The results obtained through the application of PMP were compared against the baseline spooling strategies used in fulfillment of Milestones 1.2.1 and 1.2.2. The optimized spooling speeds generated between 14% and 45% improvement relative to these baselines. Figure 24 shows cumulative energy generation under the baseline vs. PMP-based spooling strategy (left), along with the spooling speed profile resulting from PMP-based spooling (right).

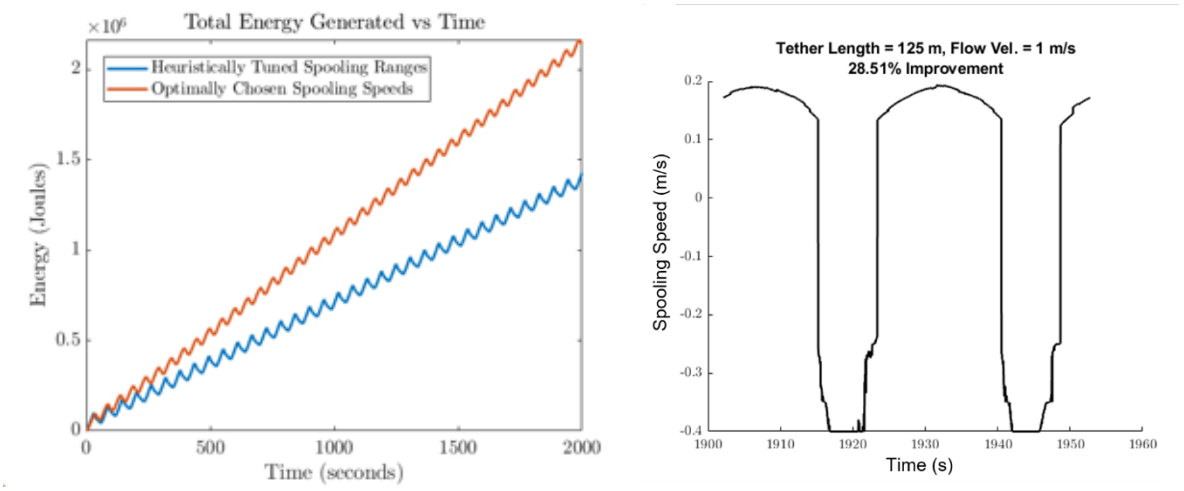

Figure 24: Cumulative energy generation (left) under PMP-based and baseline spooling strategies, along with the PMP-based spooling profile (right).

4.6 Evaluation of a Low-Order Optimization of the Combined Spooling Profile and Flight Pattern

While the prior control results tackle the problems of path optimization, angle of attack optimization, and spooling speed optimization using detailed models, they do so independently, thereby suffering some losses due to the non-consideration of coupling. The following results represent an initial effort toward treating that coupled problem. However, the results are also based on a highly simplified model at present, making several assumptions. This work is intended as a springboard for potential future work on coupled optimization. The kite was modeled under the following assumptions:

1. The kite's tether is a massless, drag-free, straight line kinematic connector between the kite and the launch platform.
2. The kite's motion can be controlled through the manipulation of its angle of attack, induced roll angle, and the magnitude of the tether tension force.
3. The kite is neutrally buoyant, *i.e.*, there is zero net impact of gravitational and buoyancy forces on the kite.

The forces acting on the kite are the lift, $\vec{L}$, drag, $\vec{D}$, and tension $\vec{T}$ forces (this assumes that that kite's yaw dynamics induce a fast and stable weathercock effect, and thereby we can ignore the side forces).

$$\vec{F}_{total} = \vec{L} + \vec{T} + \vec{D}$$

Taking the angle of attack, α, induced roll angle, ϕ, and the tension T as inputs, the equations of motion can be written as:

$$\frac{d}{dt}\begin{bmatrix} x \\ y \\ z \\ u \\ v \\ w \end{bmatrix} = \begin{bmatrix} u \\ v \\ w \\ \frac{1}{m}\vec{F}_{total}\cdot\hat{i} \\ \frac{1}{m}\vec{F}_{total}\cdot\hat{j} \\ \frac{1}{m}\vec{F}_{total}\cdot\hat{k} \end{bmatrix}$$

Based on Equation (2), the optimization statement can be written as follows:

$$\min J = \frac{1}{t_f - t_i}\int_{t_i}^{t_f}(-w_p P_{mech} + J_{rate} + J_\alpha + J_T + J_\phi)dt$$

subject to the kite dynamics plus the constraints:

$$\vec{X}_{ti} = \vec{X}_{tf}$$

$$P_{mech} = \vec{T}_T\vec{V}$$

Since, this was a periodic optimal control problem, the state was expressed as a truncated Fourier series. The vectors $a(n)$ and $\vec{b}(n)$ are expansion coefficients corresponding to the n^{th} harmonic of the Fourier expansion. In this work, n is chosen to be 3 for simplicity. The period of the Fourier series is $T_{period} = t_f - t_i$. Expressing the state as a Fourier expansion allows for the optimization of the initial kite position and velocity, as part of trajectory optimization. Thus, the coefficient vectors $\vec{a}(n)$, $\vec{b}(n)$, and the time period T_{period} become the optimization variables.

$$\vec{X} = \frac{\vec{a}\,(0)}{2} + \sum_{n=1}^{3}\left[\vec{a}\,(n)\cos\frac{2\pi n}{T_{period}} + \vec{b}\,(n)\sin\frac{2\pi n}{T_{period}}\right]$$

The results showed that the optimization algorithm that incorporates the inverse dynamics solution and the 3-DOF kite model, successfully furnishes a trajectory with desirable power production. A kite of similar area would theoretically produce a maximum of 83.9kW of power during steady state reel out. The optimization algorithm was able to produce an average power of 21.3kW within one time period. Figure 25 further shows that the kite consumed very little power during reel-in, never exceeding 3kW. Moreover, during reel out, the kite was able to produce instantaneous power much higher than the steady state theoretical limit, reaching almost 60kW. Therefore, the kite was able to achieve a Loyd factor, defined as the ratio of the generated power to the theoretical power, of 25.38%.

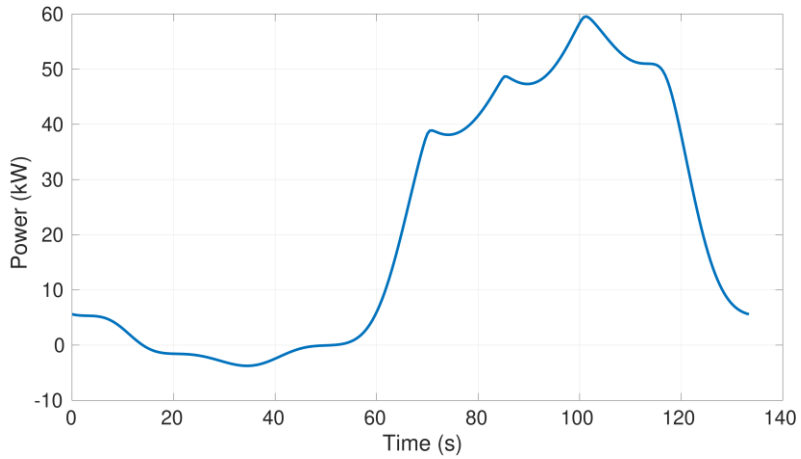

Figure 25: Power produced by the kite

The kite followed a simple trajectory of a short reel-out and reel-in episode, before being reeled-out for a longer period of time, as shown in Figure 26. It is assumed that the kite's anchor point is sufficiently underwater such that the kite does not rise above the surface as it traverses this trajectory.

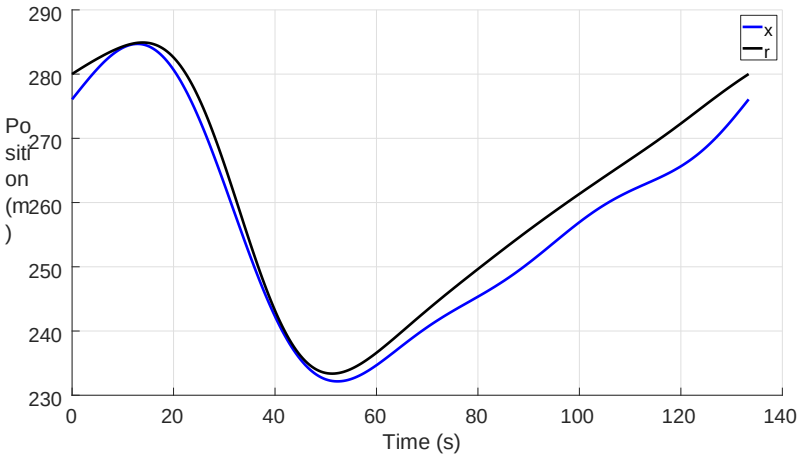

Figure 26: Longitudinal position (x) and tether length (r) vs. time.

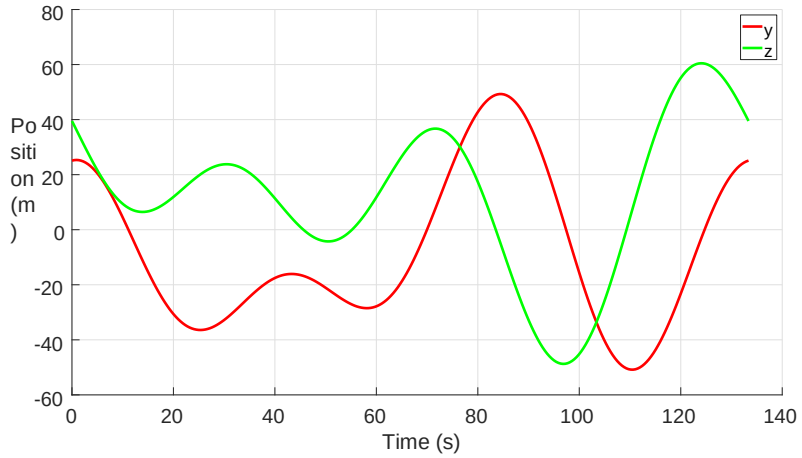

Figure 27: Lateral position (y) and depth (z) of kite

The full trajectory, as seen in Figures 27 and 28, is not figure-8, and can be approximated as a sequence of circles in the yz-plane. The non-figure-8 path shape eliminates the need for switching the direction of induced roll, which is attractive from the perspective of minimizing the rates of change of various actuation inputs. Moreover, this shape is acceptable due to the fact the kite is neutrally buoyant, and therefore does not need to exploit the potential safety benefits of a figure-8 trajectory where the kite turns upwards (as opposed to downwards) when it turns. As seen again, the radius of curvature is very tight, which can be attributed to the fact that the following two properties were neglected in the analysis: (i) the variation in relative velocity across the wing span and (ii) potentially unrealistic yaw rate.

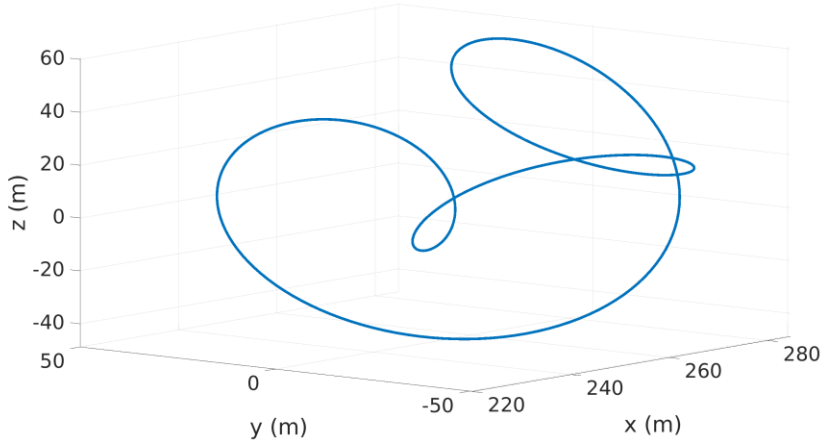

Figure 28: Optimized path shape

As shown in Figures 29 and 30, the velocity of the kite in the yz-plane is larger than in the x-direction, thereby showing that the kite is exploiting cross-current motion substantially. The speed with which the kite reels in and out, $\dot{r}$, does not always equal the speed of the kite parallel to the free-stream velocity, $\dot{x}$. This implies that the kite achieves a non-trivial portion of its reel-in/out motion by traveling either towards or away from the origin in the yz-plane. Such in-plane reel-in/out motion is intuitively attractive because it minimizes the total distance required for kite operation parallel to the free-stream fluid velocity. The

optimal velocity for the kite to produce maximum power should be $\frac{1}{3}$ of the free stream velocity, which in this case is $\frac{1}{3}\mathrm{m\,s^{-1}}$. The kite's transient reel-out speeds are slightly higher, enabling higher levels of power generation during transient reel-out.

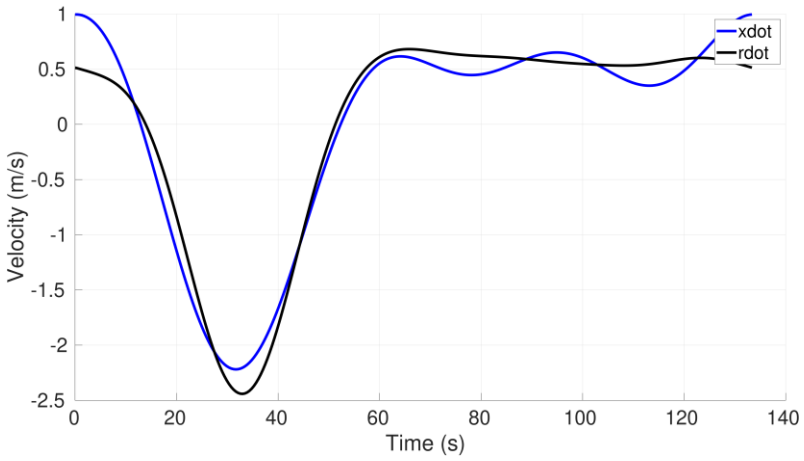

Figure 29: Rate of change of longitudinal position (xdot) and spooling velocity (rdot).

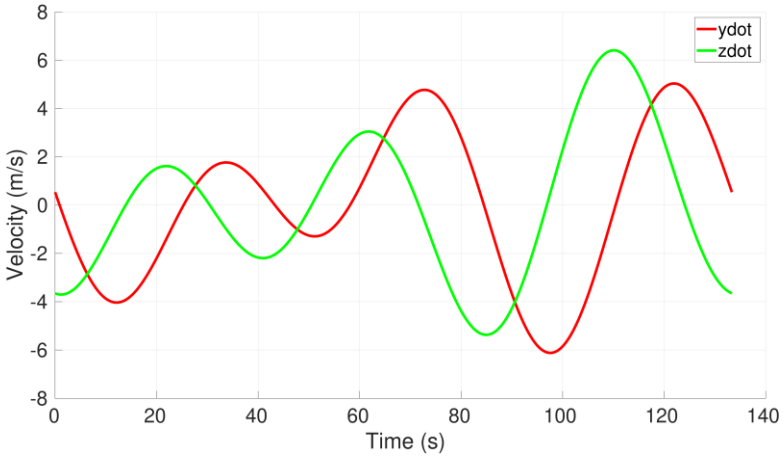

Figure 30: Lateral (red) and vertical (green) velocity of the kite

During spool-out, the angle of attack reaches a relatively high value, ensuring a high lift-to-drag ratio, as shown in Figure 31 and Figure 32. This also ensures that during spool-out, the tension is at a maximum, as seen in Figure 33. During spool-in, the angle of attack becomes negative, and the tether tension at the corresponding time reaches its minimum value.

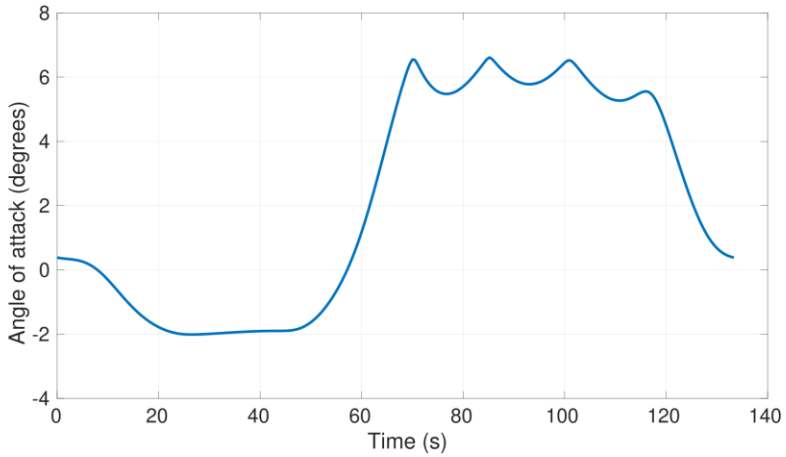

Figure 31: Angle of attack vs. time

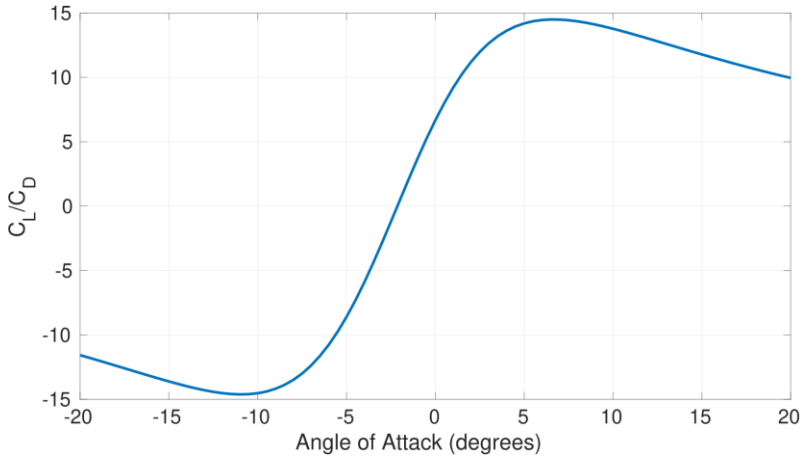

Figure 32: Lift-to-drag ratio vs. angle of attack

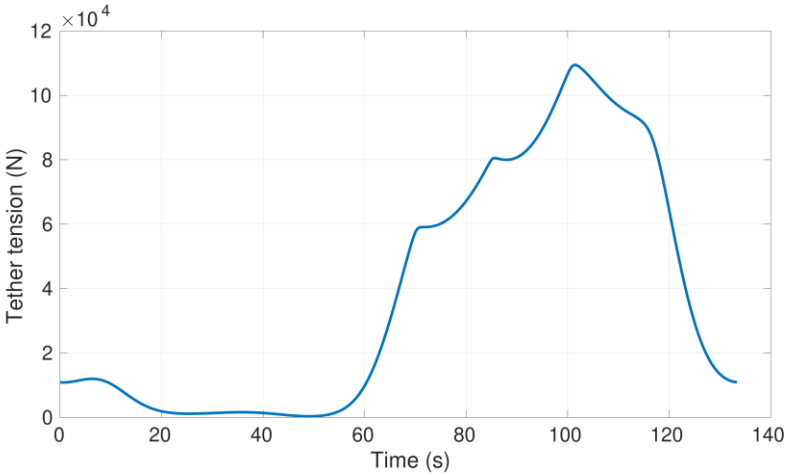

Figure 33: Tether tension vs. time

The roll angle does not change sign during the duration of the trajectory, and reaches a maximum value during spool-in, as shown in Figure 34. This causes the tether tension and lift vector to be misaligned, and thereby ensures low tension spool-in.

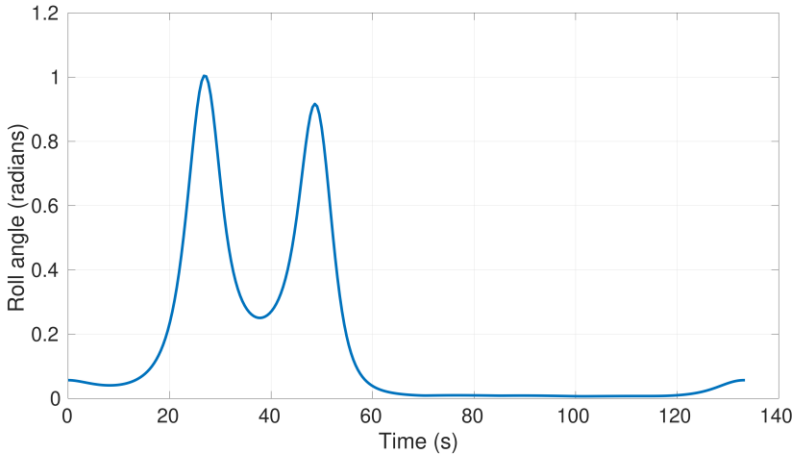

Figure 34: Roll angle vs. time

The above results are appealing for at least four reasons. First, from a fundamental perspective, the results represent the first optimization study where both spooling and cross-current motion were co-optimized using direct transcription, with an underlying analytic solution of the inverse kite dynamics. Second, from a practical perspective, the results furnish a kite trajectory that confirms the attainability of significant energy harvesting through cross-current motion, confirming earlier findings by the author based on an approximate solution of the kite dynamics. Third, the results provide new insights into the shape of the optimal kite trajectory. In particular, they highlight the degree to which circular trajectories can potentially provide energy harvesting benefits similar to those seen in the literature with figure-8 trajectories. Moreover, they highlight the degree to which kite reeling motion can take place, at least partially, in plane, as opposed to in alignment with the free-stream fluid velocity. This is particularly attractive from the perspective of multi-kite spacing in a farm of kites, where the smaller the total distance taken up by each kite in the free-stream fluid direction, the greater the potential for maximizing effective overall farm power density.

5 Combined Plant, Site, and High-Level Control Co-Design

An energy-harvesting kite system consists of three primary subsystems:

1. Control, which modulates the system's operation variables to execute cross-current flight in the prescribed path, perform spooling operation, and adjust operating depth.
2. Plant, which includes the geometric and structural attributes of the kite (lifting body) and tether.
3. Environment, which comprises the flow conditions as functions of spatial location (which is dictated through the site selection (fixed for all time) and depth (continuously variable)) and time.

Given the strong bidirectional coupling between three subsystems, a co-design-based methodology is required to avoid system-level sub-optimality or constraint violation. A multi-fidelity co-design framework was developed to optimize the MHK kite system.

5.1 Overall Problem Formulation

The effectiveness of a renewable energy harvesting system is often quantified with techno-economic metrics like generated power, structural mass or levelized cost of energy (LCOE), which combine technical performance with economic cost/profitability or a surrogate thereof. This work presents a system optimization that maximizes the weighted power-to-mass ratio. The weighting term manages the trade-off between generated power maximization and structural mass minimization, the latter of which has been estimated to be well-aligned with capital cost minimization. The overall co-design problem is formulated as:

$$\begin{aligned} \min_{\boldsymbol{u}} \quad & \frac{P^{w}_{gen,avg}}{m_{kite}} \\ \text{subject to:} \quad & C_{st}(\boldsymbol{u}) \leq 0 \\ & m_{kite}(\boldsymbol{u}) \leq \rho V_{kite}(\boldsymbol{u_p}) \\ & u_{min} \leq \boldsymbol{u} \leq u_{max} \end{aligned}$$

where $P_{gen,avg}$ is the time-averaged generated power (over a 12-month simulation period), m_{kite} is the kite's structural mass, w is a user-defined relative weighting term (= 1 for this work) , V_{kite} is the geometric volume of the kite (function of plant decision variables). The first equation set represents the structural constraint (wing and fuselage) functions, the second is the buoyancy constraint, and the third specifies the set of bounds on the decision variables. The inequality is modeled as an inequality constraint, as "cheap" ballast mass can be added to achieve the targeted neutral buoyancy. The full set of decision variables considered in the overall optimization is listed in Table 5 below.

Variable	Description	Unit	System Constituent
s	Wingspan	M	Plant
AR	Wing aspect ratio	-	Plant
N_{sp}	Number of wing spars	-	Plant
t_{sp}	Thickness of wing spars	% of c	Plant
t_{sw}	Thickness of wing shell	% of t	Plant
D	Diameter of fuselage	M	Plant
L	Length of fuselage	M	Plant
t_{sf}	Thickness of fuselage shell	% of D	Plant
θ_{el}	Elevation angle setpoint	Rad	Control
l_{thr}	Tether length setpoint	M	Control
u_{spl}	Spool rate	m/s	Control
x	Longitude index of site	-	Site
y	Latitude index of site	-	Site

Table 5: Critical co-design variables

Site details:

The environment consists of the flow regime that the kite system operates in to generate power. This work considers a portion of the Gulf Stream in the vicinity of Cape Hatteras, NC. The region of interest (ROI) -- bounded by the latitudes 32.736° and 35.2400° N, and longitudes 74.23° and 76.90° W -- was chosen based on extensive past research on ocean current energy harvesting potential (e.g., [17]).

Data generated from an oceanographic hindcast model, the Mid Atlantic Bight and South Atlantic Bight (MABSAB) ocean model, were used to model the flow environment in the ROI. The ROI was sub-divided into a 50x50 grid, with each point corresponding to a potential deployment site.

Control details:

The controller has two primary components: (1) depth control, which adjusts operating depth to optimally harvest the flow resource; (2) power generation, which achieves power-augmenting cross-current flight via path-following (flight) and spooling (winch) control. The latter component is implemented through the flight efficiency map (control proxy function) that was previously described.

The depth controller finds the optimal operating depth to maximize power generation by adjusting the operating tether length l_{thr}, elevation angle θ_{el}, and spooling rate u_{spl}. The optimal vector of depth control variables $\boldsymbol{u}_{\boldsymbol{d}}^{*}(k)$ is computed at each time step, k, as:

$$\boldsymbol{u}_{\boldsymbol{d}}^{*}(k) = \arg\max_{\boldsymbol{u}_{\boldsymbol{d}}} P_{gen}(k)$$

5.2 Control Proxy Function for Enabling Fast Co-Design

The flight performance is primarily characterized by the SFOT. Thus, the decision variables for the SOFT, wingspan (s) and wing aspect ratio (AR), dictate flight performance. To capture the behavior of the closed-loop flight controller over the whole design space, a sensitivity analysis was done by mapping the flight efficiencies to be used to approximate a function $\eta(s, AR)$. The results of the sensitivity analysis, the efficiency map, is shown in Figure 35**.**

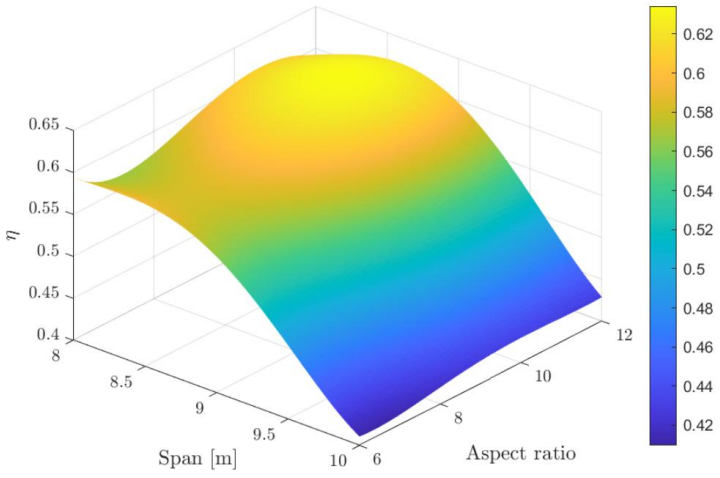

Figure 35: Results of the control proxy function efficiency mapping

5.3 Nesting and Layering Approaches to Co-Design

An integrated co-design framework combines the plant (geometric and structural sizing tools), site-based flow modeling, and controller details. To achieve a simultaneous optimization implementation two primary approaches are used: (1) nesting, and (2) layering.

Nesting:

A *tri-level nested* solution strategy is considered to combine the analysis tools of the three sub-systems, as shown in Figure 36. The approach nests the control optimization within the plant optimization, which in turn is nested within the site selection module. The site location (indexed by x, y coordinates within the ROI) is varied in an outer loop, which is used to compute the time- and depth-varying flow field for the location ($v(t,d)$). After defining the flow environment, the plant parameters are optimized by integrating the plant optimization modules discussed in the previous sections. However, the geometric tool (SFOT) requires the operating tether length (l_{thr}), elevation angle (θ_{el}), and flow velocity (v) to be defined to estimate the instantaneous power generated ($P_{gen}(t)$). Thus, the depth optimization is nested within the geometric sizing tool to compute the optimal operating depth parameters ($\boldsymbol{u}_{\boldsymbol{d}}^{*}$), corresponding performance (P_{gen}^{*}), and load (F) trajectories experienced during the simulation period. The geometric configuration (u_{geo}) and the computed maximum load (F_{max}) are then fed to the structural tools, which ultimately optimize the design and compute the resulting structural mass (m_{kite}). The optimization progresses until an optimal site-kite design combination is found.

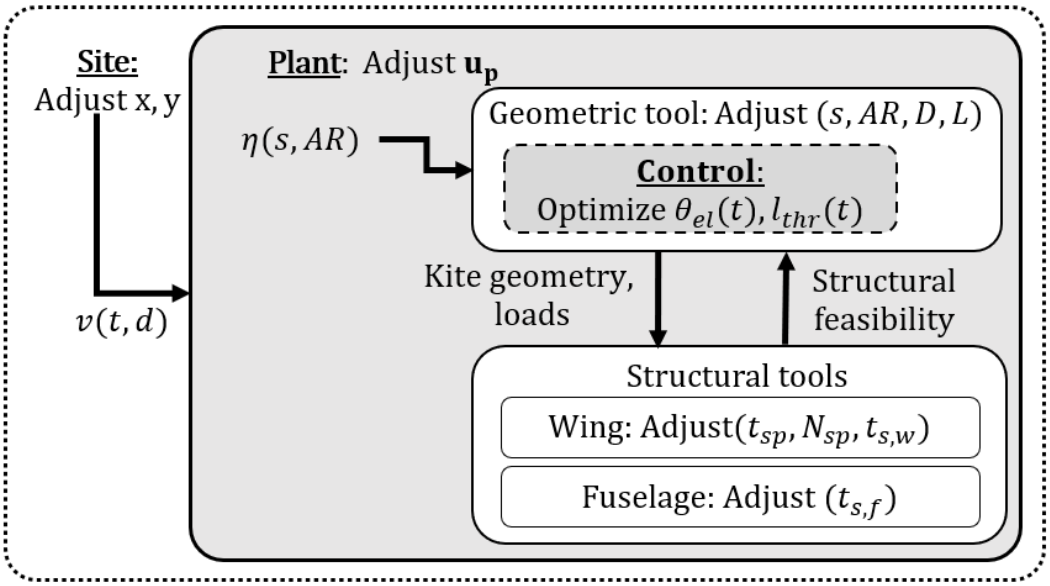

Figure 36: Nesting-based integrated co-design framework: The site, plant and control iteration loops are respectively denoted with dotted, solid and dashed lines.

Layering:

To further reduce computational cost, a layer strategy was proposed where a full optimization is performed at multiple model fidelities. Each model fidelity is based on the depth control strategy used, how often the variables are adjusted, and whether or not spooling dynamics are considered. Each model has an associated error bar on performance, and the design space is progressively reduced with increase

in model fidelity based on these confidence intervals. Thus, a large design (full site design space) is first explored with a low fidelity (LF) model which can be done quickly but isn't very accurate, then the space is reduced based on the associated error bar. The medium fidelity (MF) model is then used to explore the smaller design space; and finally, the even smaller design space is explored using the higher fidelity (HF) model to find the optimum (or a set of optimum points) system(s).

For $i = 1{:}3\ [LF, MF, HF]$

Run nested integrated optimization;
Append error bars to the results;
Perform error-bar based site design space reduction;
Store results;

end

5.4 Results

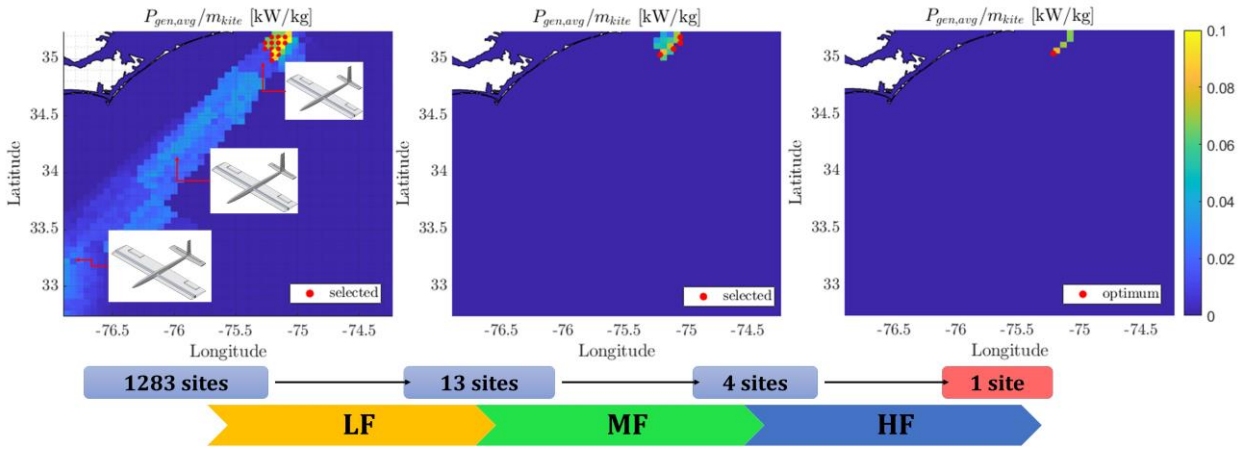

Figure 37: Site design space reduction using the proposed multi-fidelity optimization approach (layering)

Figure 37 illustrates the progression of the optimization, where the power-to-mass ratio of the optimal kite design for each candidate site, simulated at each layer's fidelity, is shown. The full site design space was explored in the LF layer ($i = 1$), following which the sites were reduced from the 1283 to 13 sites. The MF layer ($i = 2$) evaluated the reduced design space, further reducing the candidate site count to 4 sites. Finally, the HF layer ($i = 3$) evaluated the 4 sites to find the optimum. Note that each site location has an associated optimal kite design and optimal control trajectory. The CAD renderings of the resulting designs at certain sites are shown where the larger kite designs correspond to sites with greater seabed depths.

The resulting optimal kite has a low aspect ratio wing design. The average power generated over the 12-month period was 28 kW, and the resulting kite structural mass was 350 kg. As a reminder, only the masses of the structural support members that significantly contribute to manufacturing costs are considered. The resultant power-to-mass ratio translates to a 1200 kg of structural mass for a 100-kW system.

The optimal control trajectories of target tether lengths and elevation angles are shown in Figure 38. It is seen that the control trade-off resulted in shallower depth operation via higher elevation angle flight (as opposed to higher tether length or higher depth operation). The results show that the performance

penalties due to additional drag at higher tether length operation are outweighed by those due to *cubic cosine losses* associated with misaligned flight operation.

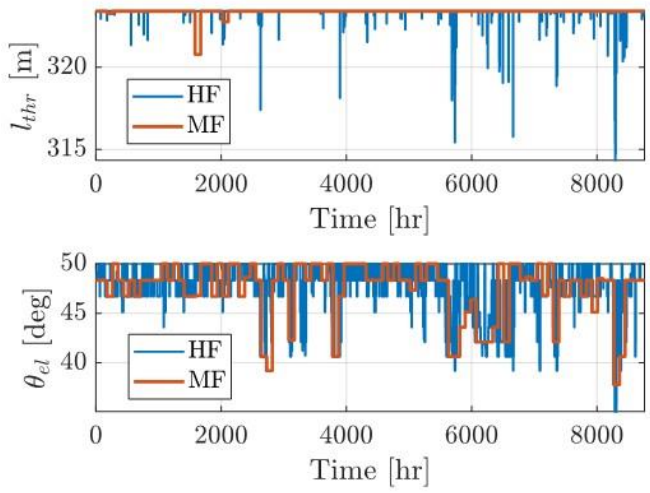

Figure 38: Optimal control input trajectories. The maximum admissible values of l_{thr} and θ_{el} are 2000 m and 50°, respectively.

6 Water Channel-Based Experimental Validation

6.1 Summary of Water Channel Capabilities

Kite individual component experimental testing was conducted in the North Carolina State Free Surface Water Tunnel. The tunnel is a closed-circuit water tunnel that is constructed of fiberglass-foam composite panels. The tunnel contains a 24" x 32" x 96" (61 x 81.3 x 243.8 cm) all glass test section and uses a three-sided contraction of 4.5:1 to produce a freestream velocity of 0.15 < U∞ < 0.97 m/s with a u-velocity turbulence intensity of 0.5-0.8%.

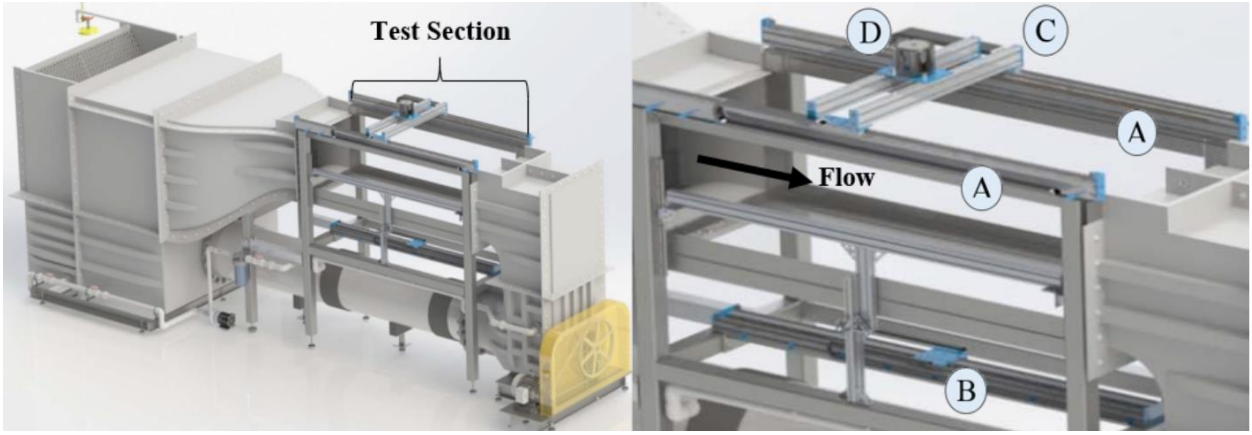

Figure 39: Left: water tunnel model. Right: test section with motion system rails and rotary motor.

Flow quality is conditioned through two plastic honeycomb screens and three stainless steel anti-turbulence meshes. The tunnel is equipped with a dual X-axis gantry powered by H2W Single Rail Linear Stages.

The tunnel is equipped with a H2W motion system controlled by a Galil 4080 controller and Xenus XTL-230-36 amplifiers operated using Galil Suite software. Custom programs downloaded into the controller or manual jogged input determine the motions of the test article with respect to the freestream velocity. The controller utilizes the amplifiers to change magnetic fields on the various rails and rotary motor with location encoder feedback to meet the specified programmed motion for the experiment. If the motors exceed a given position tolerance an error occurs and the test is stopped. A dual-axis gantry denoted twice

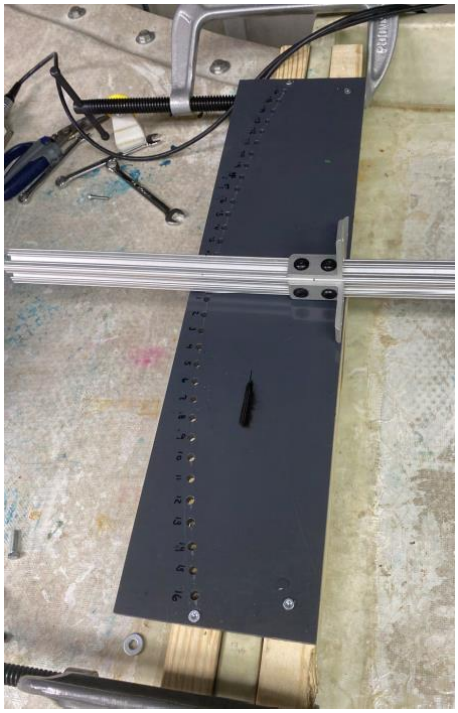

Figure 40: Manual pitching mechanism used for 1/10th scale component testing.

by (A) on the right in Figure 40, is powered by two H2W Single Rail Linear Stages. This dual stage allows the test article to surge into and away from the freestream velocity as the flow exits the contraction from left to right. The gantry is placed 20 cm above the free surface water line and spans the entire length of the test section. The gantry has a max continuous output of 294 N and a peak output of 880 N. Beneath the test section floor is a H2W Dual Rail Linear Stage (DRS), denoted by (B), aligned with the centerline of the test section. The DRS rail system is designed where motion inputs of the test article can be tracked using cameras and other hardware during the specified motion. The DRS stage spans the entire length below the test section and has a continuous output of 44 N. A second dual rail stage spans the width of the test section, denoted by (C), allowing the test article to plunge. The rotary motor, denoted by (D), allows the test article to pitch. The motion system uses RLS LM 13 linear magnetic encoders as feedback position sensors with a resolution of 1 micrometer for the linear rails and a rotary encoder with 1/125th of a degree resolution for the rotary motor.

A manual pitching mechanism was utilized for this experiment of 1/10th scale components from -16 to 16 degrees in 1 degree increments. The 8020 aluminum rail pivot point is at the test article location in the

water tunnel test section, where the holes in the acrylic plate correspond to repeatable angle of attack locations.

6.2 Force and Moment Testing for Steady Hydrodynamic Characterization

The experimental setup of the scale kite model components were isolated by mounting struts connected to a load cell in the water tunnel for force and moment testing. The components are the wing, stabilizers, fuselage only, and fuselage with additional tether connections. The additional tether connections included the servo arm wire bundle, bridle, and tether connector. The intent was to characterize the individual contributions of these components for lift, drag, and pitching moment to experimentally inform the Simulink model hydrodynamic predictions.

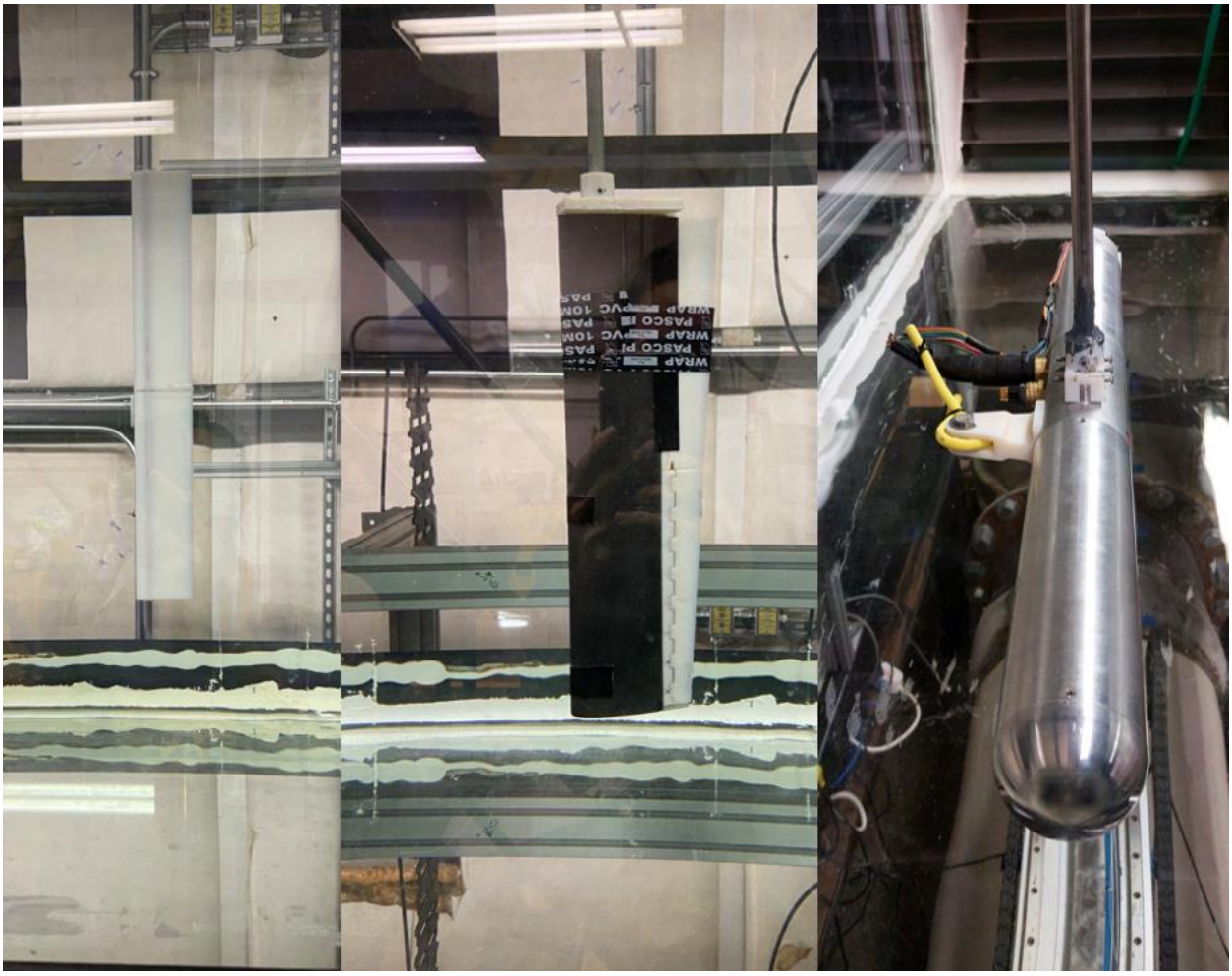

Figure 41: From left to right; the elevator, wing, and fuselage with tether components as vertically strut mounted in the water tunnel.

The strut assemblies of the fuselage, wing, and horizontal stabilizer cross-sectional area were 3.18 %, 5.5 %, and 1.24 % of the total water tunnel cross-sectional area, respectively. The static blockage for these three components are less than the nominally recommended 10 % blockage ratio. An ATI Gamma 6-axis load cell was used to measure forces and moments produced by these components at velocities of: 0.50, 0.75, and 0.95 m/s flow. These speeds were chosen to capture the maximum velocity of the water tunnel

and provided different Reynolds numbers to represent different flow regimes to investigate the hydrodynamic forces' consistency. The load cell was mounted above the test objects, so that it rotated with the change in angle of attack. Load cell measurements of the struts were recorded and subtracted from the overall measurements of the different components. The equations below were used to determine the lift, L and drag, D force acting on the components at each angle of attack, where A is the axial force, N is the normal force, and α is the angle of attack.

$$L = N\cos\alpha - A\sin\alpha$$

$$D = N\sin\alpha + A\cos\alpha$$

The forces were measured with a National Instruments NI PXIe-6363 I/O module using a LabVIEW DAQ system with a 10 kHz sampling rate. The freestream tunnel velocity was produced with a 10 hp Baldor Reliance Super E Motor EM3774t controlled with an ABB ACS355 variable frequency drive. For each velocity, the angle of attack was varied from -16 to 16° at 1° increments using a manual rotary stage. Force and moment data were recorded for 20 seconds and averaged to produce each experimental test point. Table 6 displays the test parameters for the water channel experiments.

Parameters	Units	Description
Kite Component	-	Wing, Horizontal Stabilizer, Fuselage Only, Fuselage with Tether Components
Hydrodynamic Coefficient	-	Lift, Drag, and Pitching Moment
Angle of Attack	degrees	−16 to 16, 1° Increments
Velocity	m/s	0.5, 0.75, 0.95

Table 6: Variable test parameters for water channel experiments.

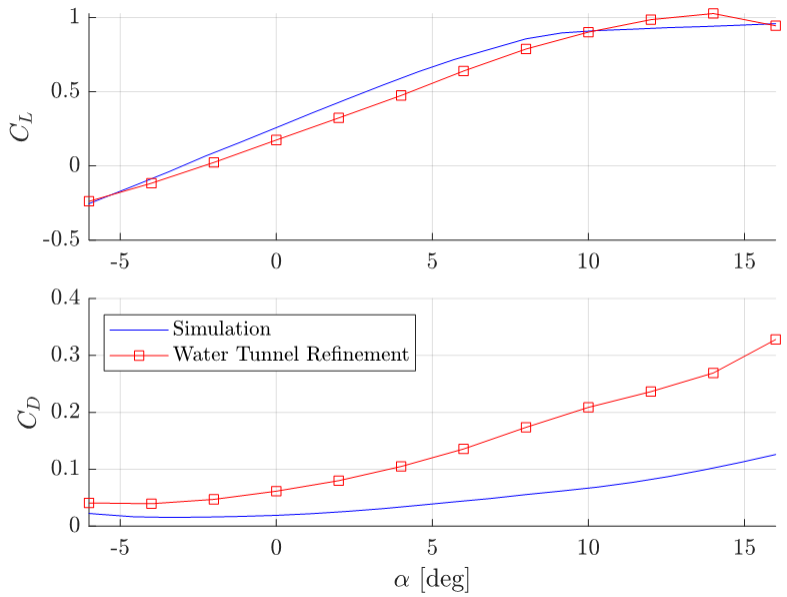

Figure 42: Top: static wing lift coefficient vs. angle of attack. Bottom: static wing drag coefficient vs. angle of attack.

The sweep of angle of attack for the components tested yielded consistent results across all water tunnel velocities. This result demonstrated that constant values for lift and drag for the tail surfaces, wings, and fuselage could be implemented for any expected flow conditions. From the wing and fuselage lift and drag coefficient plots (note that fuselage lift is negligible and is on par with measurement noise; however, fuselage drag is significant) it can be seen that the main contributor and largest discrepancy from the initial hydrodynamic characterizations is due to drag. The lift induced drag of the wing contributed to approximately 65 % of the drag discrepancy, where the fuselage is 20 – 25 %, and the fuselage connectors contributed the remaining 10 - 15 %.

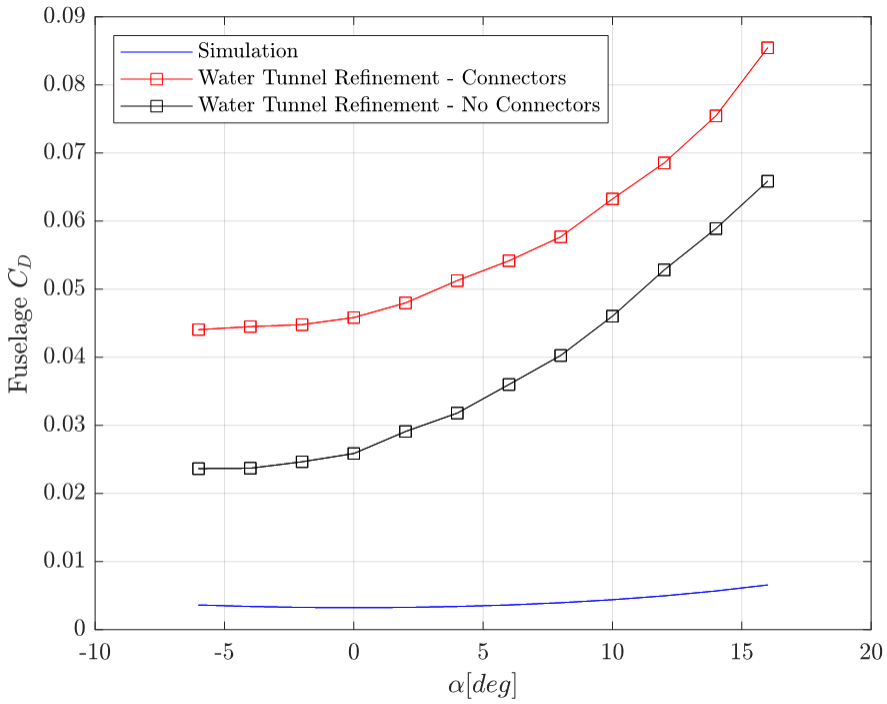

Figure 43: Static fuselage drag coefficient vs. angle of attack for the original simulation, experimental fuselage with no connectors, and the experimental fuselage with connectors.

Following the wing and fuselage individual component explanations it is shown that the aggregate kite lift is slightly over-predicted in simulation prior to 10° angle of attack, where the experimental combined values show a slightly delayed stall location at ~14°.

The magnitude of the aggregate lift is also slightly better than prediction exceeding a value just above one with respect to the kite wing area. This consistency between experiment and initial hydrodynamic characterization is contrasted by the drag discrepancies previously mentioned for the wing induced drag and fuselage with connectors. In the remaining three aggregate plots these drag components account for the vast majority of the differences for the kite drag coefficient, ${C_L}^3/{C_D}^2$, a key kite performance metric, and C_L/C_D, the lift to drag ratio.

The result was that the kite simulation predictions compared to the experiment were greatly improved for key parameters: azimuth, elevation, and velocity augmentation. An example of this improved

prediction accuracy can be seen in the last section figure for all three key parameters. With utilization of these refined experimental, static, hydrodynamic characterizations for the wing, tail surfaces, and the fuselage with connectors correlation between cross-current experimental results and simulation have been significantly improved. This supported the implementation of the static component hydrodynamic characterization to refine the Simulink simulation results and improve performance predictions.

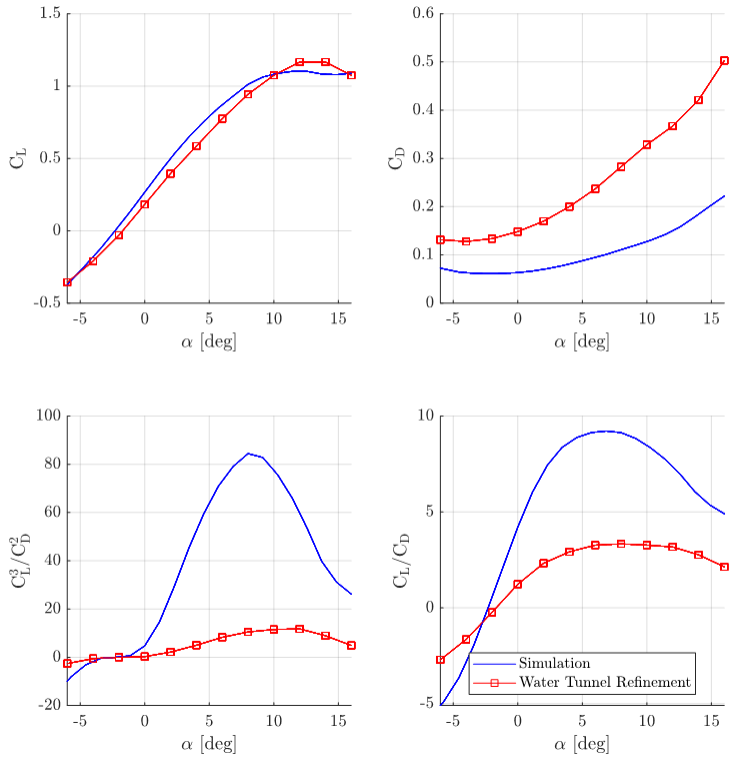

Figure 44: Static aggregate 1/10th scale kite values vs. angle of attack for the original simulation and experimental values. Top left: lift coefficient, top right: drag coefficient, bottom left: $C_L{}^3/C_D{}^2$, bottom right: C_L/C_D, lift to drag ratio.

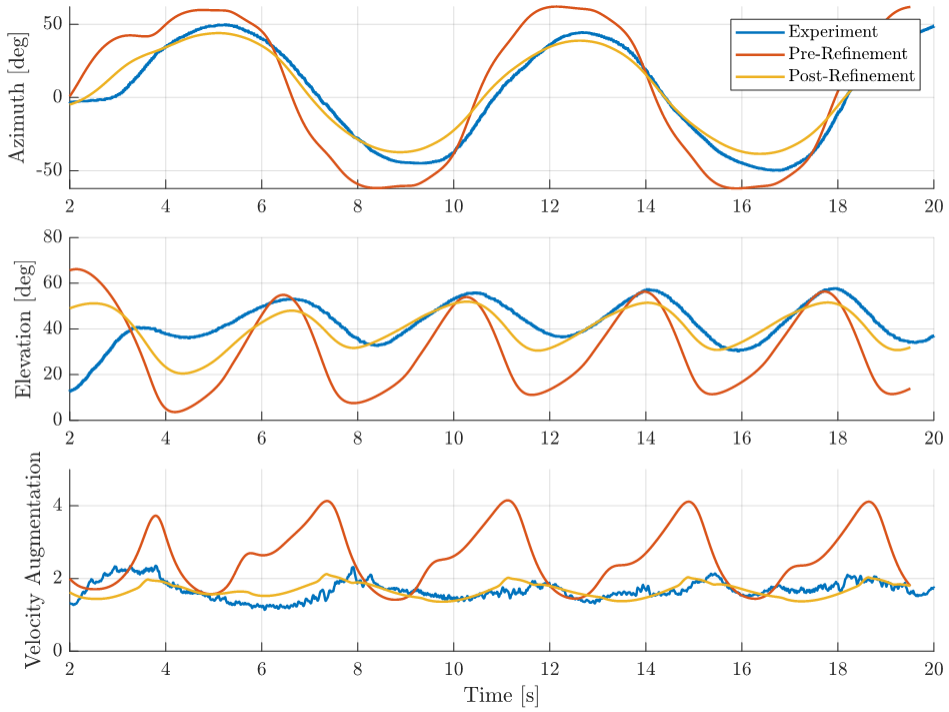

Figure 45: Comparison of dynamic flight performance as measured in experiments, versus simulated dynamic performance before and after model refinements were made.

6.3 Controlled Motion Experiments for Unsteady Hydrodynamic Characterization

Tether characterization: Two main goals/objectives were posed regarding the tether hydrodynamics. The first objective was to determine:

1. *Are we flying at a frequency that is close to the natural vortex shedding frequency?*

This was answered by performing controlled motion experiments that used simulation data. The simulation data was post-processed to derive relevant non-dimensional parameters such as Reynolds number, Strouhal number, and natural vortex shedding frequency. The flow parameters derived from the simulation data and used for the experiments are shown in Table 7.

Simulation - Flow Parameters				
Diameter (m)	Flow Velocity (m/s)	Re Number	Strouhal Number	Shedding freq. (Hz)
0.0144	0.50133	7204.743	0.209939	7.308945
0.0144	1.00059	14379.74	0.204683	14.222483
0.0144	2.00706	28843.98	0.201338	28.062384

Experiment - Flow Parameters				
Diameter (m)	Flow Velocity (m/s)	Re Number	Strouhal Number	Shedding freq. (Hz)
0.0605	0.11973	7229.207	0.209911	0.415416
0.0605	0.23739	14333.43	0.204687	0.803151
0.0605	0.47748	28829.88	0.201339	1.589011

Table 7: Flow parameters from dynamic model simulations and parameters used for water channel experiments.

For the prescribed motion tests, harmonic motions were fitted against the Lemniscate of Booth that was utilized as the figure-8 path to track in the simulations. Figures 46 and 47 show the harmonic fitting against the Lemniscate of Booth. The RMSE in the x-direction ($RMSE_x$) was ± 4.14 meters and the RMSE in the y-direction ($RMSE_y$) was ± 7.39 meters.

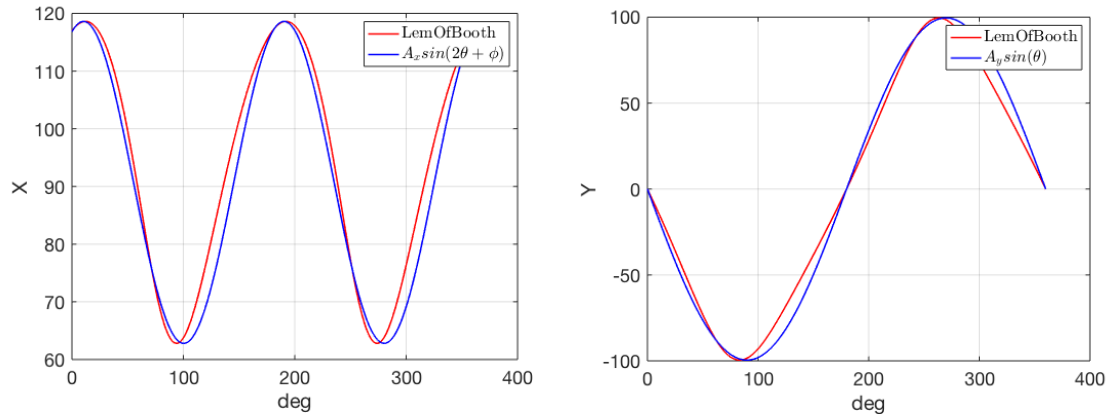

Figure 46: Trajectory (versus phase angle) in the direction parallel to the flow (left) and transverse to the flow (right).

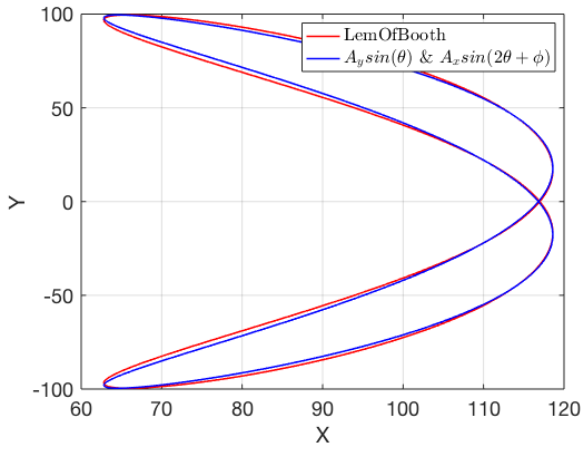

Figure 47: Path flown in the water channel, where x is aligned with the flow and y is transverse to the flow.

Using the simulation data that was provided, normalized amplitudes and frequencies in both X and Y were extracted. These normalized amplitudes and frequencies were essential to perform the controlled motion experiments. The extracted parameters are shown in Table 8, and the parameters used for the experiments are shown in Table 9. Note that Cases 11-13 are equivalent to Cases 4-6, except that the amplitudes in x- and y-directions, A_x and A_y, were downscaled by $2000D$ to observe if wall-effects are present in Cases 4-6 (A_x and A_y are close to the water tunnel physical constraints).

Run #	Tether Length (m)	Flow Speed (m/s)	Ax (m)	Ay (m)	fx (Hz)	fy (Hz)	Shedding Frequency (Hz)	Period (sec)	Ax/(1000 *D)	Ay/(1000 *D)	fx/fs	fy /fs
1	100	2	25.927	83.670	0.01815	0.01805	28.06238	55.0978	1.801	5.810	0.00065	0.00064
2	90	1	22.062	74.425	0.01057	0.01059	14.22248	94.61437	1.532	5.168	0.00074	0.00074
3	80	2	21.139	67.538	0.02404	0.02385	28.06238	41.60597	1.468	4.690	0.00086	0.00085
4	70	1	17.137	58.190	0.01441	0.01437	14.22248	69.40503	1.190	4.041	0.00101	0.00101
5	60	2	16.192	51.224	0.03335	0.03316	28.06238	29.98273	1.124	3.557	0.00119	0.00118
6	60	1	14.746	50.121	0.01723	0.01714	14.22248	58.0541	1.024	3.481	0.00121	0.00121
7	50	0.5	12.149	41.483	0.01021	0.01023	7.308945	97.97845	0.844	2.881	0.00140	0.00140
8	50	1	12.424	41.9990	0.02113	0.02108	14.22248	47.3289	0.863	2.917	0.00149	0.00148
9	40	0.5	9.776	33.288	0.01299	0.01300	7.308945	76.9881	0.679	2.312	0.00178	0.00178
10	30	0.5	7.445	25.174	0.01736	0.01744	7.308945	57.60001	0.517	1.748	0.00238	0.00239
11	70	1	17.137	58.190	0.01441	0.01437	14.22248	69.40503	1.190	4.041	0.00101	0.00101
12	60	2	16.192	51.224	0.03335	0.03316	28.06238	29.98273	1.124	3.557	0.00119	0.00118
13	60	1	14.746	50.121	0.01723	0.01714	14.22248	58.0541	1.024	3.481	0.00121	0.00121

Table 8: Parameters extracted from simulation data.

Run #	Flow Speed (m/s)	Ax/(1000 *D)	Ay/(1000 *D)	Ax/D Adjusted	Ay/D Adjusted	Ax (m)	Ay (m)	fx/fs & fy/fs	Shed. Freq (Hz)	fx & fy (Hz)	Period (min)	3 Cycles Period (min)
1	0.47748	1.8005	5.8104	0.9003	2.90521	0.05447	0.17577	0.0006468	1.589011	0.001028	16.21738	48.65214
2	0.23739	1.5321	5.1684	0.7660	2.58420	0.04635	0.15634	0.0007431	0.803151	0.000597	27.9244	83.77321
3	0.47748	1.4680	4.6901	0.7340	2.34507	0.04441	0.14188	0.0008565	1.589011	0.001361	12.24622	36.73867
4	0.23739	1.1900	4.0409	1.1900	4.04094	0.07200	0.24448	0.0010131	0.803151	0.000814	20.48414	61.45242
5	0.47748	1.1245	3.5572	1.1245	3.55719	0.06803	0.21521	0.0011885	1.589011	0.001889	8.825059	26.47518
6	0.23739	1.0240	3.4807	1.0240	3.48066	0.06195	0.21058	0.0012111	0.803151	0.000973	17.13404	51.40211
7	0.11973	0.8437	2.8807	0.8437	2.88074	0.05104	0.17428	0.0013964	0.415416	0.000580	28.73101	86.19304
8	0.23739	0.8628	2.9166	0.8628	2.91660	0.05220	0.17645	0.0014856	0.803151	0.001193	13.96861	41.90583
9	0.11973	0.6789	2.3117	0.6789	2.31168	0.04107	0.13986	0.0017771	0.415416	0.000738	22.57584	67.72753
10	0.11973	0.5170	1.7482	0.5170	1.74821	0.03128	0.10577	0.0023753	0.415416	0.000987	16.89052	50.67155
11	0.23739	1.1900	4.0409	0.5950	2.02047	0.03600	0.12224	0.0010131	0.803151	0.000814	20.48414	61.45242
12	0.47748	1.1245	3.5572	0.5622	1.77860	0.03402	0.10760	0.0011885	1.589011	0.001889	8.825059	26.47518
13	0.23739	1.0240	3.4807	0.5120	1.74033	0.03098	0.10529	0.0012111	0.803151	0.000973	17.13404	51.40211

Table 9: Parameters used for the controlled motion experiments.

To determine the existence of lock-in, the C_L spectra must be observed. The C_L spectra for the cases observed is shown in Figure 48. The presence of lock-in is defined by sharply defined spectral peaks (typically higher than 0.5).

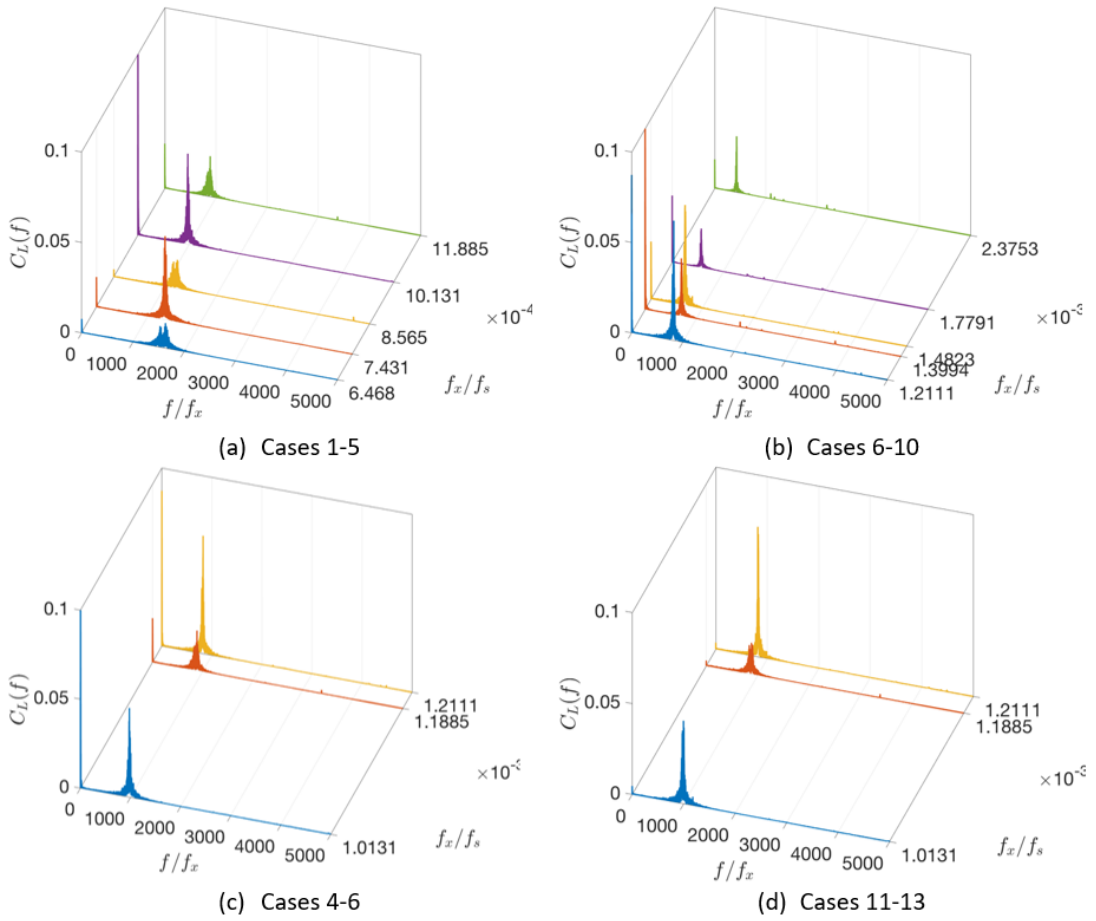

Figure 48: C_L spectra for Cases 1-13.

The C_L spectra results demonstrate that lock-in is not present, as expected, because the motion was very slow compared to the vortex shedding frequency. The amplitude of the spectral peaks is typically higher than 0.5 for cases where lock-in is present, and that is not the case for the current runs. In Figures 48(a) and 48(b), Cases 4-7, and 9 (f_x/f_s = 0.001013, 0.001189, 0.00121, 0.001399, and 0.0014823) present a large spectral peak near zero, and this is due to the presence of wall effects and small aerodynamic loads that are difficult to be measured with the current load cell. Cases 4-6 experienced wall effects, and Cases 7 and 9 were performed at a Reynolds number of 7229, which corresponded to a flow speed of 0.119 m/s. The NCSU water tunnel flow speed goes from 0 to 1.0 m/s but the tunnel operates most efficiently at speeds higher than 0.17 m/s. At a speed of 0.119 m/s the load cell measurements were very close to the load cell resolution, therefore the signal to noise ratio was low. As mentioned before, Cases 11-13 used a motion with half A_x and A_y compared to Cases 4-6, and this yielded no wall effects. The C_L spectra for Cases 4-6 and 11-13 is shown in Figures 48(c) and 48(d), when observing these figures side-by-side, the large spectral peak is no longer present when wall effects are removed.

Since the controlled motions were very slow compared to the vortex shedding frequency, and on average a single cycle lasted 20 minutes, it was of interest to compare the $(C_L)_{rms}$, $(C_D)_{mean}$, and shedding frequency results against the static case. The $(C_L)_{rms}$, $(C_D)_{mean}$, and shedding frequency results for the controlled motion experiments are shown in Figure 49.

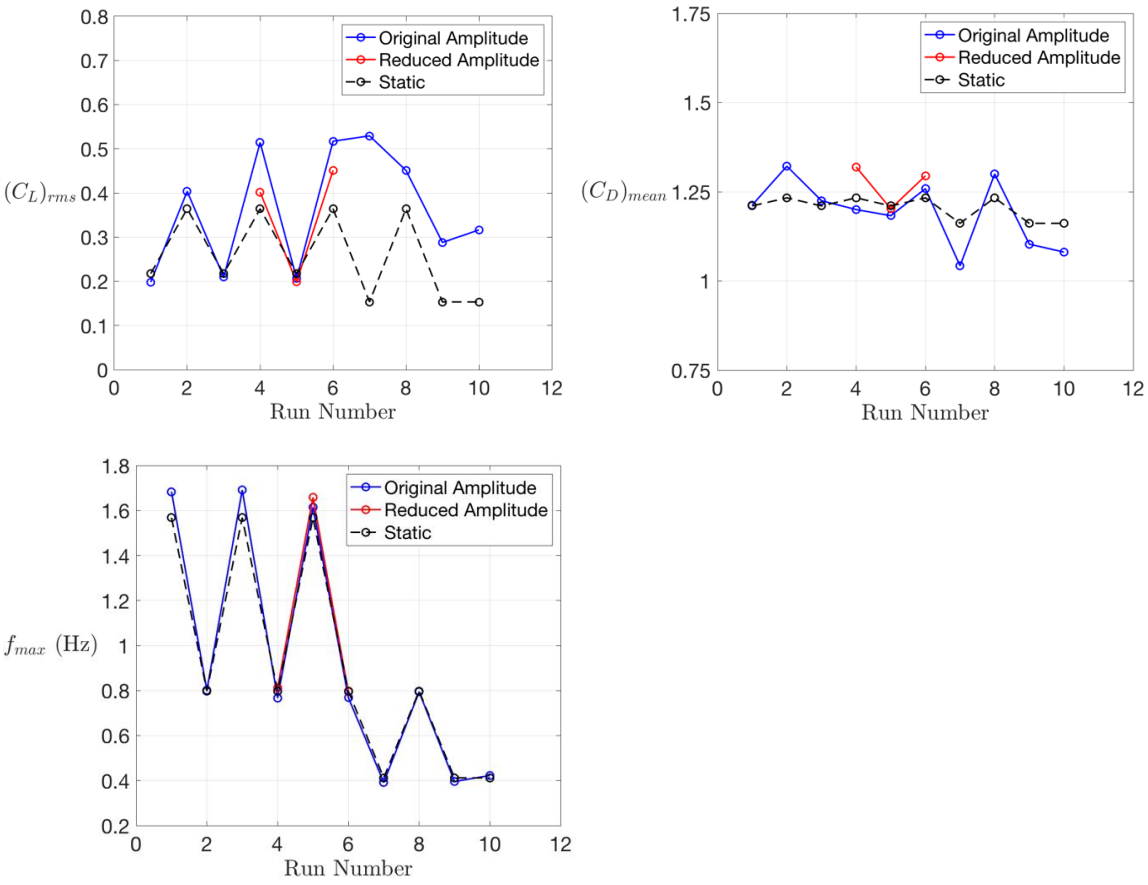

Figure 49: Comparison between dynamic and static $(C_L)_{rms}$, $(C_D)_{mean}$, f_{max} for Cases 1-13. Cases 11-13 are shown in red.

The results in Figure 49 show trends similar to the static case, as was expected. The $(C_L)_{rms}$ was relatively close to the static results, although Cases 6, 7, 9, and 10 were relatively higher in comparison. Cases 11-13 are labeled as Reduced Amplitude, and these yielded a smaller difference with respect to the static values in comparison with Cases 4-6. The $(C_D)_{mean}$ and shedding frequency results were much closer to the static values. In Figure 49(c) f_{max} is referred to the frequency where the maximum value of $C_L(f)$ occurs, which is considered the shedding frequency. The f_{max} results showed agreement with the static results, thus demonstrating that the vortex shedding from the controlled motion experiments was similar to the static case due to the very slow motions. $RMSE$ values for these three parameters are shown in Table 10.

Run #	$(C_L)_{rms}$ $RMSE$ (%)	$(C_D)_{mean}$ $RMSE$ (%)	f_{max} $RMSE$ (%)
1	$\pm$9.72	$\pm$0.20	$\pm$6.85
2	$\pm$9.82	$\pm$6.70	$\pm$0.46
3	$\pm$3.85	$\pm$1.20	$\pm$7.26
4	$\pm$29.2	$\pm$2.74	$\pm$4.02
5	$\pm$5.27	$\pm$2.31	$\pm$2.84
6	$\pm$29.6	$\pm$2.03	$\pm$3.78
7	$\pm$71.0	$\pm$11.40	$\pm$5.23
8	$\pm$19.3	$\pm$5.13	$\pm$0.47
9	$\pm$46.7	$\pm$5.29	$\pm$4.14

10	±51.5	±7.45	±2.45
11	±9.36	±6.55	±1.72
12	±9.47	±0.66	±5.43
13	±19.2	±4.77	±0.48

Table 10: RMSE between experimental results and model predictions for lift coefficient, drag coefficient, and shedding frequency. Green results indicate satisfaction of the milestone, blue indicates near satisfaction, and red indicates significant error.

Three important conclusions follow from an assessment of the aforementioned RMSE results:

- The team's models are accurately predicting tether drag and shedding frequency, which are the most significant predictors of flight dynamic behavior.
- Errors in lift prediction are significant insofar as they impact the dynamic performance predictions for the kite.
- The results demonstrate that the kite's periodic motions have frequencies far from the Strouhal vortex shedding frequency.

To summarize, these set of results answer the first question that was posed, and demonstrate that we are indeed not flying at a frequency that is close to the natural vortex shedding frequency. This is desired since flying at a frequency that is close to the vortex shedding frequency can lead to a dramatic increase in the hydrodynamic forces, which poses design and controller challenges. The second objective that was presented regarding the tether hydrodynamics was:

2. *Are we experiencing vortex induced vibrations as the kite flies?*

Since it is known that the kite flies at a frequency that is significantly slower compared to the natural vortex shedding frequency, is the natural vortex shedding causing any vibrations? if so, how does the $(C_L)_{rms}$ and $(C_D)_{mean}$ change? The main question was answered by looking into the free-vibrations experimental literature, and relevant non-dimensional parameters were extracted to perform controlled motion experiments to determine the magnification of the hydrodynamic loads. Jauvtis & Williamson (*2004*) performed free-vibrations experiments where a cylinder was connected to two-pairs of springs (one in x-direction, and another in y-direction). The authors varied the flow speed to observe the free-vibrations patterns that arouse from operating in a Reynolds number range from 1000 to 15,000. Normalized amplitudes and frequencies for the x- and y-directions, and phase change were extracted from Jauvtis & Williamson's data (using current kite simulation data), and shown below in Table 11.

Tether Length (m)	$\boldsymbol{Re}$	**Velocity Ratio** $(\boldsymbol{U^* = U_\infty/f_s d})$	$\boldsymbol{A_x/d}$	$\boldsymbol{A_y/d}$	$\boldsymbol{f_x/f_s}$ **and** $\boldsymbol{f_y/f_s}$	**Phase change** $(\boldsymbol{\phi})$
60	14380	4.72	0.038	0.45	0.84	149°

Table 11: Normalized amplitudes and frequencies for the x- and y-directions, along with phase change.

A controlled motion test was performed using $\frac{A_x}{d} = 0.10$, $\frac{A_y}{d} = 0.50$, $\frac{f_x}{f_s} = \frac{f_y}{f_s} = 0.85$, and $\phi = 135°$. The C_L spectra results confirm the presence of lock-in due to the large amplitude and sharply defined spectral peak shown in Figure 50, and the $(C_L)_{rms}$ and $(C_D)_{mean}$ static and Figure-8 VIV controlled motion results are listed in Figure 50.

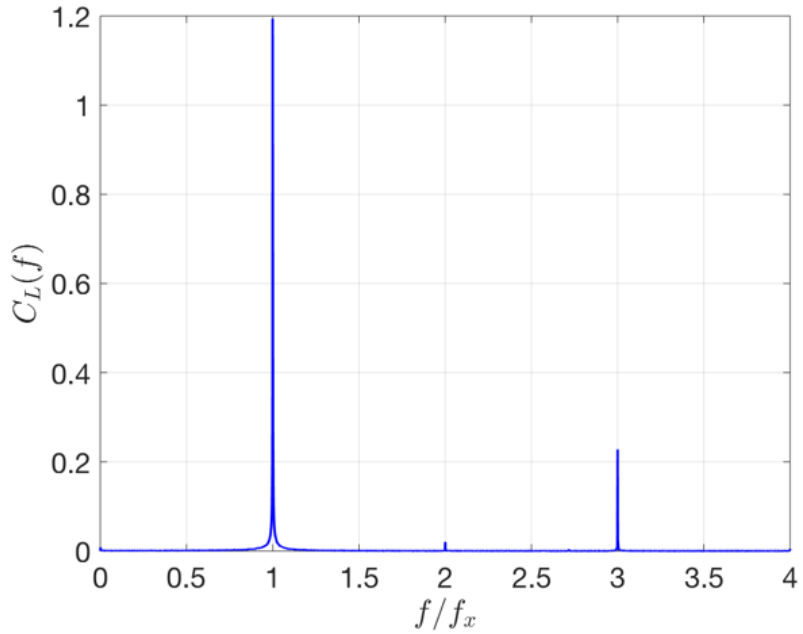

Figure 50: Lift coefficient spectrum for $A_x/d = 0.05$ and A_y/d =0.50, $f_x/f_s = f_y/f_s = 0.86$, $\phi = 135°$.

Test Type	$(C_L)_{rms}$	$(C_D)_{mean}$
Static	0.303	1.229
Figure-8 VIV	2.532	1.597

Table 12: Lift and drag coefficient results for static and Figure-8 VIV tests.

The $(C_L)_{rms}$ increased by an order of magnitude and the $(C_D)_{mean}$ increased by 24% compared to the static case. Since the tether will experience 2DoF vortex induced vibrations, the kite-tether system should have a natural frequency that is not close to the frequency of the vortex induced vibrations. The natural frequency to avoid when the tether length is 60m, and the system is operating in this flow regime is presented below in Table 13. The vortex shedding frequency is expressed as f_s.

Tether Length (m)	Flow Speed (m/s)	Re	Shedding Frequency (f_s) in Hz	System's Natural Frequency Should Not Be Equivalent To
60	1.00	14380	14.22	$f_n \neq 0.84 f_s = 11.98Hz$

Table 13: Natural frequency to avoid for a system with a tether length of 60m, operating at a Reynolds number of 14,380.

The determination of what natural frequencies the system should avoid is very dependent on flow speed, tether length and diameter, and Young's Modulus. The tether length, L, is used to calculate tether mass and stiffness, along with Young's Modulus, and these are the main parameters used to find f_n. For the 13 cases evaluated, the estimated natural frequencies to avoid are listed in Table 12. Two important things to note are: (i) all the simulation cases used a cylinder diameter of 0.0144m and a Young's Modulus of 40*10^(9) Pa, and (ii) the frequency ratios, f/f_s, were extracted from Jauvtis & Williamson's free-vibrations results. In Table 12, Cases 1, 9, and 10 do not report a frequency ratio since Jauvtis & Williamson report frequency ratio data from $U^* = 1.76$ to 13.45.

Run #	L (m)	U (m/s)	Re	f_s (Hz)	f_n (Hz)	U^*	f/f_s	$f_n \neq \frac{f}{f_s} f_s$ (Hz)
1	100	2.0	28844	28.06	8.83	15.73	NA	NA
2	90	1.0	14380	14.22	9.81	7.08	0.98	13.96
3	80	2.0	28844	28.06	11.04	12.59	1.33	37.40
4	70	1.0	14380	14.22	12.61	5.51	0.91	12.98
5	60	2.0	28844	28.06	14.71	9.44	1.31	36.73
6	60	1.0	14380	14.22	14.71	4.72	0.84	11.98
7	50	0.5	7205	7.31	17.66	1.97	0.51	3.75
8	50	1.0	14380	14.22	17.66	3.93	0.77	11.00
9	40	0.5	7205	7.31	22.07	1.57	NA	NA
10	30	0.5	7205	7.31	29.43	1.18	NA	NA
11	70	1.0	14380	14.22	12.61	5.51	0.91	12.98
12	60	2.0	28844	28.06	14.71	9.44	1.31	36.73
13	60	1.0	14380	14.22	14.71	4.72	0.84	11.98

Table 14: Natural frequencies to avoid for the 13 cases that were evaluated.

To conclude, the free-vibrations literature confirmed the presence of 2DoF vortex induced vibrations for the range of simulation cases that were evaluated, and also provided an estimate of what natural frequencies should be avoided when designing the system. The natural frequency of the kite system should be higher than the results reported in Table 14, but the final value will be determined based on the final tether geometry and/or material properties. In addition, the controlled motion test provided an estimate of the hydrodynamic loads magnification due to experiencing VIV, which were an order of magnitude higher for C_L, and approximately 30% for C_D.

Kite characterization: In experimental characterizing the hydrodynamics of the kite and comparing these experimental results to a variety of steady, quasi-steady, and unsteady hydrodynamic models, the team has:

- Converted the kinematics of a figure-8 kite trajectory to non-dimensionalized unsteady parameters for the purpose of quantifying an unsteady correction to the kite model;
- Performed unsteady model and experimental characterizations on motions that were sinusoidally fit to the phase and amplitude of the figure-8 kite wings' kinematics. This was done with differing levels of fidelity from steady state, quasi-steady, and unsteady analysis to determine which model was the better characterization of the simplified sinusoidal parameters.
- Because the kite experiences predominantly cyclic motions of changing apparent velocity, angle of attack, and tether length during a single figure-8, it was deemed a good candidate motion to be represented as sinusoids of these three separate motions; and are referred to as surge, pitch, and plunge respectively. Not considered in the following models are the addition of bank angle, roll rate, yaw rate, or turning radius. Frequently, complicated unsteady research is reduced to cases of incompressible, single blade, and oscillatory planar motions. These characteristics are often modified due to too many variables affecting the same physical mechanisms of the results.

There is a base of existing works that have taken a similar approach to other types of three-dimensional motions, but often have investigated either a singular motion of surge, pitch, or plunge, or a combination of two motions, with the least frequency of all three motions combined. With the goal of achieving planar kinematic relationships to the simulated figure-8 kite wing paths, motions of surge, pitch, and plunge were obtained and converted to non-dimensionalized unsteady parameters.

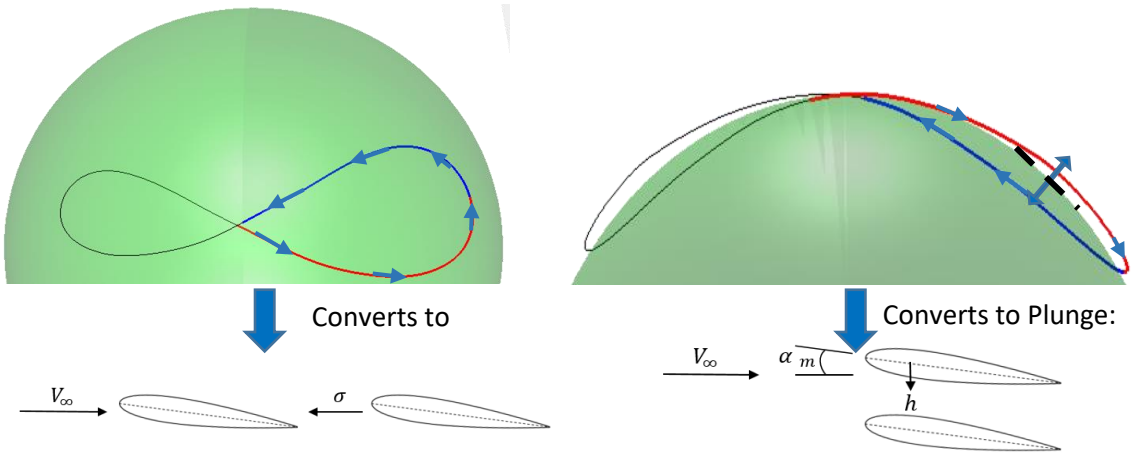

Figure 51: (Left) Surge: Traversing along the sphere with constant tether length. (Right) Plunging away from a constant tether length spherical surface towards (plunge down) or away from (plunge up) the sphere's center.

Surge was defined as the cyclic motion of traversing along the surface of a sphere that would be created if no tether spool-in or out were to occur at constant angle of attack. The flow direction on the left is out of the page towards the reader. Plunge occurs when the kite does have tether spool-in or out and plunging down is towards the tether's anchor point (spool-in), and away from the anchor point (spool-out). The flow direction on the right is up towards the top of the page. The third motion, pitch is defined as the angle of attack with respect to the apparent velocity vector of the flow encountered by the wing. These motions combine to complete the linear, oscillatory transformation.

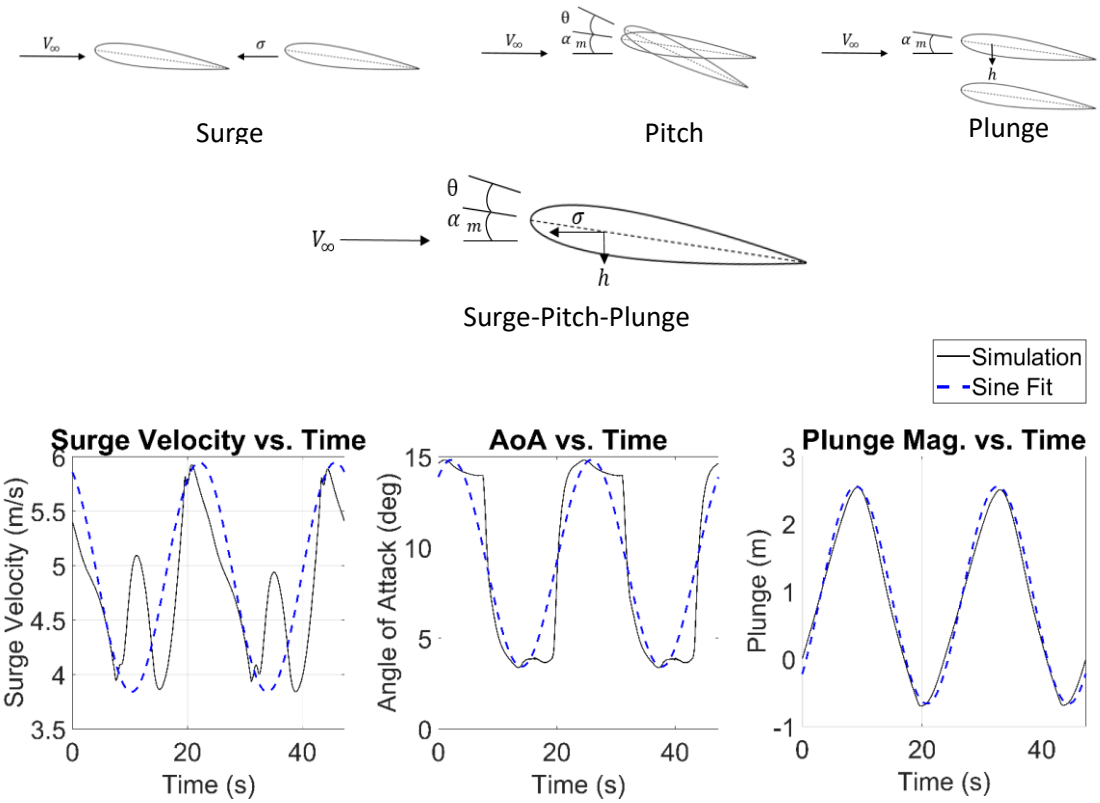

Figure 52: (Top) Surge, pitch, and plunge independent motions combined. (Bottom) The dashed-lines are sinusoidal fits of the simulation results in solid. These plots correspond to Case 3, listed in Table 16 for the 100 m tether length and 0.5 m/s flow speed.

Due to the relatively large plunge amplitudes with respect to the width of the NCSU water tunnel (WxDxL is 32x24x96 inches) test section, the following cases in Table 15 were able to be tested. The approximated sinusoidal motions are from an average of the port and starboard wings' motions due to mirrored changes on both loops on either side of the figure-8 crossing point. This causes two cycles of sinusoidal motion to be completed in a single figure-8. The following parameter derivations and results are for half (a single loop starting at the crossing point and back to the crossing point) of a figure-8 motion. The experiments matching the Table's parameters were performed for a mean Reynolds number of 50000 for a NACA 0018 foil.

Case #	Flow Speed (m/s)	Tether Length (m)	Period (s)	Reduced Frequency, k	Surge Amplitude	Mean App. Velocity (m/s)	Pitch Amplitude (deg)	Mean Angle (deg)	Plunge hm/c	Surge Phase (deg)	Pitch Phase (deg)	Plunge Phase (deg)
1	0.5	50	48.78	0.0308	0.19	2.09	5.43	8.62	1.90	33.59	50.54	127.91
2	0.5	70	12.54	0.0274	0.12	9.14	6.48	7.67	1.71	358.74	33.59	119.66
3	0.5	100	23.65	0.0268	0.21	4.96	5.58	7.53	1.61	334.87	50.83	136.55
4	1	30	15.57	0.0421	0.23	4.80	7.56	9.19	1.03	325.76	68.18	164.16
5	1	40	18.73	0.0335	0.20	5.10	6.32	8.11	1.22	319.90	50.76	145.55

6	1	50	23.69	0.0276	0.23	4.80	5.75	7.57	1.61	329.08	33.55	37.08
7	1	60	21.44	0.0407	0.25	3.60	6.62	8.15	1.65	67.82	50.76	153.79
8	2	30	9.37	0.0460	0.25	7.29	8.36	8.46	1.12	33.66	50.40	136.76
9	2	40	10.38	0.0347	0.16	8.71	7.09	8.03	1.35	16.92	50.62	119.59
10	2	50	12.55	0.0274	0.12	9.14	6.67	7.72	1.70	0.00	51.08	119.38
11	2	80	12.47	0.0402	0.29	6.27	7.63	7.50	2.03	56.30	67.57	145.26

Table 15: Sinusoidal kinematics derived from figure-8 kite wing kinematics; sorted by descending order of flow speed and then tether length.

The steady-state model is an interpolation of static lift measurements with increasing angle of attack. This model only considers pitch as it varies with apparent flow velocity. It is important to have static experimental results for the dynamic motions performed as they can vary widely between experimental facilities even with the same parameters and airfoil considered.

The quasi-steady model considered is a reduced Greenberg theory that only considers the linearly imposed lift of individual surge, pitch, and plunge contributions, and does not include apparent mass or a wake deficiency function. This model is attractive because it is the simplest model that still considers all three motions. Quasi-steady Components:

$$\text{Static} = 2\pi\theta_{mean}$$

$$\text{Surge} = 2\pi\sigma\theta_{mean}\left[\left(1+\sigma e^{i\omega t}\right)^2\right]$$

$$\text{Pitch} = 2\pi b\left(\theta + \frac{b(1/2-a)}{v_0}\dot{\theta}\right)$$

$$\text{Plunge} = 2\pi\frac{\dot{h}}{v_0}$$

$$C_{l,quasi} = 2\pi\left[\theta_{mean} + \sigma\theta_{mean}\left[\left(1+\sigma e^{i\omega t}\right)^2\right] + b\left(\theta + \frac{b(1/2-a)}{v_0}\dot{\theta}\right) + \frac{\dot{h}}{v_0}\right]$$

The first unsteady model that is investigated is also a reduced Greenberg theory, but considers the first force harmonic of circulatory, apparent mass, and the Theodorsen wake deficiency function. 1st Lift Force Harmonic Unsteady Greenberg Components:

$$\text{Static} = 2\pi\theta_{mean}$$

$$\text{Surge} = 2\pi\sigma\theta_{mean}e^{i\omega t}\left[1+\left(1+\sigma e^{i\omega t}\right)C(k) + i\frac{b}{2v_0}\omega\right]$$

$$\text{Pitch} = \pi b\frac{\dot{\theta}}{v_0} - \pi b^2 a\frac{\ddot{\theta}}{{v_0}^2} + 2\pi\theta C(k) + 2\pi\frac{b(1/2-a)}{v_0}\dot{\theta}C(k)$$

$$\text{Plunge} = \pi b\frac{\ddot{h}}{{v_0}^2} + 2\pi\frac{\dot{h}}{v_0}C(k)$$

$$C_{l,Greenberg} = 2\pi\theta_{mean} + 2\pi\sigma\theta_{mean}e^{i\omega t}\left[1+\left(1+\sigma e^{i\omega t}\right)C(k) + i\frac{b}{2v_0}\omega\right] + \pi b\frac{\dot{\theta}}{v_0} - \pi b^2 a\frac{\ddot{\theta}}{{v_0}^2} + 2\pi\theta C(k) + 2\pi\frac{b(1/2-a)}{v_0}\dot{\theta}C(k) + \pi b\frac{\ddot{h}}{{v_0}^2} + 2\pi\frac{\dot{h}}{v_0}C(k)$$

This Greenberg theory is closed-form and can still be implemented quickly into real-time controllers. There are limitations and assumptions made:

- Two-dimensional, potential flow, trailing edge Kutta condition
- Uniform, chord velocity perturbation
- Sinusoidal, harmonic motions
- High frequency wake integral consideration
    - Evenly spaced wake
    - Moderate surge amplitude accuracy, $\sigma = 0.4$

The most complicated unsteady model considered is a Generalized Isaacs formulation from the seminal works of van der Wall to include an arbitrary pitch location and plunge displacement. This is an open solution with multiple Fourier series components, but considers variable chord velocity perturbations and variable velocity wake while still maintaining two-dimensional, potential flow, trailing edge Kutta condition, sinusoidal harmonic motion considerations. Apparent mass, coupled lift effects, and wake deficiency are accounted for, where this is considered to be a complete potential flow solution.

$$C_{l,Isaacs,nc} = 2\pi\alpha_0 \frac{k}{2}\{[\sigma\bar{\alpha}_0 + \bar{\alpha}_{1S} + k(a\bar{\alpha}_{1C} - \bar{h}_{1C})]\cos\omega t - [\bar{\alpha}_{1C} - k(a\bar{\alpha}_{1S} - \bar{h}_{1S})]\sin\omega t + \sigma(\bar{\alpha}_{1C}\cos 2\omega t + \bar{\alpha}_{1S}\sin 2\omega t)\}$$

$$C_{l,Isaacs,c} = 2\pi\alpha_0 \left(\left\{\left(1 + \frac{\sigma^2}{2}\right)\bar{\alpha}_0 + \sigma\left[\bar{\alpha}_{1S} - \frac{k}{2}\left(\left(\frac{1-2a}{2}\right)\bar{\alpha}_{1C} + \bar{h}_{1C}\right)\right]\right\}(1 + \sigma\sin\omega t) + \sum_{m=1}^{\infty}(l_{\mathrm{m}}\cos m\omega t + l'_{\mathrm{m}}\sin m\omega t)\right)$$

$$C_{l,Isaacs} = C_{l,Isaacs,nc} + C_{l,Isaacs,c}$$

For the Experiment, one side of a 6-axis load cell ATI Delta is mounted to the bottom of the rotary motor. The other side of the load cell is connected to the vertically oriented airfoil test article to measure aerodynamic forces and pitching moment. The airfoil is constructed from two, internal span-wise CFRP tubes approximately at 1/3*chord and 2/3*chord, supporting four wire-EDM stainless steel profiles at ¾*span ½*span, ¼*span and the top. The bottom profile is made of CPVC to prevent scratching the glass during the mounting process. The skin of the airfoil is made of two layers of vacuum molded GFRP. Twenty-five cycles sampled at 1 kHz of each motion were recorded to measure an accurate sample representation for the load cell data collection. The first three, and last the two cycles were not used to eliminate potential influence from initial startup and completion of the oscillations, resulting in 20 total used cycles and then filtered at five times the motion frequency using a fourth-order Chebyshev II low-pass filter in MATLAB. A tare of the system motion was performed to isolate the aerodynamic and non-circulatory forces. The NACA 0018 airfoil has a 0.146 m chord and 4.2 aspect ratio with 20˚ pitch maximum. This is a maximum static blockage of 6.4% that only momentarily occurs during dynamic motions.

An aspect ratio of approximately four has been used in several water tunnel facilities. Aspect ratio and other experimental factors such as gap effects, freestream turbulence, airfoil stiffness, and static blockage

are not entirely accounted for in the present experiment and can vary broadly between experimental facilities. The experiment does take measures to minimize the influence of these factors, but the affects cannot be eliminated. The natural frequency of 5.4 Hz of the submerged airfoil assembly was determined through fast Fourier transform of the lift force signal when tapped with a soft mallet. The forcing frequency range of 0.02 to 0.03 corresponding to reduced frequency of 0.02 to 0.05 is over two orders of magnitude less than the natural frequency of the airfoil, resulting in negligible airfoil bending.

Results are shown in Table 16.

Case #	Flow Speed (m/s)	Tether Length (m)	RMSE Steady AoA (%)	RMSE Quasisteady (%)	RMSE Greenberg 1st Harmonic (%)	RMSE Generalized Isaacs (%)
1	0.5	50	10.90	13.70	21.00	31.60
2	0.5	70	20.70	16.50	16.60	24.60
3	0.5	100	21.30	5.50	14.10	14.80
4	1	30	29.20	27.40	18.70	18.20
5	1	40	27.50	12.60	12.00	13.70
6	1	50	32.40	30.90	26.30	36.00
7	1	60	19.00	28.20	29.00	37.50
8	2	30	32.60	45.60	23.80	35.50
9	2	40	19.30	15.30	6.37	15.30
10	2	50	18.70	14.10	11.40	19.70
11	2	80	24.50	39.70	26.00	30.20

Table 16: RMSE deviation from experiment for the four models discussed, sorted by descending order of flow speed, then tether length.

The goal is to have a 5 percent or lower root mean squared error (RMSE) between the experimental results and the theory over the prescribed motions. An important note from the last report is that may only be feasible where surge-pitch and surge-plunge coupled effects are not dominant. Due to size constraints on the water channel, only one case with a 100+ meter tether length could be tested.

Results corresponding to a 100m tether length and 0.5 m/s flow speed (scaled for the water channel) and an 80m tether length and 2 m/s flow speed (scaled for the water channel) are shown in Figure 53. Comparisons are made over all of the models described in the aforementioned summary. A full summary of test results is given in Table 17.

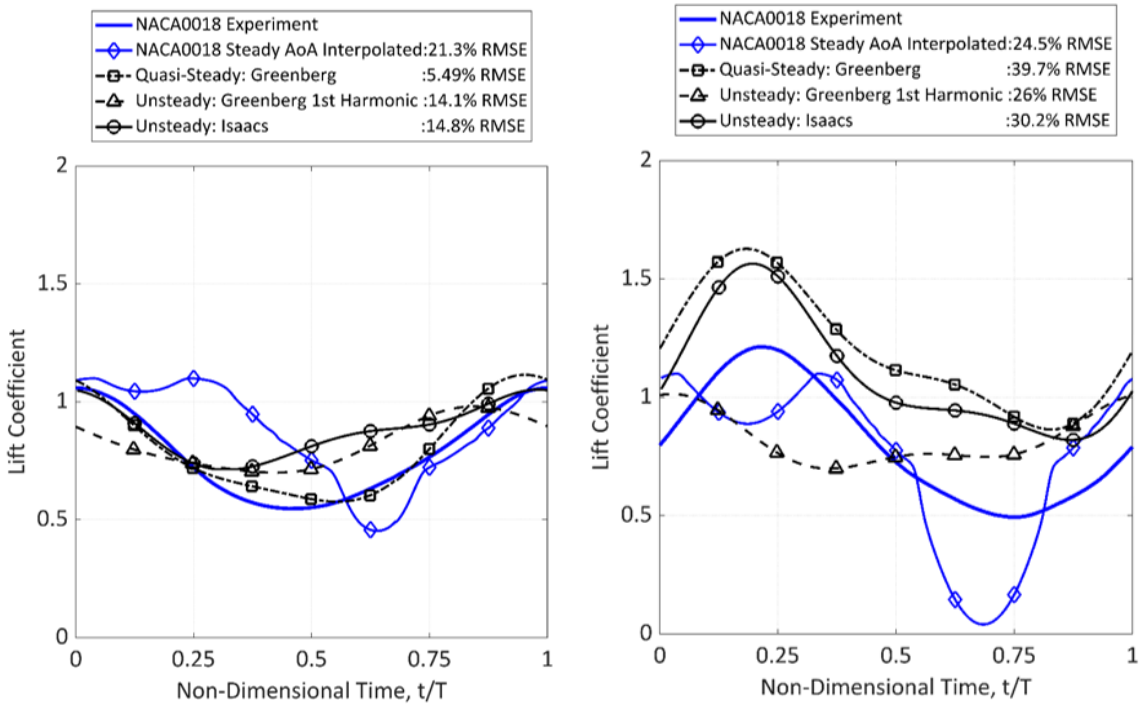

Figure 53: Comparison of model predictions against experiments for (scaled) test conditions corresponding to a 100m tether with 0.5 m/s flow (left) and 80m tether with 2 m/s flow (right).

Case #	Flow Speed (m/s)	Tether Length (m)	RMSE Steady AoA (%)	Steady Mean to Mean Comparison	RMSE Quasisteady (%)	Quasi Mean to Mean Comparison	RMSE Greenberg 1st Harmonic (%)	Greenberg Mean to Mean Comparison	RMSE Generalized Isaacs (%)	Isaacs Mean to Mean Comparison
1	0.5	50	10.9	8.3	13.7	10.7	21.0	19.1	31.6	22.4
2	0.5	70	20.7	15.3	16.5	7.5	16.6	6.9	24.6	8.8
3	0.5	100	21.3	18.8	5.5	4.9	14.1	13.3	14.8	10.9
4	1	30	29.2	28.6	27.4	12.8	18.7	12.9	18.2	12.9
5	1	40	27.5	27.2	12.6	9.4	12.0	9.9	13.7	10.3
6	1	50	32.4	25.9	30.9	25.8	26.3	21.3	36.0	26.4
7	1	60	19.0	15.8	28.2	9.7	29.0	24.6	37.5	9.1
8	2	30	32.6	30.2	45.6	20.9	23.8	22.6	35.5	13.9
9	2	40	19.3	18.6	15.3	10.9	6.4	6.0	15.3	5.5
10	2	50	18.7	17.1	14.1	7.9	11.4	5.0	19.7	10.7
11	2	80	24.5	23.5	39.7	6.4	26.0	25.9	30.2	7.3
Average RMSE PCT Error			23.28	20.85	22.68	11.54	18.66	15.24	25.19	12.56

Table 17: Full test result summary, including RMSE between experiments and model predictions, both with and without a correction for mean matching (explained below).

Mean to Mean Comparison in the above Table refers to setting the mean value of the theory equal to the mean value of the experiment. This is done to isolate the dynamic effects of the theory as compared to the experiment. The average RMS error is greatly reduced by almost 50% for both the quasi-steady and Generalized Isaacs theories. This significant improvement is an indication that these two theories are capturing the dynamics of the lift coefficient better than an interpolated-steady angle of attack approach.

However, this also indicates that the accuracy level of modelling the mean amplitude of the lift coefficient is attributing to half of the error. The mean of the theory in these cases is always greater than the magnitude of the experimental mean. This is most likely due to unsteady boundary layer affects that are not captured in the theories.

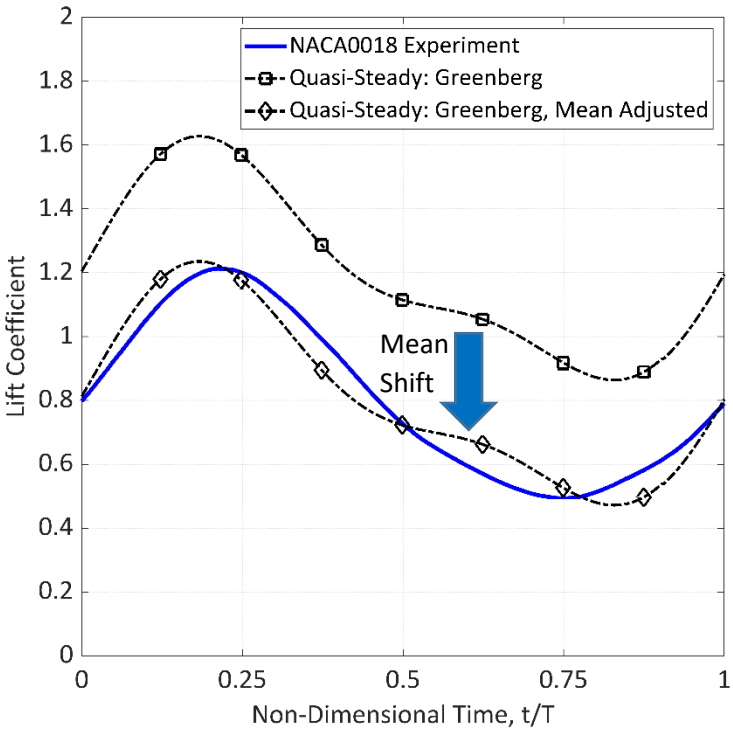

Figure 54: Case 11, quasi-steady lift coefficient only, with a mean amplitude shift to the experimental mean to demonstrate the theory capturing the dynamics of the experiment.

6.4 Small-Scale Water Channel-Based Validation of Dynamic Performance

Per the SOPO, the team was to complete characterization of the kite through tether-based cross-current flight control in the water channel. The experimental results were to be compared against dynamic model predictions, and demonstrate RMSE of 5 percent or less, in terms of position and attitude prediction, over the course of a simulation/experiment. The methodology and results are summarized here, with further details available in [18].

The team was able to complete a substantial number of closed-loop cross-current flight tests using a 1.5:100 scale kite model, as shown in Figure 55. The cross-current flight test served as the primary basis for model refinement and validation, as they are most representative of the conditions under which we desire the dynamic model to be highly accurate (thereby representing the most logical conditions for verifying the fulfillment of milestones 5.2 and 5.3). The summary of the cross-current flight tests executed by tracking a square wave roll setpoint are shown in Table 18.

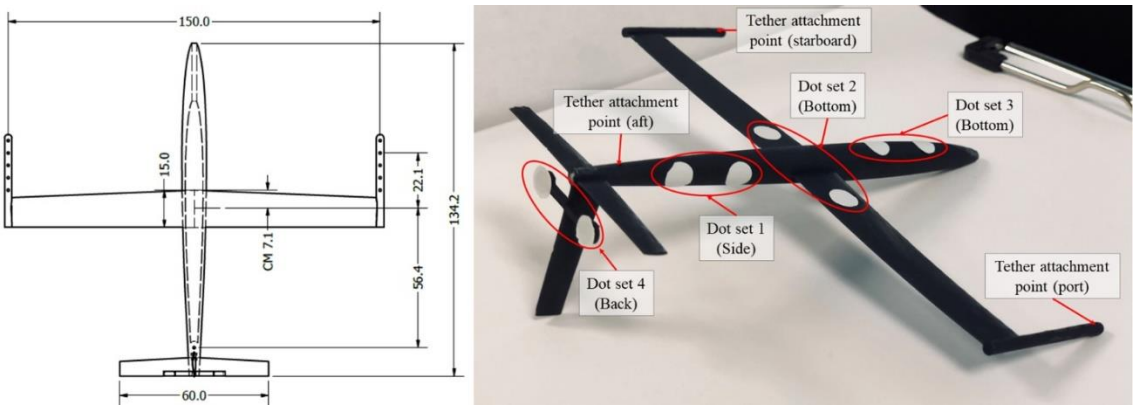

Figure 55: (Left) CAD Drawing of the kite model used in the water channel characterization experiments; (Right) Actual Kite model with locations of dots (used for tracking) and tether attachment points.

Run	Flow speed (m/s)	Square wave amplitude (deg)	Square wave period (s)
1	0.245	12	6
2	0.262	13	6
3	0.279	13	5.5
4	0.296	13	5.5
5	0.313	13	5
6	0.330	13	5
7	0.347	13	4.75
8	0.364	13	4.75
9	0.381	13	4.75
10	0.381	14	4.75
11	0.390	14	4.75
12	0.398	14	4.5

Table 18: Summary of experiments. Odd-numbered experiments served as ***training experiments***, used to further improve the dynamic model, whereas even-numbered experiments served as ***validation experiments***, which served to assess the quality of the model and also served as a metric for assessing fulfillment of Milestones 5.2 and 5.3.

Experimental validation: The goal of the water channel testing was to validate our dynamic model, which consisted of two major steps – model refinement, and model validation. The collected data sets were split into two groups: one group for model refinement and another for validation. The refinement data sets were used to identify and refine the values of critical simulation parameters, whereas the validation data sets were used to test the goodness of fit of the refined parameters.

Model refinement: In order to refine the model, the team identified a set of nine key parameters for which model uncertainty was high, and used numerical optimization to determine the values of these parameters (specifically, ``adjustment coefficients" to the original parameters) that minimized RMSE between the model and data. These parameters were lift and drag coefficients of the wing, horizontal stabilizer, and vertical stabilizer; and added mass terms along the x, y, and z direction. In each case, the original parameter values were multiplied by the adjustment coefficients to form the refined parameters.

The adjustments coefficients were optimized by minimizing an objective function which was equal to the weighted sum of Root Mean Squared Errors (RMSE) between the simulated and measured values of the roll angle (ϕ), yaw angle (ψ), and y-position (y_{cm}), as follows:

$$c_j^* = \underset{c_j}{arg\,min}\left(w_1 R_\phi + w_2 R_\psi + w_3 R_y\right)$$

$$= \underset{c_j}{arg\,min}\left(w_1\sqrt{\sum_{i=1}^{n}\frac{\left(\phi_{exp,i}-\phi_{sim,i}\right)^2}{n}} + w_2\sqrt{\sum_{i=1}^{n}\frac{\left(\psi_{exp,i}-\psi_{sim,i}\right)^2}{n}} + w_3\sqrt{\sum_{i=1}^{n}\frac{\left(y_{exp,i}-y_{sim,i}\right)^2}{n}}\right)$$

Subject to: $0.5 \le c_j \le 1.5 \qquad for\ j = 1,2,\ldots,9.$

Here, R_ϕ, R_ψ, and R_y are root mean squared errors in roll angle, yaw angle, and y-position, respectively; $\phi_{exp,i}$, $\psi_{exp,i}$, and $y_{exp,i}$ are the experimentally measured values of the roll angle, yaw angle, and y-position of the kite at time step i. n is the total number of time steps over a course of the experiment ($n = 6000$ for a 60 s experiment). The constraints on the scaling coefficients were imposed to allow for 50% error in the initial estimate of the uncertain parameters. Optimized values of c_j close to 1 would indicate a good initial characterization of the uncertain parameter associated with the scaling coefficient.

The weighting terms (w_1, w_2, w_3) on the RMSE values of the roll angle, yaw angle, and y-position were set to 1, 1, and 5, respectively. The optimized values of the adjustment coefficients are listed in Table 19. These results indicate relatively high modeling accuracy for all of the identified parameters, ***with the exception of added mass terms***. This triggered an additional investigation into the team's mechanisms for characterizing added mass, the results of which were implemented in the dynamic model prior to tow testing (both pool-based and open-water) during budget period 2.

Description	Adjustment Coefficient	Value
Added mass in x	c_1	0.543
Added mass in y	c_2	1.135
Added mass in z	c_3	0.782
Half wing lift coefficient	c_4	0.989
Horizontal stabilizer lift coefficient	c_5	0.961
Vertical stabilizer lift coefficient	c_6	0.992
Half wing drag coefficient	c_7	1.096
Horizontal stabilizer drag coefficient	c_8	1.103
Vertical stabilizer drag coefficient	c_9	1.095

Table 19: Results of model refinement. It is noteworthy that the model refinement revealed accurate estimates of all parameters except for added mass parameters, which prompted a significant refinement of the dynamic model to better-account for these terms.

Model validation: The goodness of fit between the predicted and measured values was quantified by calculating the RMSE values described by , R_ϕ, R_ψ, and R_y, along with "aggregate" metrics that quantify the differences in amplitude and phase shift between the experimental validation data and model predictions. The equations for these additional "aggregate" metrics are as follows:

$$A_\phi = \frac{\sqrt{\frac{\sum_{i=1}^{n_p} \phi_{sim,i}^2}{n_p}} - \sqrt{\frac{\sum_{i=1}^{n_p} \phi_{exp,i}^2}{n_p}}}{\max(\phi_{exp}) - \min(\phi_{exp})}$$

$$A_\psi = \frac{\sqrt{\frac{\sum_{i=1}^{n_p} \psi_{sim,i}^2}{n_p}} - \sqrt{\frac{\sum_{i=1}^{n_p} \psi_{exp,i}^2}{n_p}}}{\max(\psi_{exp}) - \min(\psi_{exp})}$$

$$A_y = \frac{\sqrt{\frac{\sum_{i=1}^{n_p} y_{sim,i}^2}{n_p}} - \sqrt{\frac{\sum_{i=1}^{n_p} y_{exp,i}^2}{n_p}}}{\max(y_{exp}) - \min(y_{exp})}$$

$$P_\phi = \frac{2}{T}\frac{\sum_{i=1}^{n_z-1}\left(t_{sim,i+1}^\phi - t_{sim,i}^\phi\right) - \sum_{i=1}^{n_z-1}\left(t_{exp,i+1}^\phi - t_{exp,i}^\phi\right)}{n_z - 1}$$

$$P_\psi = \frac{2}{T}\frac{\sum_{i=1}^{n_z-1}\left(t_{sim,i+1}^\psi - t_{sim,i}^\psi\right) - \sum_{i=1}^{n_z-1}\left(t_{exp,i+1}^\psi - t_{exp,i}^\psi\right)}{n_z - 1}$$

$$P_y = \frac{2}{T}\frac{\sum_{i=1}^{n_z-1}\left(t_{sim,i+1}^y - t_{sim,i}^y\right) - \sum_{i=1}^{n_z-1}\left(t_{exp,i+1}^y - t_{exp,i}^y\right)}{n_z - 1}$$

Here, n_p and n_z are number of peaks and number of zero-crossings over the duration of the experiment, respectively. A_ϕ, A_ψ, and A_y are the differences between the average amplitude of the roll angle, yaw angle, and the y-position, respectively; P_ϕ, P_ψ, and P_y are the differences between the average periods of the roll angle, yaw angle, and the y-position, respectively.

Milestones 5.2 and 5.3 required the team to demonstrate less than 5 percent RMSE between simulations and water channel experiments under dynamic motions that consist of (i) basic steady control of the kite and (ii) cross-current flight. **As is demonstrated below, the team achieved this RMSE target in the vast majority of test cases, based on the critical variables and metrics summarized in the discussion**. A full summary of results is given in Table 20, for each of the validation experiments.

Run	A_ϕ (%)	A_ϕ (%)	A_y (%)	P_ϕ (%)	P_ψ (%)	P_y (%)	R_ϕ (deg)	R_ψ (deg)	R_y (cm)
2	10.43	6.86	14.48	0.03	0.07	0.12	2.32	4.24	1.20
4	3.89	2.44	8.07	0.05	0.14	0.09	1.77	4.07	0.78
6	2.63	2.36	3.24	0.04	0.03	0.03	1.66	4.05	0.39
8	6.05	6.16	3.90	0.01	0.06	0.01	3.17	2.86	0.54
10	7.64	9.45	3.23	0.02	0.03	0.04	3.95	2.28	0.88
12	7.53	6.86	3.88	0.04	0.08	0.12	4.95	1.64	1.34

Table 20: Quantification of error between the dynamic model predictions and experiments for validation data (note that odd-numbered runs represent training data; hence their exclusion from the present results). Green numbers indicate fulfillment of the percent error target, whereas blue numbers indicate

near-fulfillment. The two instances of red numbers indicate significant prediction error. This test case (run 2) corresponds to the lowest Reynolds number tested and may not be indicative of the ability of the model to extrapolate to full-scale flight.

A comparison of key variables (Euler angles and positions) over two selected runs (run 6 and run 7) are shown in Figure 56, which underscore the tight correlation between predictions from the dynamic model and experiments. It is worth noting that run 7 is a training run, whereas run 6 is a validation run.

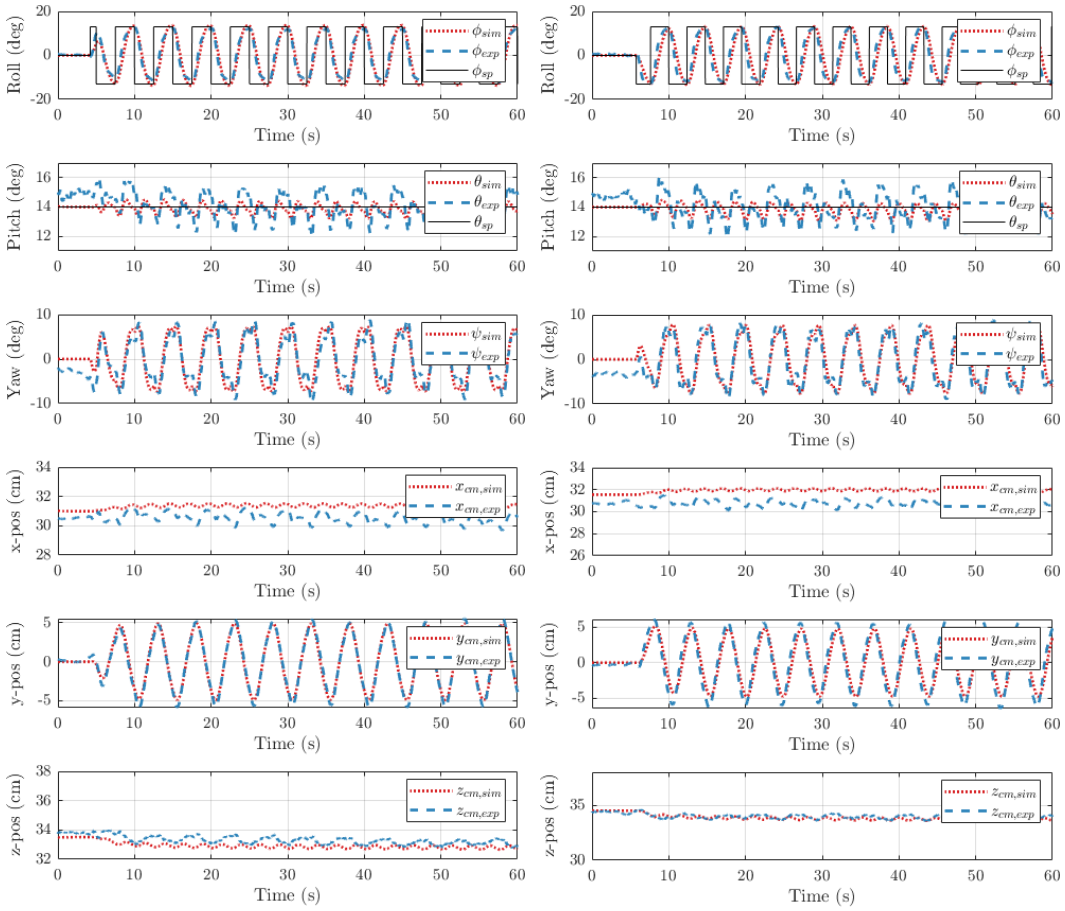

Figure 56: Examination of dynamic model vs. experimental data comparison for two selected test runs.

7 Component-Wise Validation

7.1 Power Take-Off "Dry" Testing

In parallel with its testing of the mechanical towing system, the University of Maryland team assembled and tested the winch system in a lab environment. This system consists of two Blue Robotics Fathom Spools, each controlled via brushless DC (BLDC) motors. Motor commands are issued by the team's Speedgoat rapid control prototyping system, and encoder measurements are fed back to the Speedgoat for inference of speed and spooled tether length measurements. Figure 57 shows CAD for the winch/spool system and the initial benchtop testing setup at the University of Maryland.

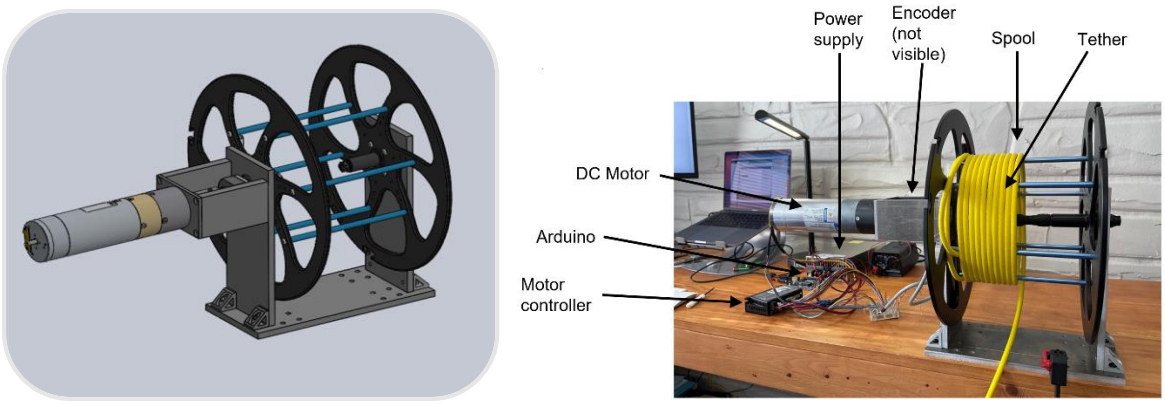

Figure 57: CAD (left) and lab setup (right) for winch and spooling system.

The team performed separate tests of the mechanical towing system and the winch system (including the motor control and encoder feedback). Videos from initial testing of the mechanical tow testing system are presently archived on the team's Google Drive folder at https://drive.google.com/drive/folders/1zr_CYKrYJPICdh0GPGAIxMfTftg2uWkm (viewable with an invitation to the folder). In terms of the winch system, the University of Maryland team ran three sets of test where it (i) ramped the spooling speed up to a set point at a ramp rate of 0.1 m/s^2, then (ii) controlled the spool to that setpoint, then (iii) ramped the spooling speed back down to zero at the same ramp rate. The tests were performed under load, and the team also confirmed that the system maintains its integrity and does not exhibit any undesirable flex modes under up to 400 N of tension. Results of winch testing for three spooling speeds are shown in Figures 58-60.

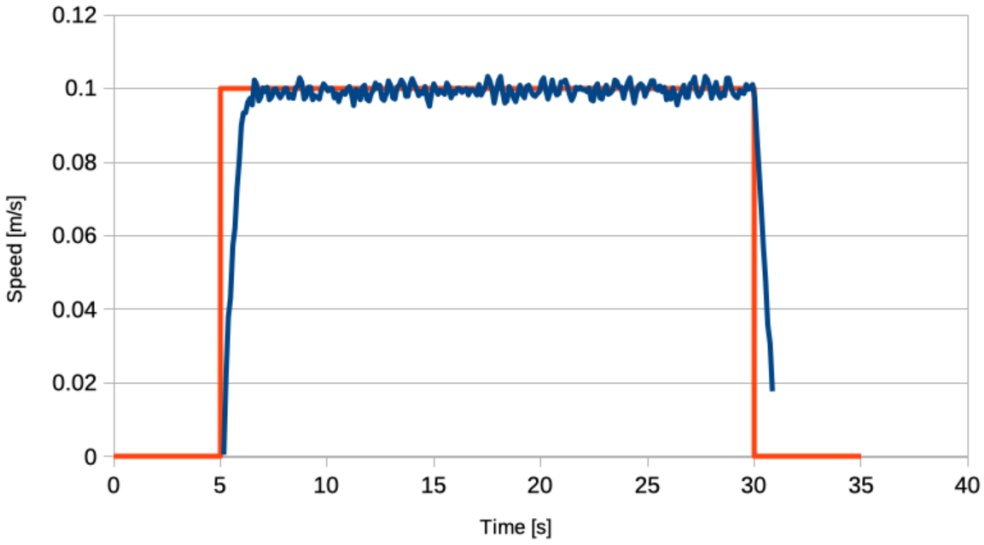

Figure 58: Winch validation test for a setpoint of 0.1 m/s.

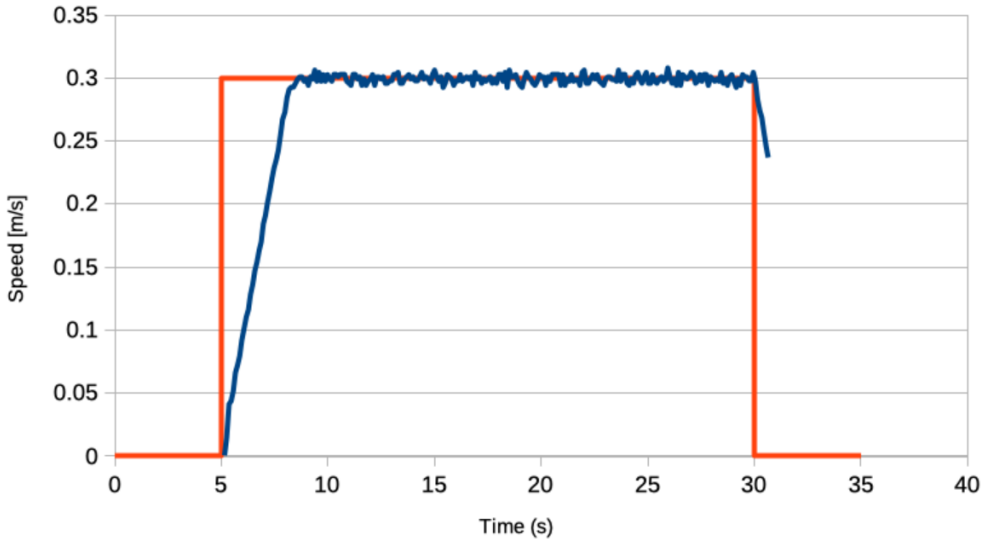

Figure 59: Winch validation test for a setpoint of 0.3 m/s.

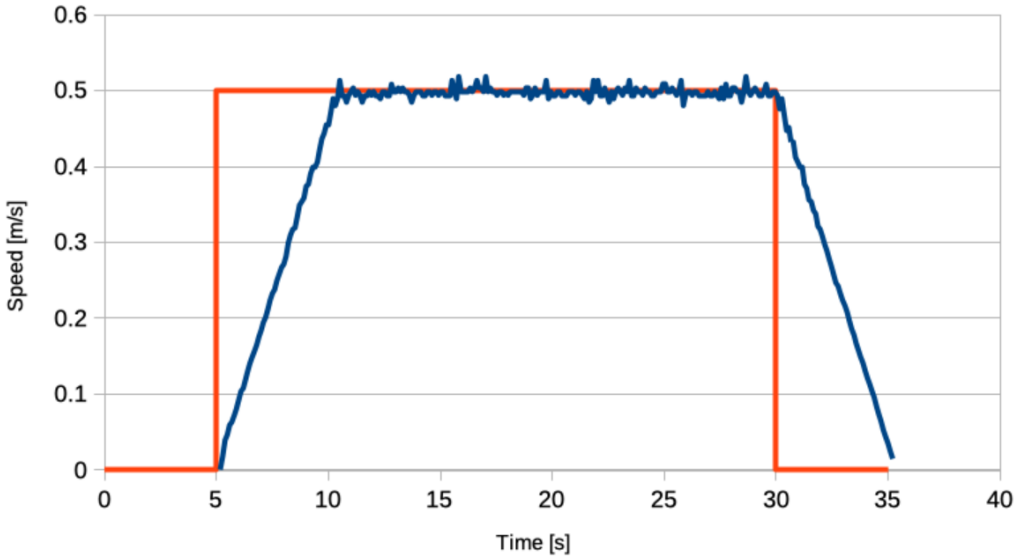

Figure 60: Winch validation test for a setpoint of 0.5 m/s.

7.2 Dry Hardware-in-the-Loop Testing of Kite and Ground Station Components

This task involved selection with the computing platform and sensor suite for prospective budget period 2 testing, in addition to developing the estimation algorithms for variables that are not measured. The computing platform and full sensor suite are shown in Figure 61.

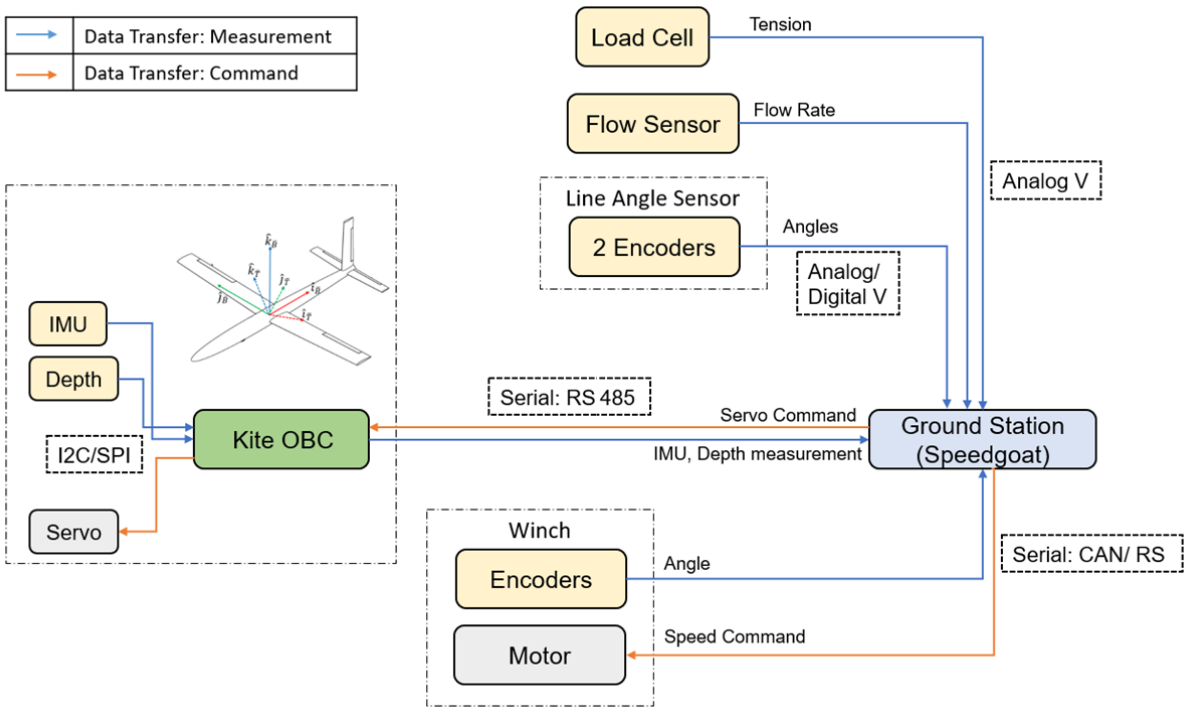

Figure 61: Computing, sensing, and communications schematic for tow testing. All of the components have been received and are being benchtop tested.

Computing Platform Selection:

The team selected a Speedgoat Baseline M machine for its primary (ground station) rapid control prototyping platform. Speedgoat machines are specifically designed to run Simulink projects in real time. The pairing of a Speedgoat hardware with software designed in Simulink means that no manual generation of C code or associated device drivers (for supported hardware) is required. The target machine features a 2GHz quad core CPU, 4GB RAM, 32GB solid state drive for data logging, and four mPCIe I/O slots for I/O expansion. The Baseline M machine has been customized to include the specific I/O modules required for the team's application, including:

- A serial module for communication to and from the kite's microcontroller;
- A quadrature encoder module for interfacing with the line angle sensor (two encoders) and winch encoder;
- A MODBUS module for communication to and from variable frequency drives (if MODBUS is the required communication mechanism for the chosen VFD);
- A CAN module for communication to and from variable speed drives (if CAN is supported);

Through hardware-in-the-loop testing, the team verified that its controller, with the exception of the dynamic programming-based elevation angle optimization (which is not relevant to tow testing) can execute at a time step of 0.1 seconds (in fact, a 0.01 second time step is achievable), thereby confirming that real-time control was indeed achievable with the selected control hardware and developed algorithms.

Sensor/communications system selection:

***Sensing**:* Selected components are summarized in Table 21.

Measured variable	Sensor	Manufacturer	Model
Angular rate, Angular position	IMU (Inertial Measurement Unit)	Lord Sensing	3DM-CX5-10
Position (through Elevation, Azimuth measurement)	Line Angle Sensor (LAS)	To be prototyped. Hall effect encoders will be used (by Melexis Tech.)	
Depth correction	Depth sensor	Blue Robotics	Bar02 (Pressure based)

Table 21: Chosen sensing tools for state variable measurements

Rationale for the selection of these components is as follows:

- IMU: The driving properties for selection were high sampling rates (>100 Hz), low bias instability (<8°/hr), low noise density (300°/s) and high resolution (0.003°/s). Among other factors, dynamic range, operation pressures and temperature, and size and mass were considered.
- Depth sensor: Resolution (0.16 mm), operation range (10 m depth), and size and mass were the driving properties considered for the depth sensor selection.
- Line Angle Sensor (LAS): The Line Angle Sensor was designed and prototyped by the team. It consists of an arm with two rotational degrees of freedom, which is connected to the tether. As the kite moved along its path, the tether and hence, the arm follow this path. This movement is measured using two encoders, each measuring one rotation. The design and measurement method is shown in Figure 62. A third encoder on the spool measures the tether length, which along with the elevation and azimuth is used to calculate the cylindrical co-ordinates of the Kite.

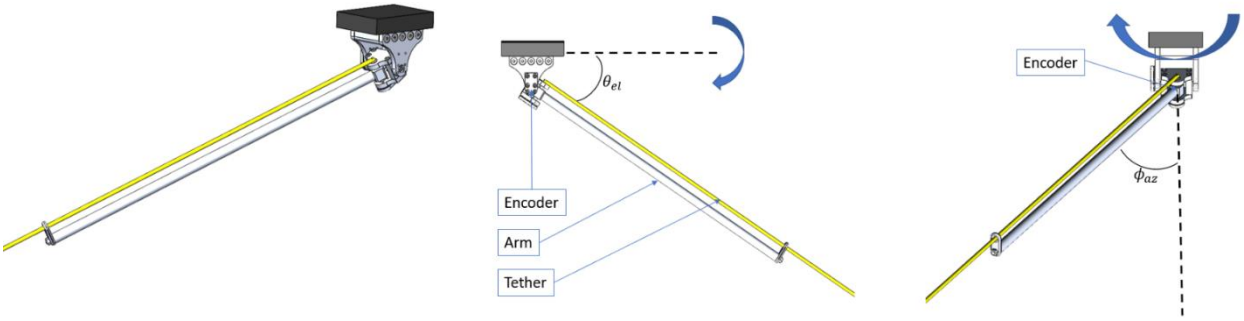

Figure 62: (Left) Isometric view of the LAS design; (Center) Side view of the LAS, showing measurement of elevation; (Right) Front view of the LAS showing measurement of azimuth angle.

Communications: All communications in the experimental system have been designed to reduce complexity. Wireless communications are not feasible for the underwater system, thereby requiring wired communication through the tether. Though the length of the tether in the water is small – 3-5 m for pool-based and 6-15 m for lake-based testing – the net tether length used for pool testing was much longer (approximately 30m), as it was also used to tow the raft (acting as a tow vessel) across the pool. RS485 was chosen among the few reliable protocols that provide reasonable data rates (>10 kB/s) at the required length for its relatively low complexity.

The winch/spool communicated with the ground station through CAN or MOD bus, depending on the chosen variable frequency drives. The LAS used encoders, which output Pule-Width Modulated (PWM) signals, which were read directly by the Speedgoat target machine.

Estimation Algorithm Design:

Because the kite's position cannot be measured directly, it must instead be estimated via a combination of a system model and sensors that act as *surrogates* for the kite's position.

To begin the process of estimator design, simulations were run with a multi-node (5 nodes) tether model, in order to quantify the accuracy of the LAS-based position measurement. In Figure 63, the difference in the LAS estimate and the positon predicted by the dynamic model can be seen – The LAS estimate is obtained by extrapolating the first link, which would coincide with the simulated 'true' position if the tether were completely taut and possessed no catenary shape.

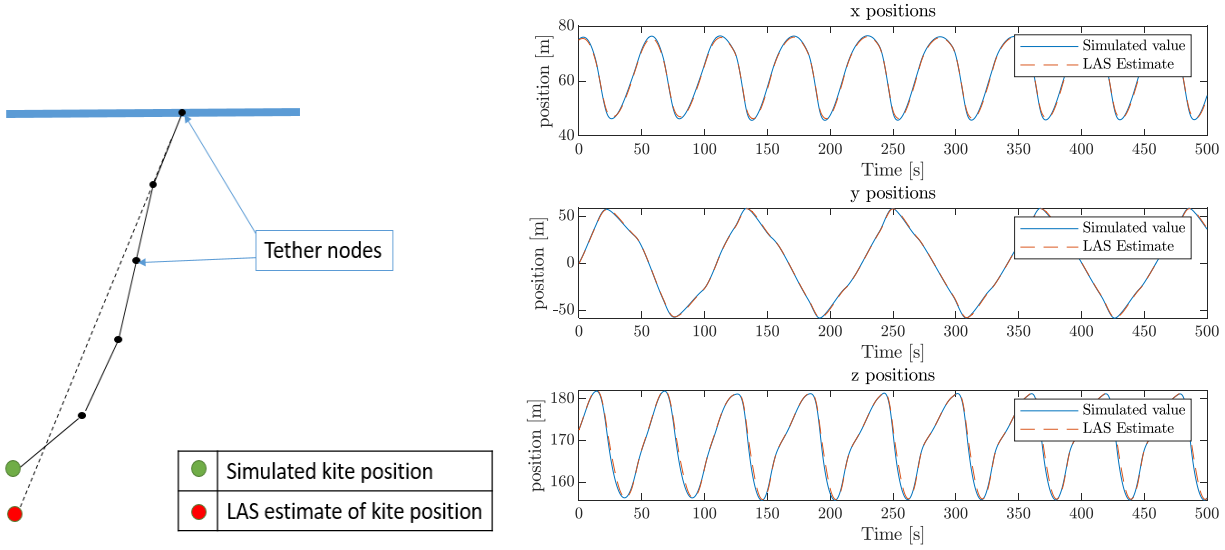

Figure 63: (Left) An exaggerated illustration of the difference between LAS estimate and the position estimated by the dynamic model. (Right) LAS and dynamic model positions co-plotted for 0.5 m/s flow speed. Both curves considerably overlap each other.

It is evident from these results that the error in the positon estimation is not significant. The error estimates under various simulation runs (corresponding to a range of flow speeds) have been tabulated in Table 22. The impact of this error on the performance was estimated by simulating the model with the LAS estimates as inputs to the flight controller. The table shows that there is little impact on performance (average power per lap). However, these numbers may vary when model uncertainties and measurement noise come into play.

Flow Speed [m/s]	**Performance**		**Maximum value of estimation error**				
	P_ideal [kW]	P_LAS [kW]	x pos [%]	y pos [%]	z pos [%]	El [deg]	Az [deg]
0.25	0.161	0.160	1.121	1.891	1.054	1.517	0.986
0.5	1.385	1.349	1.844	2.203	1.626	2.338	1.172

0.75	5.471	5.231	2.633	2.486	2.305	3.399	1.235
1	13.001	12.747	2.558	3.842	2.929	4.458	1.195
1.25	23.878	24.8	1.704	5.466	2.813	4.367	1.838
1.5	41.041	40.58	0.502	6.110	2.298	3.634	2.768

Table 22: Simulation results showing the impact of using the LAS position estimates on the performance and the max errors of positions and elevation (El) and azimuth (Az) angles – Direct measured quantities of the Line Angle Sensor (LAS)

Component-Level Testing

In its component-level testing, the team has focused on benchtop testing of candidate sensing, communication, and control equipment.

Subtask 5.4: Benchtop Testing of Candidate Control Electronics

As an example of an initial benchtop test, Figure 64 shows the interface in which the Lord Sensing IMU was tested to verify the angular position and rate measurements. The actual value (ground truth) was estimated with manual measurements.

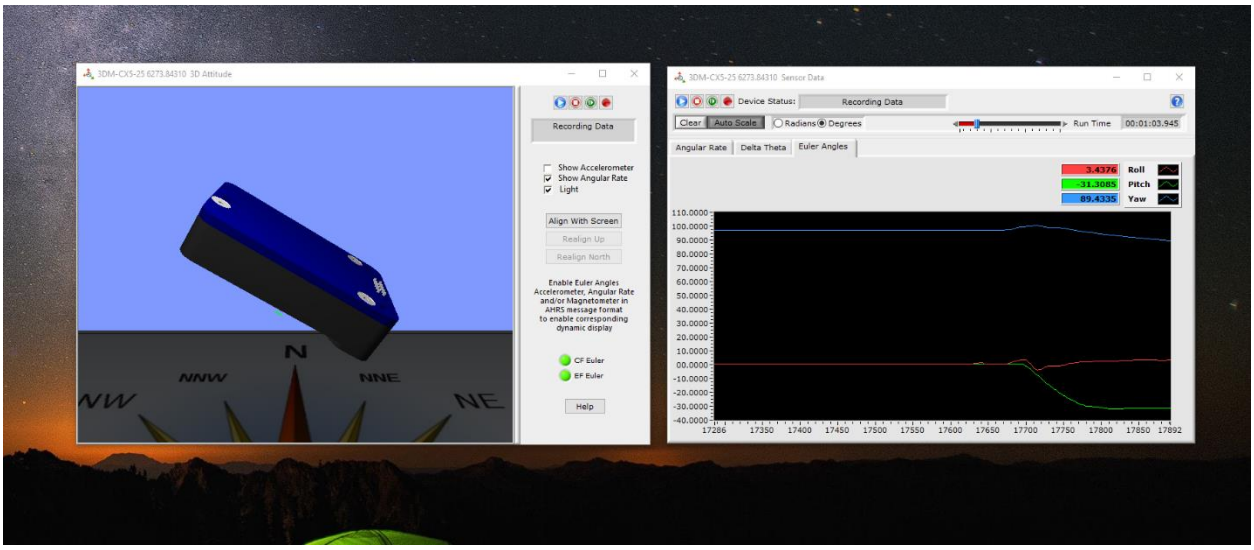

Figure 64: Snapshot of the IMU's computer testing/calibration user interface. The screen on the left the orientation (Euler angle) measurements being made by the IMU in real-time. The animation on the right show how the IMU interprets its orientation with respect to a reference (Using the ground plane with magnetic north pole as heading reference). The figure shows a pitched down positon.

Hardware-in-the-loop (HIL) testing served an essential role in confirming the team's readiness for pool-scale and, eventually, open-water testing. The high-level goals of the HIL testing are listed below:

- Establish effective communications between all sensing and computing hardware in the experimental setup.
- Verify the sampling rate and accuracy requirements for the controller to run without negative effects on performance.
- Verify the computation requirements for the controller.

The HIL testing campaign took on two flavors: The University of Maryland team prototyped and tested the PTO (Power Take-Off) system, and the NC State team prototyped and test the kite electronics, the Line Angle Sensor (LAS), and the tether communication system. Note that the onboard kite sensors and LAS constitute the sensing platform required for full state estimation, and thus, a controller in the loop test can be run. The testing took place in a 'dry' environment where the kite – a box containing the required electronics – was moved manually to check output control commands for the given data.

8 Pool-Scale Tow Testing

8.1 Test Setup

Experiments were conducted through a customized tow testing setup in the NC State Casey Aquatic Center 25-yard competition pool. Details regarding the test setup and experimental results are given here, with further insights and analyses archived in [19] and [20]. The system operated in the dive well, which offered an available depth of 3.35m (11 ft), a length of 22.9m (75 ft), and a width of 7.4m (24 ft). Figure 65 shows the overall setup. In this setup, the kite is suspended in the pool from a catamaran-style raft, via a tether of prescribed length (between 2 and 3 meters from the raft to the kite for the experiments performed in this work). The raft is towed across the pool by a winch located on the pool deck, which is co-located with the system controller. Lateral motion is restrained through a pair of guy wires tensioned between the sides of the pool, which engage with four guides arranged in a 1m x 1m grid about the center of mass of the raft. The system can achieve tow velocities up to 1 m/s.

Communication between the ground station and raft is accomplished via two tethers. The first tether, referred to herein as the tow tether, is used to pull the raft across the pool and transmits data from a suite of sensors local to the raft. The second tether, referred to herein as the kite tether, is used to suspend the kite from the raft and transmits data between the kite and the controller and carries power to the kite. The kite tether passes through a line angle sensor (LAS) suspended from the bottom of the raft, which encodes the instantaneous orientation of the tether.

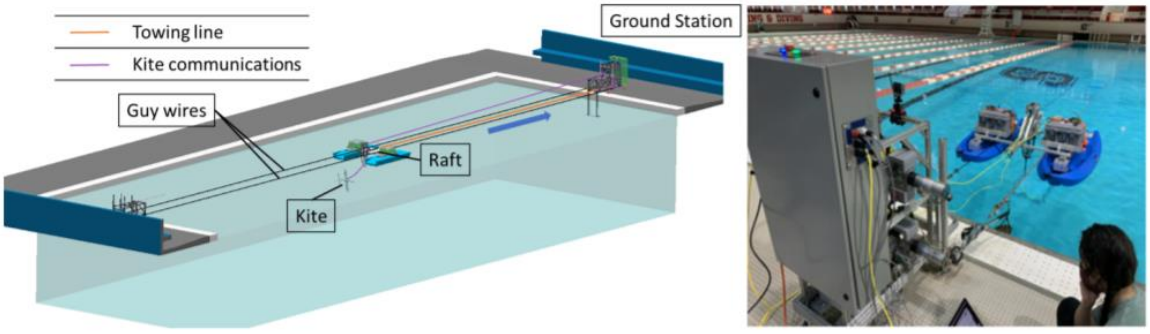

Figure 65: Overall pool-based tow testing framework.

The pool-based framework not only represents a significant advancement with respect to the earlier water channel-based validation (performed at 1.5:100-scale and shown in Figure 66 – left); it also represents a first amongst academic institutions seeking to validate open-source kite dynamic models and control algorithms, in addition to making their tow framework accessible to others. Compared to the previous leading academic effort aimed at tow testing of kite devices, as deployed by David Olinger's research group out of Worcester Polytechnic Institute (WPI) and depicted in Figure 66 – right, our team's tow testing framework incorporates two critical advancements:

- First, unlike the framework of the WPI setup where a rigid rod is used as a tether and rigidly fixed to the kite (thereby eliminating two of the kite's rotational degrees of freedom), the kite in this effort is attached via a flexible tether and possesses a full six degrees of freedom, along with full actuation via ailerons, a rudder, and an elevator.
- Second, the kite is fully autonomously controlled, as opposed to joystick-operated control used in other setups.

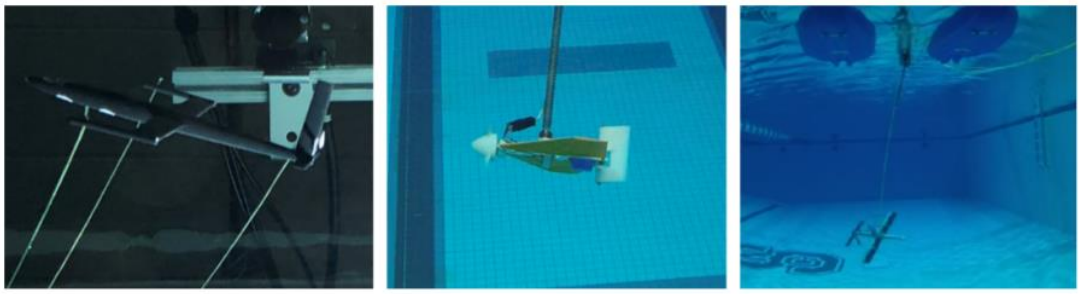

Figure 66: Comparison of the team's earlier water channel setup (left), the WPI pool testing setup (middle), and the NC State team's full degree-of-freedom, fully autonomous pool testing setup.

The remainder of this section briefly summarizes the key hardware involved with the tow testing setup.

Tow hardware: The tow system consists of two towing tethers – one to tow the raft and another to tow the kite. The raft is pulled along tensioned guy wires, which dramatically limit the lateral sway achievable by the raft. A retraction system at the opposite end of the pool provides prescribed tension, which keeps the tow tether in tension at all times.

Winch and ground station: The winch and ground station contains three core components, namely two winches and a main electrical enclosure. The two winches are used to regulate the speeds of the raft tether and kite tether. The electrical enclosure contains fuses, circuit breakers, power supplies, motor controllers, and the main Speedgoat computer, which is used to run the real-time control algorithms that regulate the behavior of both the kite and tow system. The main Speedgoat communicates with a host computer (monitored on the pool bleachers by the test operators) over an Ethernet link, with a UDP link used to communicate between the main Speedgoat and raft (which contains an additional Speedgoat), and a serial link (RS-485) used to communicate with the kite.

Raft and line angle sensor: The raft is used to aggregate two sets of signals critical for control and data analysis, namely the tether angles and tension. A line angle sensor, depicted in Figure 67, characterizes the azimuth and elevation angle of the kite. Because the tether contains curvature, which is not particularly pronounced in pool experiments but will be more pronounced in open-water experiments, these estimates can be corrected via a state estimator, detailed in the quarter 10 report and the control system section of this report. The raft also contains a load cell unit, which measures tether tension through a redirect system. Both the line angle sensor measurements (via two encoders) and the load cell measurements are aggregated on a Speedgoat real-time computer, which are in turn relayed to the ground station unit over a UDP link.

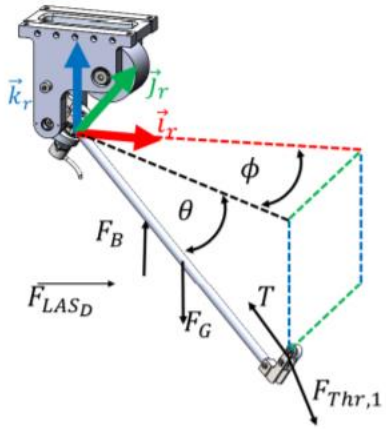

Figure 67: Line angle sensor schematic.

Kite design: The kite consists of a sealed aluminum fuselage with an electronics "sled" contained therein, which includes a customized printed circuit board (PCB) that includes a microcontroller, two RS-485 communication modules, an inertial measurement unit (IMU), depth sensor, and associated circuitry. The kite is equipped with waterproof servos that are used to control the rudder deflection (note that the full vertical stabilizer deflects in this design), elevator deflection (note that the full horizontal stabilizer deflects in this design), and aileron deflection. The Blue Robotics tether, which communicates with the kite over RS-485, is attached to the kite via wet-mate connectors.

The kite CAD and PCB layout are shown in Figure 68. The kite has a wingspan of 0.847m, a nose-to-tail length of 0.674m, and a fuselage diameter of 0.0635m. Hydrodynamic surface specifications are given in Table 23. SG6040 foils were chosen for the wings in order to mitigate low Reynolds number effects encountered in the cross-current flight regime of the NC State pool. Kite control is accomplished via waterproof SAVOX SW1250MG servo motors. The kite ailerons are located at the far outboard extent of the wings, each with spans of 0.2m at 25-18.5% chord, decreasing as the aileron moves outboard. The entirety of the horizontal and vertical stabilizers are pitched by servo motors about the quarter chord location to enable rudder and elevator control.

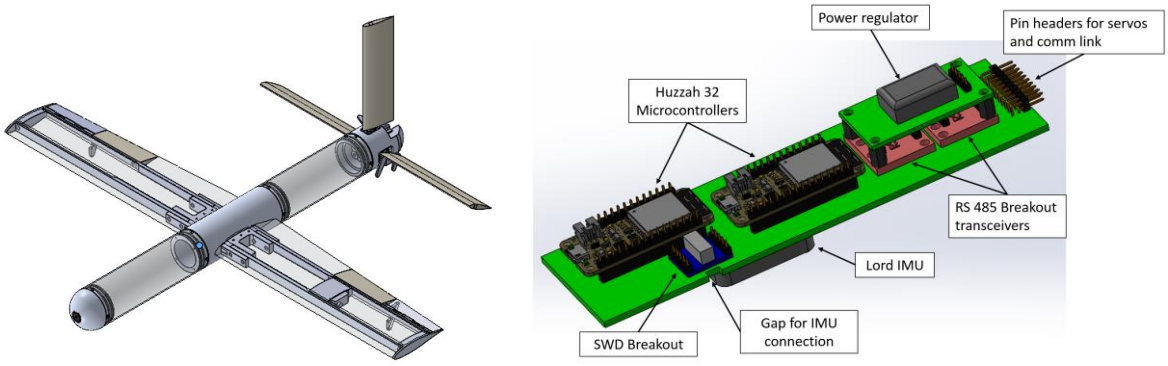

Figure 68: Kite CAD (left) and PCB design (right).

Surface	Foil	Span (m)	Root chord (m)	Taper ratio
Wings	SG6040	0.847	0.128	0.8

Vertical stabilizer	NACA 0015	0.200	0.055	1
Horizontal stabilizer	NACA 0015	0.442	0.055	1

Table 23: Key geometric properties of the kite's hydrodynamic surfaces.

Control system: The full-scale kite control system has been designed to perform two critical tasks:

- Execute figure-8 flight paths via a hierarchical controller designed during budget period 1.
- Strategically spool tether out during high-tension flight and spool tether in during low-tension, non-cross-current flight. This switching control requires robust transitions into and out of cross-current flight.

Because of the limited tow length available in the pool, which makes it difficult for the kite to quickly lock onto a prescribed path, along with the limited tether length, which makes path tracking difficult in general, a truncated version of the previously described hierarchical controller was used in pool testing. This truncated controller is shown in Figure 69 (left). This controller makes use of the third and fourth layers of the full hierarchical controller, where the roll and yaw angle setpoints are prescribed based on simulations of the four-layer hierarchical controller. Figure 69 (right) shows how predicted roll and yaw angle trajectories from simulations were used to formulate phase-shifted sinusoidal roll and yaw angle setpoint profiles.

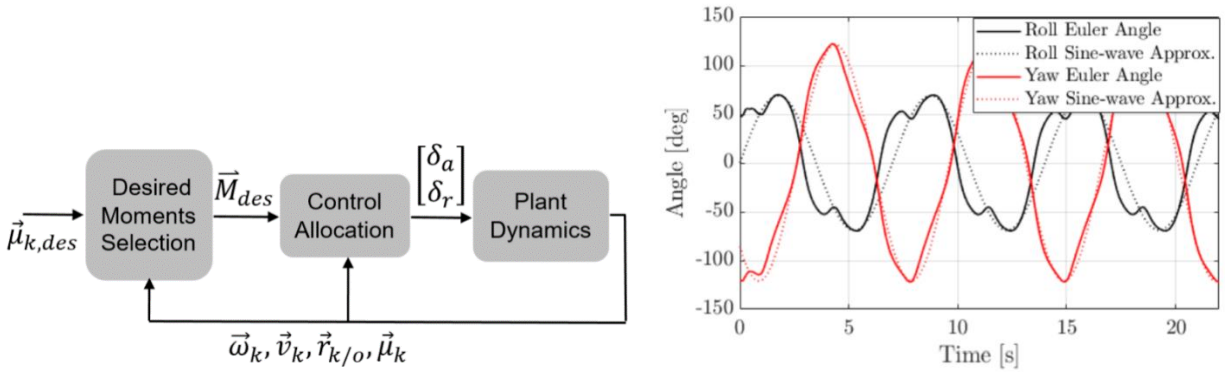

Figure 69: Block diagram of the truncated controller used in pool testing, along with an example of how realized roll and yaw angle trajectories from simulations were used to inform phase-shifted sinusoidal roll and yaw trajectories.

The "desired moment selection" block consists of two parallel filtered PID controllers: one for roll control and the other for yaw control. The "control allocation" block performs an inversion of the nonlinear system equations to determine the values of aileron and rudder deflections that achieve the target roll and yaw moments.

A final element of the control system, namely a state estimator, fuses a model of the tether dynamics (which accounts for tether curvature) with measurements from the LAS, load cell unit, and depth sensor to maintain a running estimate of the kite's position. This estimator contains a predictor that is based on the nonlinear dynamics of the LAS, raft, and tether, along with a linear corrector that is driven by the aforementioned measurements.

8.2 Initial Model and Controller Validation Under Constant Flow

Attitude control under constant tow speed: In performing our assessment of attitude control (and resulting azimuth and elevation angle behavior, along with velocity augmentation ratio and power augmentation ratio), we examined three variants of the truncated controller of Figure 70:

- *Roll control only:* Here, the rudder deflection is set to zero and only the roll angle is controlled to a sinusoidal profile. Because of the limited extent of cross-current flight made available through the actuation of the ailerons alone, the roll setpoints were limited to amplitudes no larger than 30 degrees under this control mode.
- *Combined roll and yaw control with "diagonal" control allocation:* Here, phase-shifted sinusoidal roll and yaw angle setpoints were prescribed, with individual amplitudes specified for each. Roll and yaw setpoints with amplitudes up to 60 and 80 degrees, respectively, were experimentally characterized. As noted previously, the setpoint amplitudes and phase shift were determined based on simulations of the multi-layer hierarchical controller of Figure 13. In these experiments, only the diagonal elements of the control allocation matrix were retained, restricting the ailerons to be used for roll control only and the rudder to be used for yaw control only.
- *Combined roll and yaw control with full control allocation:* As with combined roll and yaw control with a diagonal control allocation matrix, phase-shifted sinusoidal roll and yaw angle setpoints were prescribed, with roll and yaw setpoint amplitudes up to 60 and 80 degrees, respectively. However, these experiments utilized a full control allocation matrix, wherein the matrix relating the achieved moment coefficient vector to the control surface deflection vector was inverted in order to determine the required deflection vector at each time step.

Experimental results in Figure 70 (left) illustrate the setpoint tracking achieved under each control approach. Figure 70 (right) shows the resulting azimuth and elevation angles. Finally, Figure 71 characterizes the velocity augmentation ratio, given by $\left|\frac{v_{app}}{v_{tow}}\right|$, along with the power augmentation ratio, which is the cube of the velocity augmentation ratio.

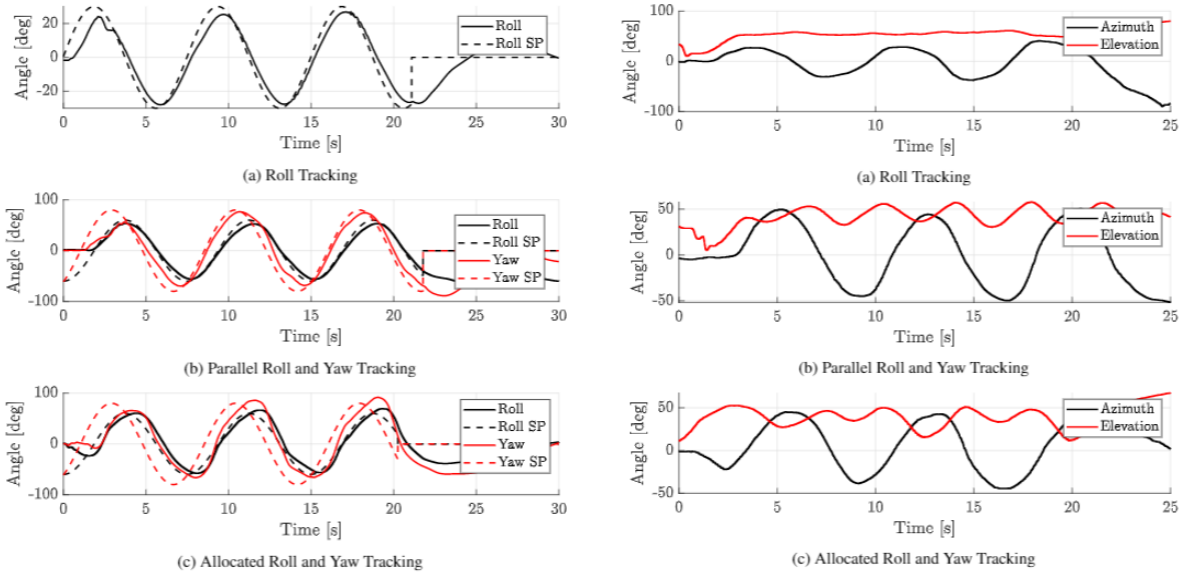

Figure 70: Left: Tracking performance under (a) pure roll control, (b) roll and yaw control with a diagonal control allocation matrix, and (c) roll and yaw control with full control allocation. Right: Azimuth and elevation angles under (a) pure roll control, (b) roll and yaw control with a diagonal control allocation matrix, and (c) roll and yaw control with full control allocation.

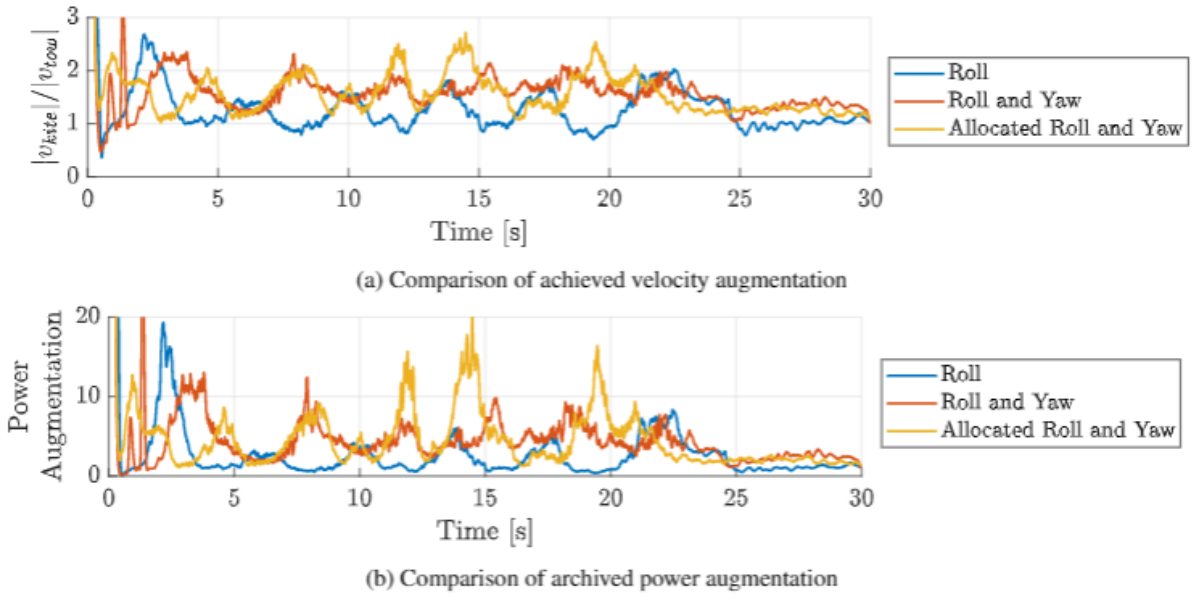

Figure 71: Velocity augmentation (top) and power augmentation (bottom) under the three considered control approaches.

As expected, performance improves as the sophistication of the underlying controller increases. In addition to evaluating performance under the considered control approaches, it is instructive to examine the level of agreement between the model predictions and the data. This assessment is provided in Figure 72, which examines the agreement between the model and data in terms of the azimuth angle, elevation angle, velocity augmentation ratio, and power augmentation ratio. Model vs. data comparisons for the roll and yaw angles show incredibly good agreement but do not represent a fair measure of assessment, since these variables were in fact controlled to setpoints. It is noteworthy that the largest source of disagreement lies in the power augmentation ratio, which stems from the fact that this is a cubic function of the velocity augmentation ratio.

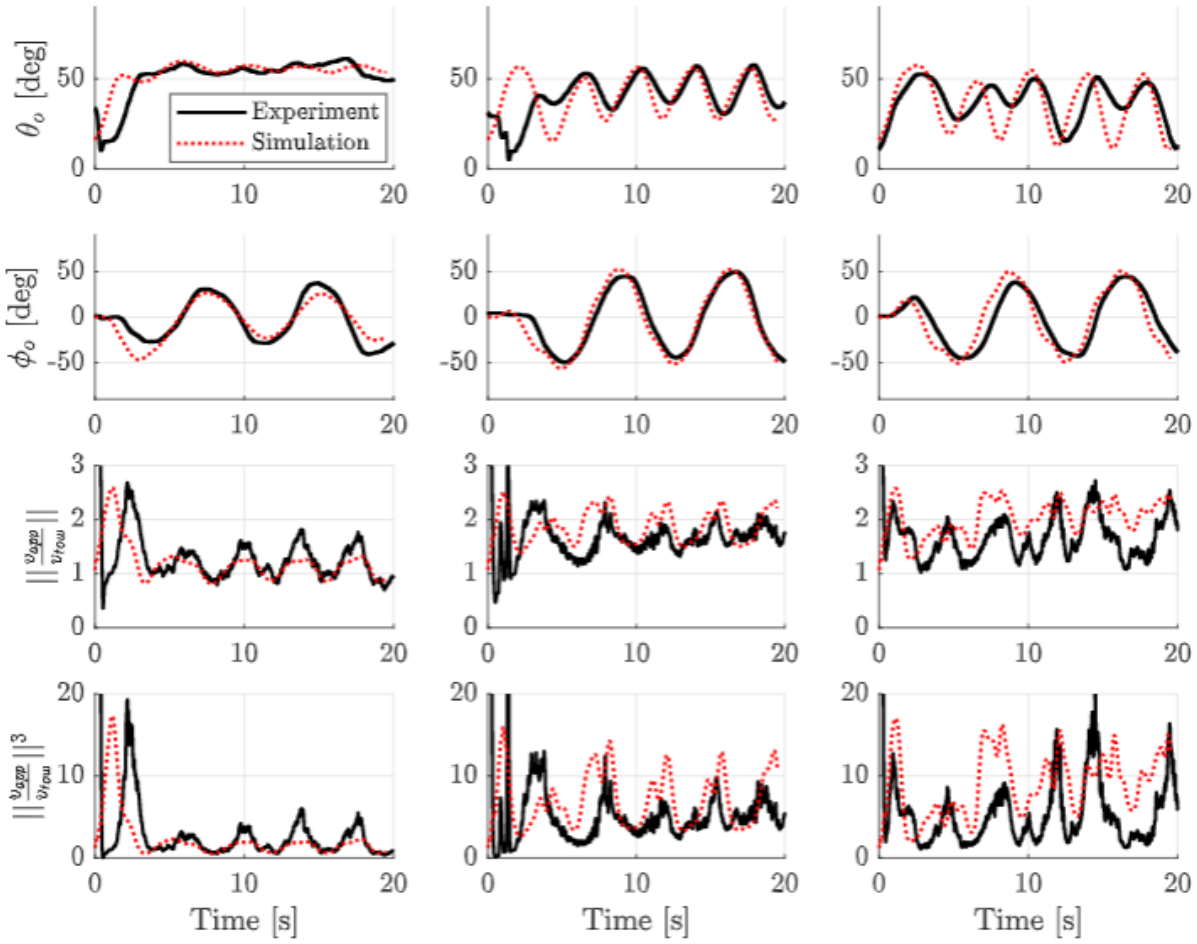

Figure 72: Model vs. data comparisons. The rows correspond to azimuth angle (first row), elevation angle (second row), velocity augmentation ratio (third row), and power augmentation ratio (fourth row). The columns correspond to the roll-only controller (left), combined roll and yaw controller with diagonal control allocation (middle), and combined roll and yaw controller with full control allocation (right).

8.3 Power Projections Based on Tow Testing

In addition to comparing the model predictions against the data, the pool testing results can be used to make projections as to the power output that will be achieved under spool-out/spool-in operation in open-water (lake) testing. To do this, net power was estimated by measuring tether tension under both steady level flight (indicative of non-cross-current spool-in operation to be performed in open-water environments) and cross-current (indicative of the spool-out operation to be performed in open-water environments) flight at different tow speeds. A quadratic curve fit was used to extrapolate tension across a range of tow speeds. The mechanical power produced or demanded by the system under spool-in and spool-out operations was characterized as:

$$P_{net} = \gamma v_{tow}^3 [k_{out}(1-\gamma) - k_{in}(1+\gamma)]$$

where γ, referred to as the *spooling speed ratio*, is given by:

$$\gamma = \left|\frac{v_{spool}}{v_{tow}}\right|.$$

Projections were made based on both the average and peak tensions observed during cross-current flight, noting that the average tension in an open-water environment with fewer space constraints is in fact expected to lie between these two values.

It is instructive and also relevant to the kite design community to examine how the resulting projected net power will vary as a function of spooling speed at a given tow speed, as well as how the maximum achievable power will vary as a function of tow speed (the latter quantity describing the power curve of the kite). In particular, Figure 73 provides power curves for a variety of spool speed ratios (0.1, 0.2, and 0.3). Figure 74 addresses the tradeoff between spooling speed ratio and power output for a number of tow speeds. The peaks in this family of curves can be used to generate a single power curve that characterizes the overall device.

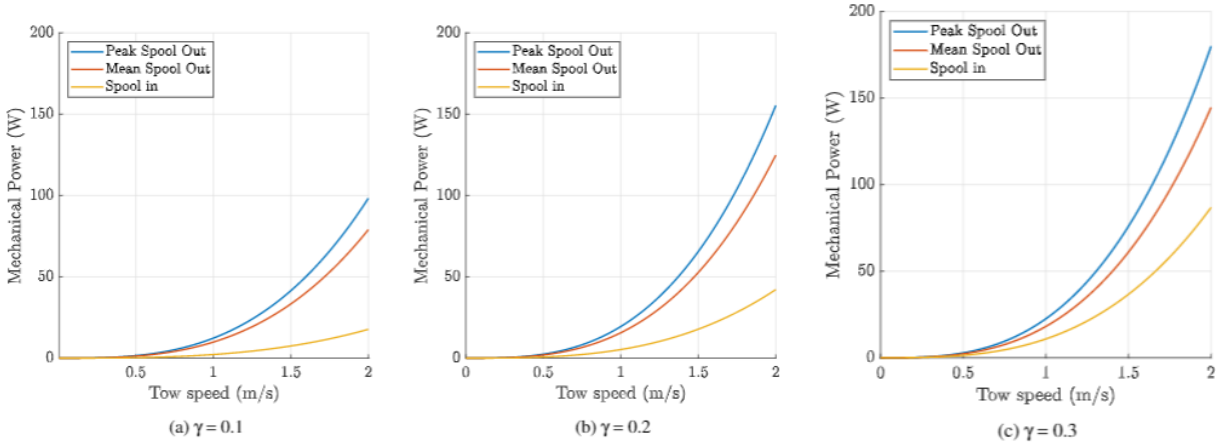

Figure 73: Projected power curves at different spooling speed ratios.

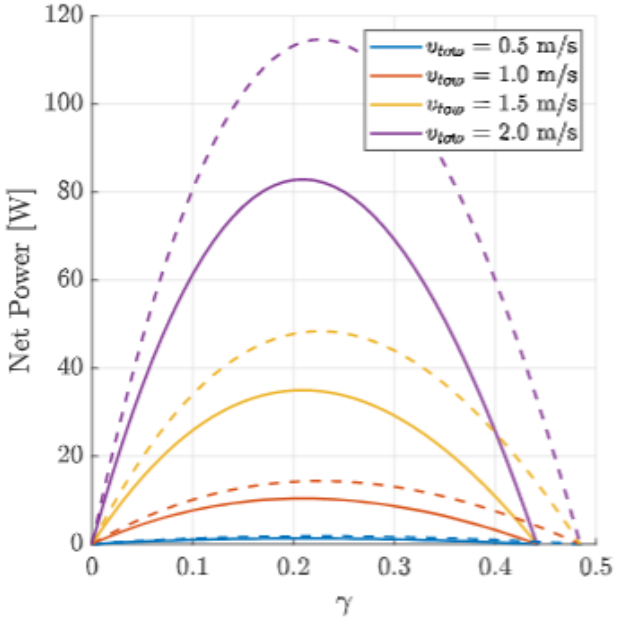

Figure 74: Projected net power (lap-averaged) vs. spooling speed ratio over a range of tow speeds.

8.4 Turbulence Emulation (and Associated Results)

To de-risk open-water testing operations, where the vessel tow speed will not be constant (due to flow disturbances and other perturbations) and additional flow disturbances may affect the local flow speed at the kite but not the tow vessel, the team performed pool-based experiments where a sinusoidal tow speed disturbance of up to 10 percent of the base tow speed was superimposed on top of the winch speed command. Based on identified frequencies over which the kite's closed-loop response is expected to be most sensitive to flow disturbances, the team applied these flow disturbances at frequencies up to 1 Hz. Results of turbulence emulation are summarized here and also discussed in detail in [21].

Figure 75 shows the resulting elevation and azimuth angle behaviors under the most severe tow disturbance, consisting of a 10 percent speed disturbance with a frequency of 1/3 Hz. As can be seen, the response of the kite under this disturbed environment is very similar to the elevation and azimuth angle behavior observed in Figure 70, which were performed without the presence of a longitudinal disturbance.

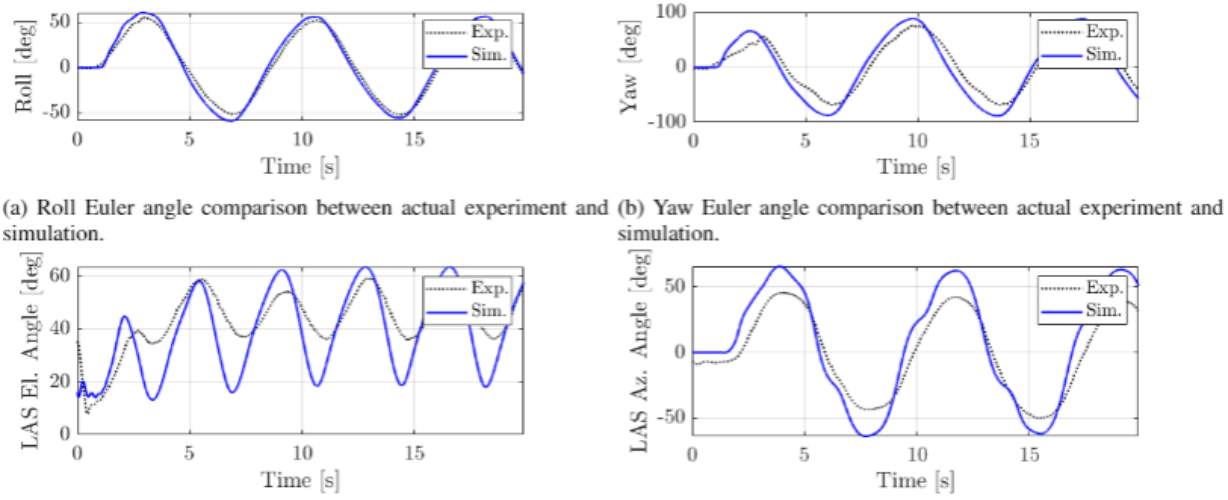

(a) Roll Euler angle comparison between actual experiment and simulation.

(b) Yaw Euler angle comparison between actual experiment and simulation.

(c) Line angle sensor elevation angle comparison between actual experiment and simulation.

(d) Line angle sensor azimuth angle comparison between actual experiment and simulation.

Figure 75: Examination of kite performance in the presence of a sinusoidal longitudinal tow speed disturbance of 10 percent of the nominal tow speed, at a 1/3 Hz frequency.

Transitioning into and out of cross-current flight: In order to de-risk open-water testing operations, where the kite must repeatedly transition from non-cross-current operation into cross-current operation and vice versa, the team performed a series of pool experiments where it "deconstructed" the transition operation, focusing either on (i) transition into cross-current flight from a free-hanging position or (ii) controlled transition out of cross current flight into steady, level flight, within a single tow length. Figure 76 shows sample results from transitioning into and out of cross-current flight in the pool.

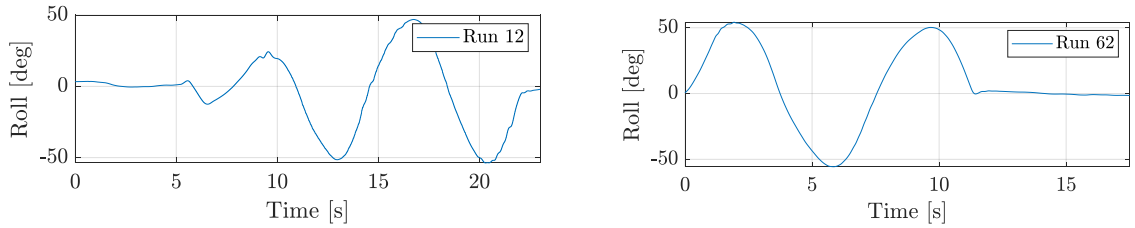

Figure 76: Sample experimental results transitioning into (left) and out of (right) cross-current flight during a pool-scale tow test.

9 Open-Water Tow Testing

9.1 Test Setup

Figure 77 shows the test vessel, overall vessel layout, and a Navionics chart of the permitted tow testing area. The vessel setup consists of several components:

- A winch and level wind system, driven by a brushless DC motor, is used to perform spooling operation. This corresponds to item 1 in Figure 77.
- Tether is routed through a load cell redirect and rollers, down a boom. The tether routing corresponds to item 2 in Figure 77.
- A line angle sensor is used to measure the angle of the tether at its base. This, in conjunction with a Pitot-based flow measurement, is labeled as item 3 in Figure 77.
- Inside the test vessel, a control and computing center adjacent to the helm is used to perform real-time kite control computations and data acquisition.
- A battery and inverter inside the vessel are used for energy storage and conversion to AC.

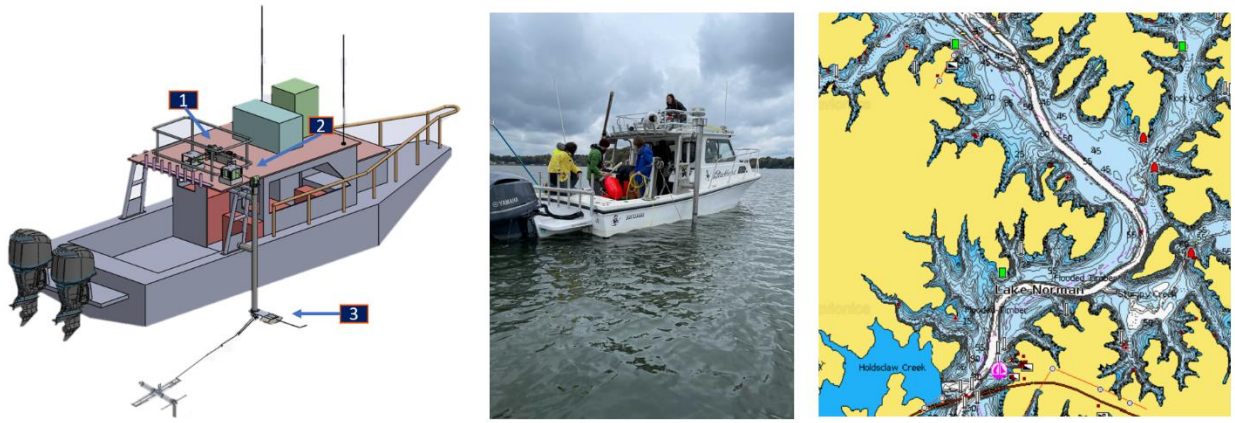

Figure 77: Test vessel setup and Lake Norman testing area.

Detailed mechanical and power take-off setup: Using the roof of the Privateer as the base of operations, a Power Takeoff System (PTO) was designed to bolt in place with existing mounting points and pass loading through the Privateer's A frame in a safe manner. Featuring primarily aluminum construction and a polycarbonate safety enclosure, the PTO was designed in modular fashion, permitting easy installation and servicing of components. Bracket hole spacing and component selection was done in such a manner

to provide maximum serviceability in the event of component replacement, which did occur in several instances. Polycarbonate was used over acrylic because of its higher shatter resistance, as personnel safety was a primary design consideration. Spatial constraints on the roof of the Privateer also required a chain driven, dual drivetrain layout, which conveniently powered the level wind mechanism as well. The upper drivetrain featured a 40V DC motor, an ATO DYN-200, 1000 Nm capacity torque sensor, a Taidacent 12 conductor slip ring, a custom aluminum spool and an ANSI type 35 chain sprocket. The lower drivetrain featured the same style and size sprocket, operating on a 1:1 ratio with the upper drivetrain, to allow a rotary encoder to function in a feedback control capacity for the motor. The same drive system was connected to a third sprocket, mechanically driving the level wind mechanism at the same 1:1 ratio.

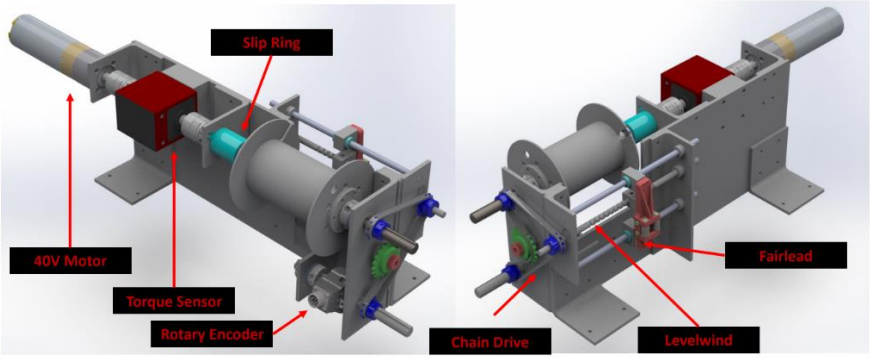

Figure 78: Detailed winch, motor, and level wind setup.

The importance of the level wind was paramount in ensuring the tether consistently wound around the spool, rather than compounding in one location, resulting in a dramatic change in drum radius. This was demonstrated when set screw failure nearly resulted in a tether snap event where the level wind wound the tether consecutively in one spot on the drum for several rotations, causing the tether to overrun the spool flanges and partially tear at a pinch point. The friction of the PTO system was quantitated on Lake Norman to be approximately 16 percent, allowing the team to derive true kite performance from measured values.

To ensure tether working capacity was not exceeded, a 1000 lb capacity Omega load cell was mounted outside of the PTO enclosure on the roof of the Privateer. Using Delrin rollers, the tether was routed in a 180° wrap fashion before being sent to another redirect mounted to the top of the vertical boom. The assembly housing the load cell was studied through finite element analysis, ensuring a safety factor of 1.81 was achieved at maximum load (double the tether's working limit, or 160 lbs). A ball bearing fairlead was mounted to the Load Cell Assembly as shown in Figure 79, to ensure the tether did not derail off the roller during low tension events. It was found during bench top testing that low tension events posed sever risk to the tether, as the sudden reapplication of tension could bring the tether in contact with sharp edges on nearby components. By continuously monitoring tether tension, the team ensured that the working capacity was never exceeded, except when unavoidable at higher tow speeds. This upper speed limit was found to be 2 m/s, where the tether failed and was subsequently replaced. Mounted to the bottom of the boom was a Line Angle Sensor, allowing accurate tracking of the spatial position of the kite for both power estimation and safety (proximity to the prop) purposes.

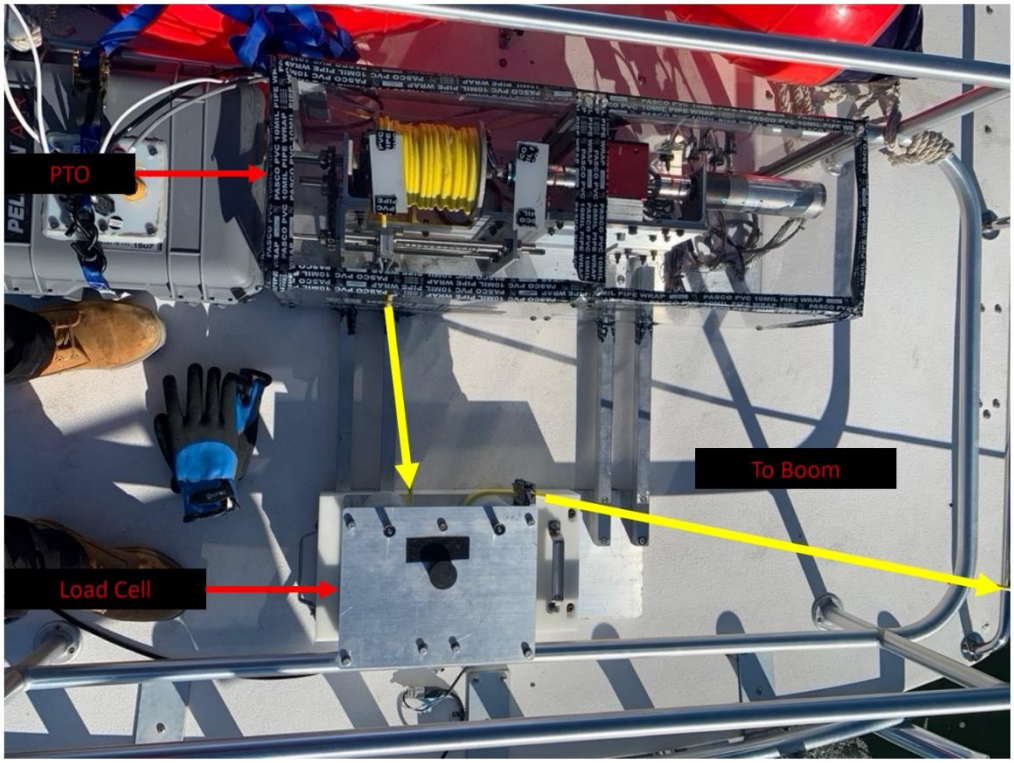

Figure 79: Detailed test vessel roof top setup.

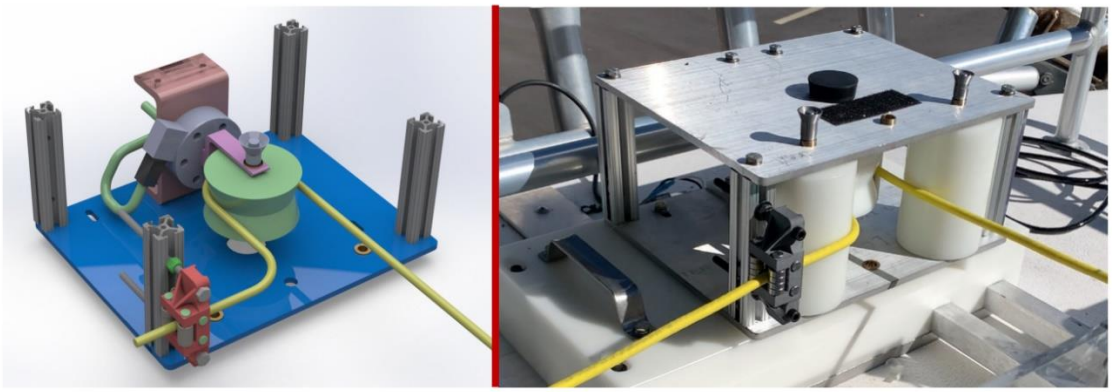

Figure 80: Detailed load cell setup.

From Figure 79, the entirety of the PTO system can be viewed. This system provides power measurement via three methods, all of which are recorded via a Simulink Real Time model at a 100 Hz sample frequency:

1. Electrical - model records current flow, but voltage is read manually from battery display. Being the farthest component upstream of the kite, it subject to the highest degree of frictional losses.
2. Mechanical/Torque Sensor - model records torque data, which is invariant with drum radius, a variable that, regardless of level wind, is subject to a higher than desired level of uncertainty. It is located downstream of the motor, but is still subject to higher frictional losses than the load cell.

3. Mechanical/Load Cell - model records tether tension data, but calculating power requires linear speed which subsequently requires use of the drum radius, a variable subject to higher than desired uncertainty. However, the load cell is the farthest downstream sensor, subject to the lowest level of frictional losses. For this reason, it was the sensor of choice for power measurement and friction analysis.

In Figure 81, the boom's upper redirect and the Line Angle Sensor can be seen, depicting how the tether was routed from the load cell to the kite. Dry-ground testing was performed, and due to the low clearance between the base of the boom and the pavement, the boom was mounted at a skewed angle to provide adequate clearance for the Line Angle Sensor. In an open-water setting, the boom is perpendicular to the water surface.

Figure 81: Boom and redirect system.

Detailed sensing, computing, and control setup: In terms of instrumentation and control, the key differences between the pool and lake-based experimental setups were (1) significantly larger operation depths and consequent tether lengths, and (2) spooling in and out operation, while accommodating regen during spooling out. To achieve this, a new a power take-off system was designed along with a new electrical enclosure to accommodate the refined sensor suite and control system setup. The lake-based setup leveraged the line angle sensor (LAS) and load cell used in the pool, the flight-tested 1/10th scale kite, the tether setup used for power and data transmission to the kite, and the computational control hardware. The flow speed was emulated by the tow vessel movement, which was assumed to be the speed over ground, recorded with an on-board GPS (Global Positioning System) sensor.

The experimental setup consists of four subsystems: (1) the kite, equipped with inertial and depth measurement sensors, servo motors to actuate control surfaces, and micro-controllers for communications; (2) the power take-off (PTO) setup, which includes a winch motor, an encoder, a torque sensor, and a battery connected via a current sensor; (3) the line angle sensor (LAS) and the load cell, housed at the end of the boom, and along the cuff attachment respectively; (4) the base station setup,

which includes two Speedgoat computers, an electronics cabinet for electrical routing, and a command station for the operator to carry out experiments. The location of each of the subsystem is shown in Figure 82, labeled in the order described above.

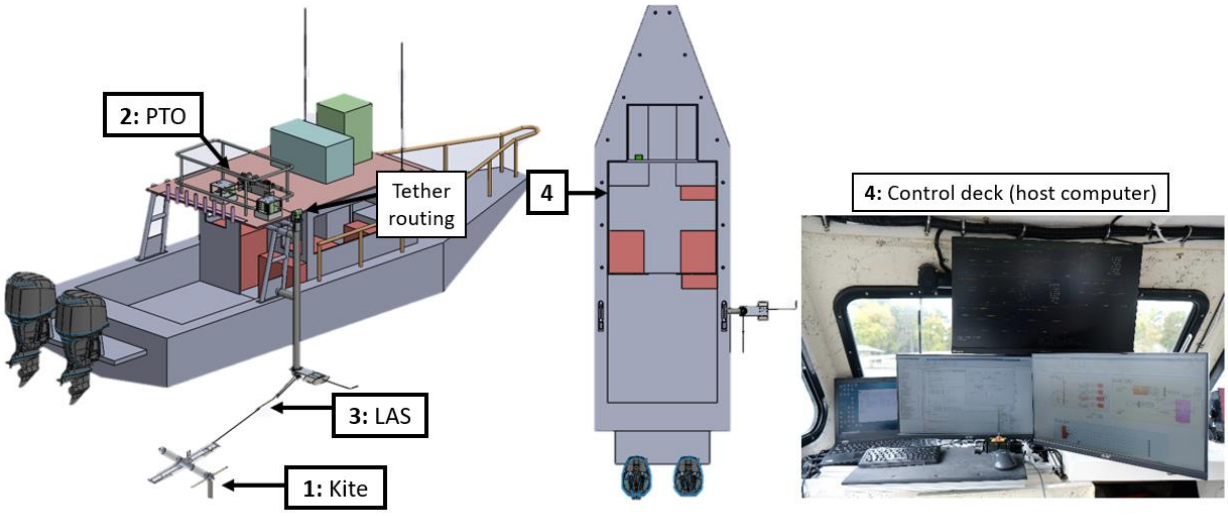

Figure 82: A CAD rendering of the tow vessel, showing the position of each subsystem and the control deck.

Communication workflow

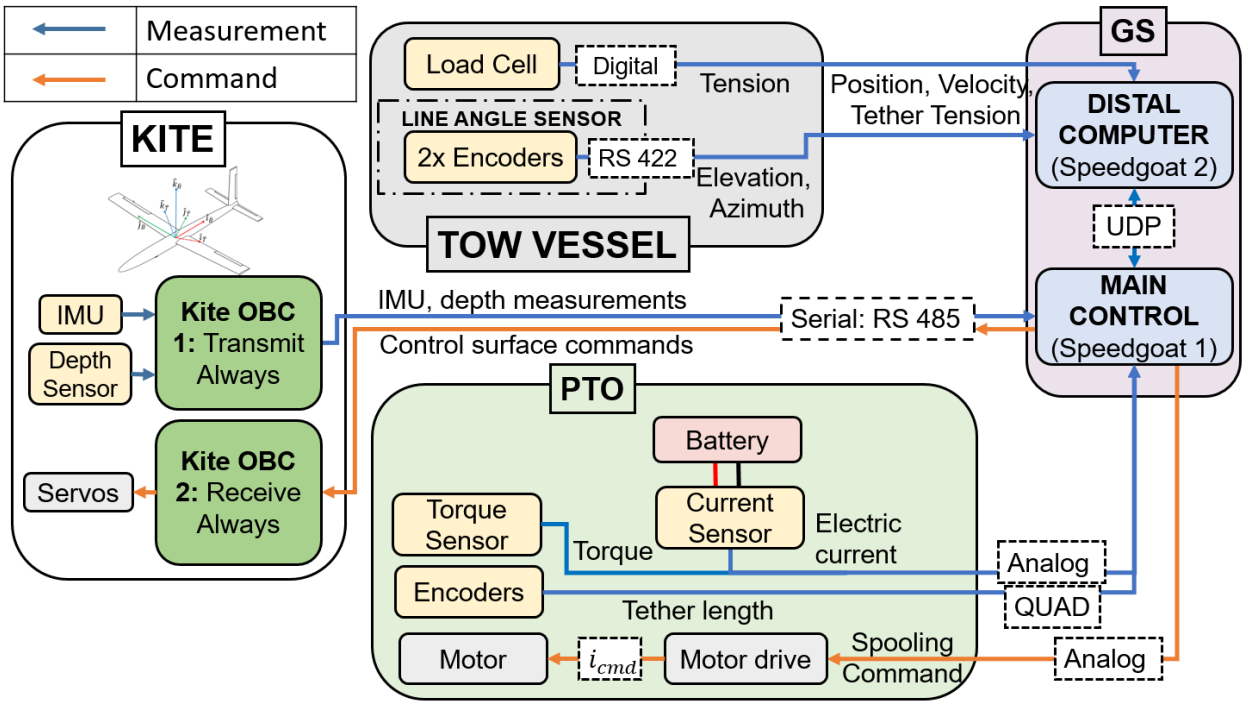

Figure 83: System instrumentation and communication workflow

The experimental setup is monitored by operators through a host computer via a custom graphical user interface (GUI). The GUI enables the operators to issue parameter updates and set points to the kite and

the PTO in order to control the kite's flight and spooling operation respectively. The updates are then relayed to the target computer, which manages data acquisition from the sensors and implements the controller in real time. Figure 83 shows the communication and control work flow of the experimental setup. Here, i_{cmd} represents the commanded motor currents post conversion of the analog speed commands by the motor drive (off the shelf motor controller), and GS = ground station. The working of each component of the setup is described below:

Kite subsystem: The kite is equipped with an IMU that measures Euler angles and accelerations, and a pressure sensor that measures the depth in water. These measurements are sent to an on-board transmit-always microcontroller (OBC1) that packages and relays the information to the ground station via serial communication (RS 485 protocol was used). The ground station processes the measurements, and the generated control commands are then sent back to the kite via serial RS 485 as well. The control surface actuation commands are relayed to the respective servo motors by the receive-always on-board microcontroller (OBC2). Each control surface is assigned a servo motor, with a total of four motors in use (two ailerons, an elevator and a rudder). Power and data transmission occurs through the conductors within tether that runs between the kite and the winch system.

Power take-off (PTO): The power take-off consists of an in-line torque sensor and encoder that respectively measure the torque and the angular position of the winch. The motor is driven by a 48V battery and a motor drive (motor controller), the combination of which allow regeneration events during motoring. An inline bi-directional current measures the current, which, along with the battery voltage is used to assess electrical power. The battery voltage is digitally displayed on the battery, and is manually noted by the operator (through the GUI) on a regular basis. The manual measurement is reasonable in this case as the voltage change is minimal -- average observed changes of 0.1V per run, and total change of 2V over the entire testing campaign. The spooling speed commands are sent as an analog voltage signal to the motor drive that converts it to BLDC motor current commands before relaying it to the motor.

Tow vessel: In addition to the aforementioned sensor suite, the setup features a load cell and a line angle sensor (LAS) that measure tether tension and the position of the kite respectively. The line angle sensor, also used in the pool-based setup, measures the elevation and azimuth the kite is flying at. The angles along with tether length (measured by the PTO encoder) can be used to estimate the position of the kite in spherical co-ordinates, assuming the tether is straight. In reality, the tether drag induces curvature in the tether and the straight tether assumption does not hold. However, the elevation and azimuth angles are still indicative of the flight performance. The load cell tension and the line angle sensor encoder measurements are directly transmitted back to the ground station. The measurements are received, packaged and relayed to the main control computer by the distal computer via UDP (User Datagram Protocol) at the ground station.

Ground station: The ground station houses the main control computer and the distal computer. Both the computers are Speedgoat[1] baseline M machines equipped with the required IO (input-output) interface for hardware integration. A laptop is used to modify and deploy control algorithms on the target computer (Speedgoat 1). Flight operations are carried out by a human operator through a custom GUI (graphical

[1] Speedgoats are rapid control prototyping hardware that use Simulink Real-time to deploy control algorithms, allowing for rapid software reconfiguration

user interface), which offers the ability to tune gains, modify flight and winch control parameters, and toggle between modes of operation.

Subsystem	Component description	Manufacturer	Model
Kite	IMU	Lord sensing	3DM-CX5-25
	Depth sensor	BlueRobotics	Bar02
	RS 485 transceiver	Sparkfun	SP3485
	OBC (1 and 2)	Adafruit	Huzzah-32
	Servo motors	Savox	1250mg
PTO	Torque sensor	ATO	ATO-TQS-DYN-200
	Encoder (tether length)	Encoder Co.	260-N-R-15-S-1800-Q-OC-1-S-SD-2-N
	Current sensor	Polulu	ACS724
	Battery	BigBattery	48V BDGR GEN-2
	Motor drive	Roboteq	HBL2360A
	Motor	ebm-papst	ECI-63.40-K1
Tow vessel	Tether	BlueRobotics	Fathom
	LAS encoders	RLS	RM22IC
Ground station	Computers	Speedgoat	Baseline M

Table 24: Summary of open-water test components

Cables from each subsystem were routed into the tow vessel cabin, to an electrical enclosure, which was housed in the cuddy cabin of the tow vessel. The functions of the electrical enclosure are to (1) systematically route signals from the sensor suite to the computational hardware, and from the computational hardware to the actuators; and (2) house power and safety electronics for the sensors. The detailed electrical routing diagram and a CAD rendering of the enclosure are shown in Figure 84.

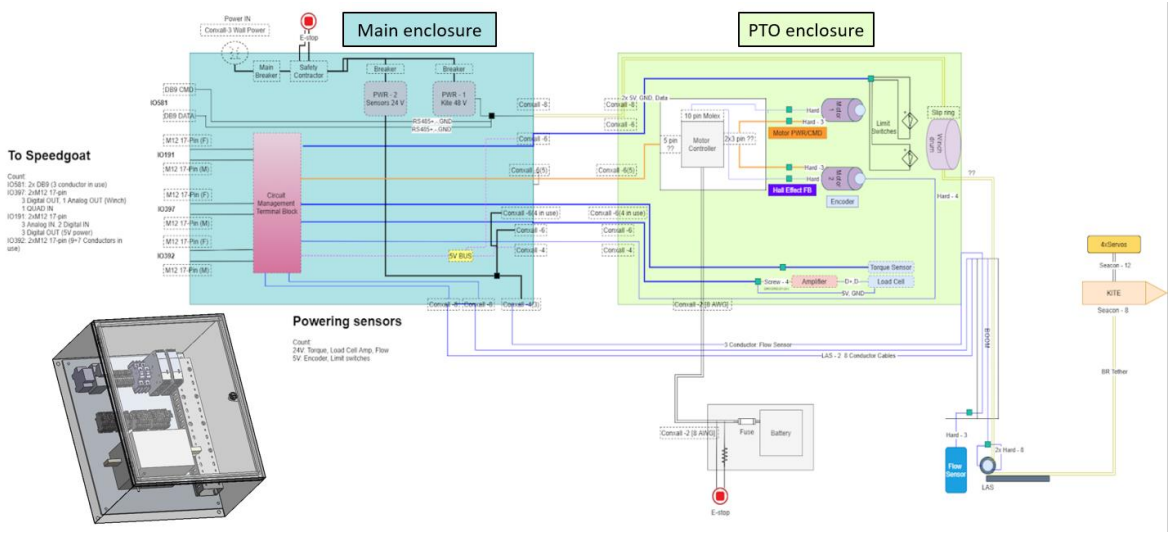

Figure 84: Electrical diagram for lake testing.

9.2 Experimental Design

The experimental methodology consisted of two layers:

1. Selection of the tow speed and spool speed combinations at which to characterize power output, for the purpose of characterizing a power surface;
2. Use of iterative learning control (ILC) to adapt (and ultimately optimize) figure-8 control parameters at each of the aforementioned combinations of tow speed and spooling speed.

Design of experiments for tow speed and spool speed selection: From commissioning tests conducted in November of 2021, tow speed resolution was known using the Privateer's built in Navionics system, measuring GPS speed over ground in 0.1 knot increments. Given the power output of the Privateer's outboard motors, lack of current, low windage, and vessel hydrodynamics, the minimum achievable speed was 2.0 knots or 1.03 m/s. The upper limit was defined as 4 knots or 2.06 m/s according to project milestone requirements. However, this upper limit was further curtailed to approximately 3.5 knots based on a tether tension limit of 400N. An experimental design space was created based on feasible tow and spool speed limits, 1.8 m/s and 0.5 m/s, respectively. Spool speed ratio is defined as $SSR = \omega R / v_{tow}$ and is used to normalize linear spool speed throughout the operating range of the winch. This creates a design space consisting of four variables: spool speed ratio in (SSR_{In}), spool speed ratio out (SSR_{Out}), tow speed (v_{tow}), and indicated power ($P_{Indicated}$).

With a target spool speed ratio resolution of 0.1, the potential range and number of experiments quickly became large, exceeding what is capable within the limited time frame of lake testing. The team's first round of testing (in November, 2021) revealed the need for substantial downtime allocations for data dumps, mechanical and/or software debugging, kite repair, and inclement weather. Therefore, steps were taken to narrow the realistic design space and efficiently sweep through enough data points to characterize a power surface model.

Simulation results indicated that the optimal spool in speed ratio was always contingent on the maximum linear spool speed that could be safely achieved. That is, a kite flying at steady level flight generates minimal drag, and with friction losses independent of the spool speed, spooling in rapidly under higher tension was advantageous as compared to longer periods of lower tension at slower spool speeds. Using this knowledge, the design space could be narrowed down to two design variables; spool-out speed ratio and tow speed. The next task was to identify potential experimental configurations and fit them within the experimental window. Given the 1-2 m/s tow speeds and 0-0.5 m/s linear spool speeds, the feasible design space was mapped and shown in Table 25, representing every configuration available under these conditions. Thanks to the iterative learning controller, which pushes the envelope of cross-current flight performance to maximize tension in the tether and thus induced power, we can be certain that after a series of consecutive spool cycles, an optimum will be reached and power production will stabilize at a maximum. Knowing tow and spool speed ranges, the tether length operating window of seven to twelve meters, and transition time between spooling events, time estimates for each experimental configuration could be tabulated. This information was used to create a daily schedule for lake experimentation.

Speed (m/s)	Speed (knots)	SSR In	SSR Out	Status
1.03	2.00	0.39	0.10	Completed
1.03	2.00	0.39	0.20	Completed
1.03	2.00	0.39	0.30	Completed

1.03	2.00	0.39	0.40	Completed
1.29	2.50	0.31	0.10	Completed
1.29	2.50	0.31	0.20	Completed
1.29	2.50	0.31	0.30	Completed
1.54	3.00	0.26	0.10	Completed
1.54	3.00	0.26	0.20	Completed
1.54	3.00	0.26	0.25	Completed
1.80	3.50	0.22	0.10	Completed
1.80	3.50	0.22	0.15	Completed
1.80	3.50	0.22	0.20	Completed
2.06	4.00	0.19	0.10	Not completed
2.06	4.00	0.19	0.15	Not completed
2.06	4.00	0.19	0.20	Not completed

Table 25: Experimental design space. Note that the tests at 4 knots were not completed due to the tether exceeding its mechanical limit at that point.

Notably, the highest anticipated tow speed of 4 knots could not be achieved due to overloading of the Blue Robotics Fathom Tether, as indicated by the control system's real-time display of tether tension. Post-processing of February, 2022's data revealed that, for spooling operation, the kite spent 756 minutes in the water while conducting power surface data acquisition. Another 366 minutes were spent on friction and drag studies and 436 minutes on investigative flight configurations, for a total of 1558 minutes, or nearly 26 hours of testing over the course of seven usable days.

Iterative learning control for optimizing flight parameters at each test point: In an attempt to find the optimal set of control parameters corresponding to each test case, we used a technique called iterative learning control. Iterative learning control (ILC) learns from previous repetitions of a task to inform future control decisions. To illustrate what iterative learning control is, picture a basketball player shooting free-throws. The cycles/iterations (where one cycle/iteration is one repetition of a task), are the basketball shots. The control input that the player uses, is their muscle movements. What the player learns from is how far off the shot is.

Our kite system performs repetitive operations (spooling cyclically as well as flying in figure-eight cycles). Using this cyclic behavior, we attempted to learn the optimal set of control parameters based on the kite's past performance. Traditional iterative learning control, shown in Figure 85, is used to optimize the tracking performance of a system. However, for our system, what we care about is not the tracking performance, but the cycle-averaged power production of the kite system. Because of this, we re-tailored the traditional iterative learning control formulation to optimize economic objectives (which for our case is cycle-averaged power production). A block diagram of this formulation is shown in Figure 86.

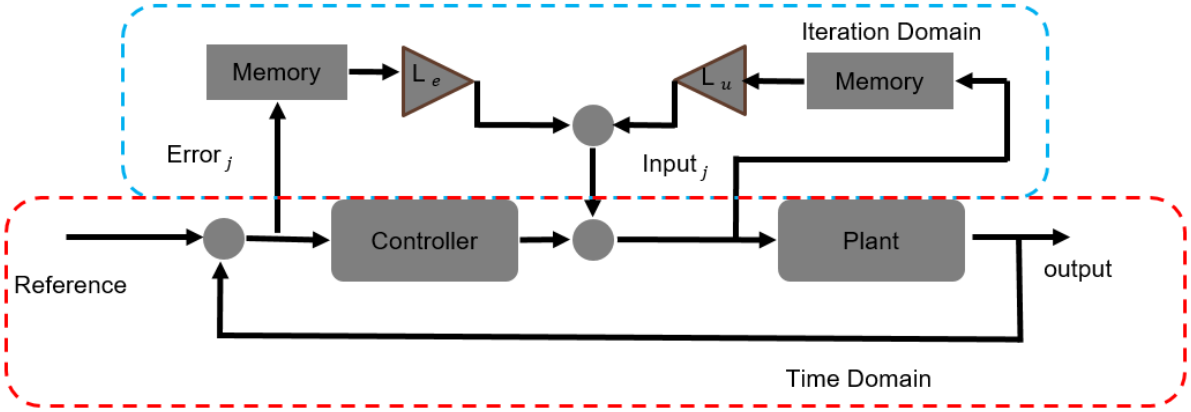

Figure 85: Traditional iterative learning control

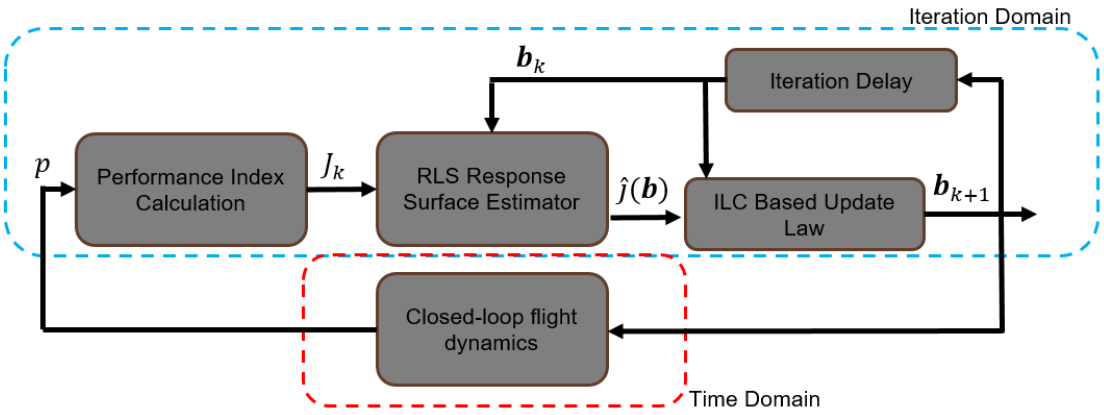

Figure 86: Economic iterative learning control

We performed an ILC optimization at each tow speed and spool speed combination. The control variables of interest were the roll amplitude, yaw amplitude, phase shift, period of the sinewave roll and yaw setpoints that the kite tracked during the spool-out portion of the cycle, as well as the elevator deflection of the kite during the spool-out portion of the spooling cycle. An example of how the optimization works can be seen graphically in Figure 87. The ILC uses a recursive-least-squares algorithm to fit a surface mapping the cycle-averaged power performance (exemplified by the surface in Figure 87) to the set of control parameters, which were the roll amplitude, yaw amplitude, phase shift etc. The ILC the uses a gradient based update law, of the form

$$\boldsymbol{b_{k+1}} = \boldsymbol{b}_k + K_e \nabla \hat{J}(\boldsymbol{b}_k) + \boldsymbol{P}_k$$

where $\boldsymbol{b_{k+1}}$ are the control parameters at the next trial, K_e is the learning gain, $\nabla \hat{J}(\boldsymbol{b}_k)$ is the estimate response surface, and $\boldsymbol{P}_k$ is a noise term to move the system out of local optimums and identify the response surface.

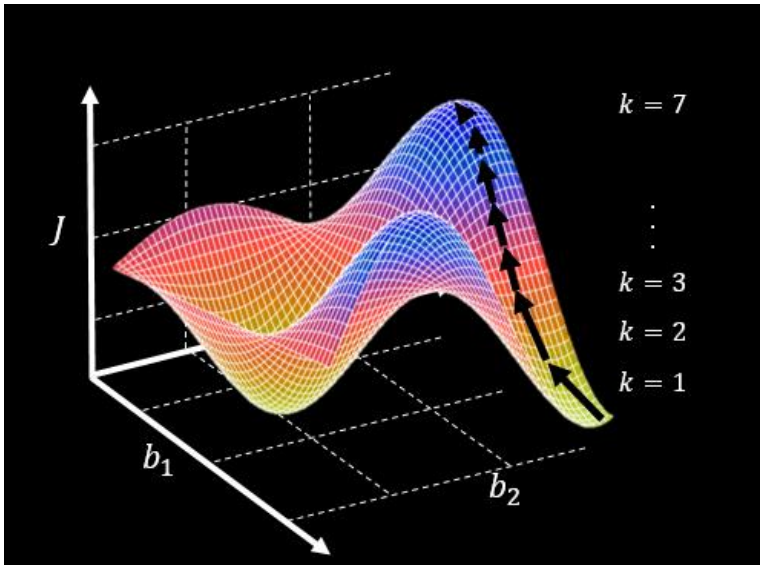

Figure 87: ILC optimization graphic

Using this formulation, at all of the different test cases, we were able to improve our cycle-averaged power performance greatly.

9.3 Power Surface and Time Series Data Analysis

Time series data, with comparison against simulation results: Figure 88 displays the time series data of a single spool out event at a tow speed of 1.00 m/s and a spool speed ratio of 0.1. Figure 89 shows the same plot zoomed in on 30 - 38 seconds for a closer inspection of the experimental vs. predicted data sets.

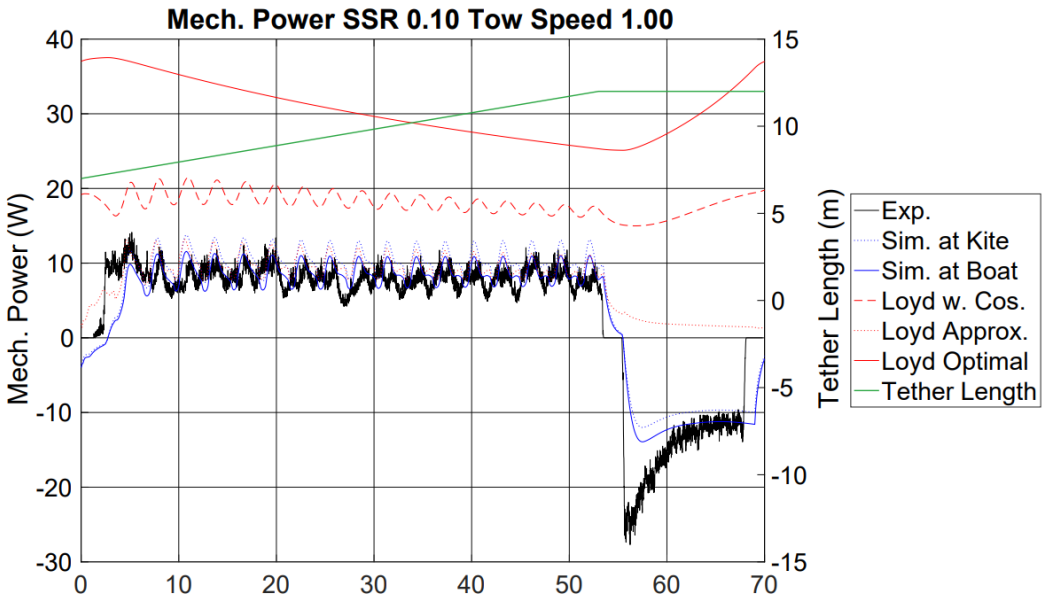

Figure 88: Time series results at a tow speed of 1 m/s and spool-out speed ratio of 0.1.

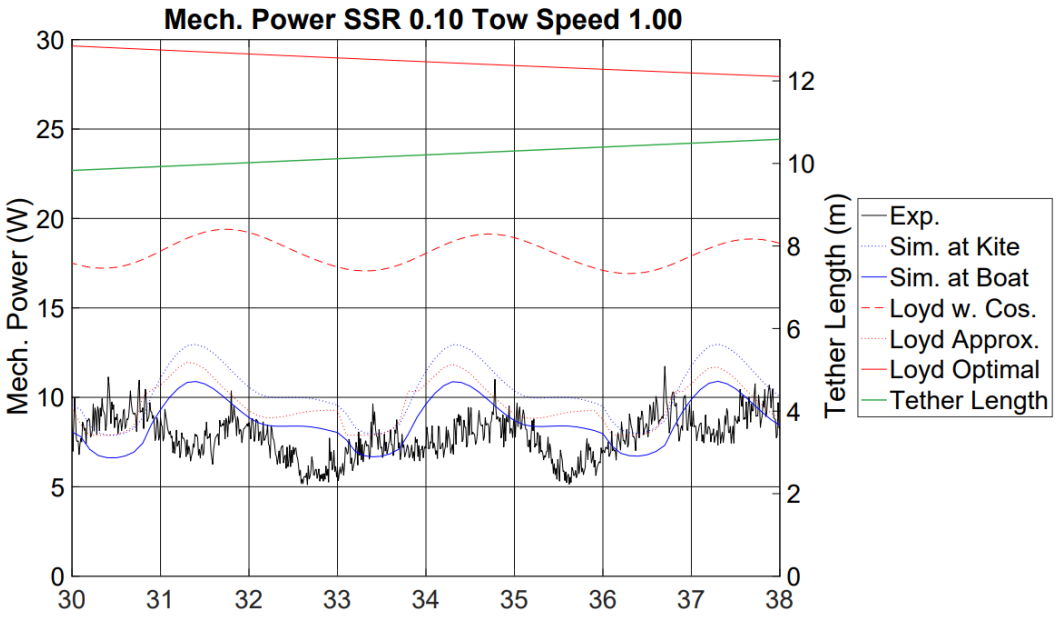

Figure 89: Zoomed in version of Figure 88.

Loyd Optimal power, shown in the solid red line, and is a function of maximum lift coefficient cubed over minimum drag coefficient squared, as given by the following equation:

$$P_{Loyd} = \frac{1}{2}\rho A \left(\frac{C_L^3}{C_D^2}\right)(V_T - V_S)^2 V_S$$

As time passes and the tether length increases, the lift coefficient of the kite remains constant; however, the drag coefficient increases, since the longer tether increases the drag reference area. For this reason, Loyd Optimal Power decreases with time.

The dashed red line builds on the aforementioned Loyd power equation by accounting for cosine losses from the azimuth and elevation angle as measured by the Line Angle Sensor relative to the incoming flow, shown in the equation below:

$$P_{Loyd,Cos} = \frac{1}{2}\rho A \left(\frac{C_L^3}{C_D^2}\right)(V_T \cos\theta \cos\phi - V_S)^2 V_S$$

As the tether length increases and the kite travels further from the Privateer, the magnitude of both azimuth and elevation angle decrease, causing the negative slope of this line to become less steep over time, as compared to Optimal Loyd Power. The increased tether length also slows the rate of change of each angle and, since cross current flight span is held constant, accounts for the attenuation in the amplitude of oscillation. The solid green line represents tether length and is shown to vary between seven and twelve meters as intended.

In Figure 90, a portion of the original plot has been expanded to show the remaining four trend lines with more precision. The unfiltered experimental signal is shown in black, while blue represents simulation predictions, before and after accounting for frictional losses, shown in dashed and solid, respectively. The simulation uses a quasi-steady dynamics-based approach to predict power, which, rather than relying on optimal C_L and C_D, relies upon achieved C_L and C_D, both of which never reach their optimal values. The

red dotted Loyd Power line represents the same equation as (3), but instead of using optimal C_L and C_D, it uses the simulation achieved C_L and C_D, creating the most accurate prediction of power from a Loyd derivation. While not perfect, the close alignment in magnitude, phase, and amplitude signify noteworthy accuracy in the model's predictive abilities.

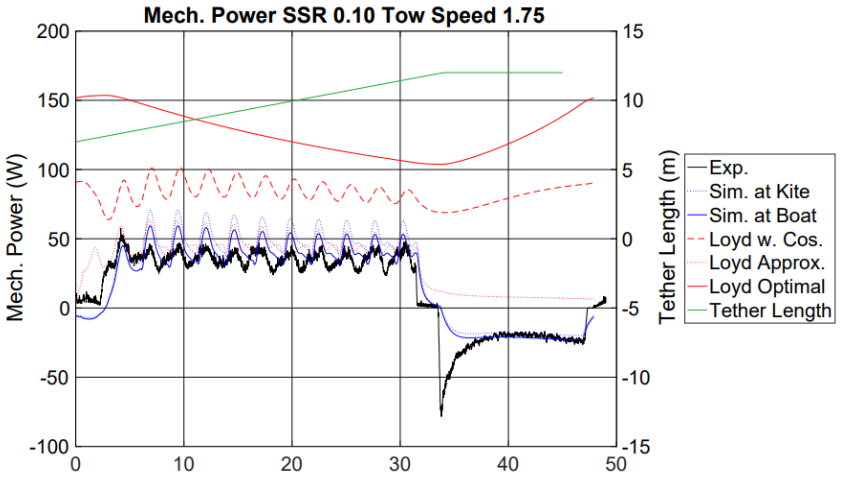

Figure 90: Time series results at a higher tow speed.

Note that even though the spool speed ratio is the same, the higher tow speed results in a faster linear spool speed, meaning the time required to spool out from 7 to 12 meters is lower, and fewer figure 8's are flown.

Power surface (aggregate) data analysis: When assessing the power surface, the team focused on two metrics: cycle-averaged power and spool-out power. Cycle-averaged power is computed over a full spool-out/spool-in cycle, whereas spool-out power is restricted to the spool-out power. Because the control efforts in this project were focused on figure-8 flight control parameters, the spool-out power is more reflective of control effectiveness; on the other hand, cycle-averaged power is an important indicator of the system's ability to ultimately generate net positive power. Accompanying the assessment of power is an assessment of cycle-averaged and spool-out-averaged tension (which, in combination with the spool rate, drives mechanical power output). Figure 91 provides the cycle-averaged power and tension surfaces, whereas Figure 92 provides the spool-out-averaged power and tension surfaces.

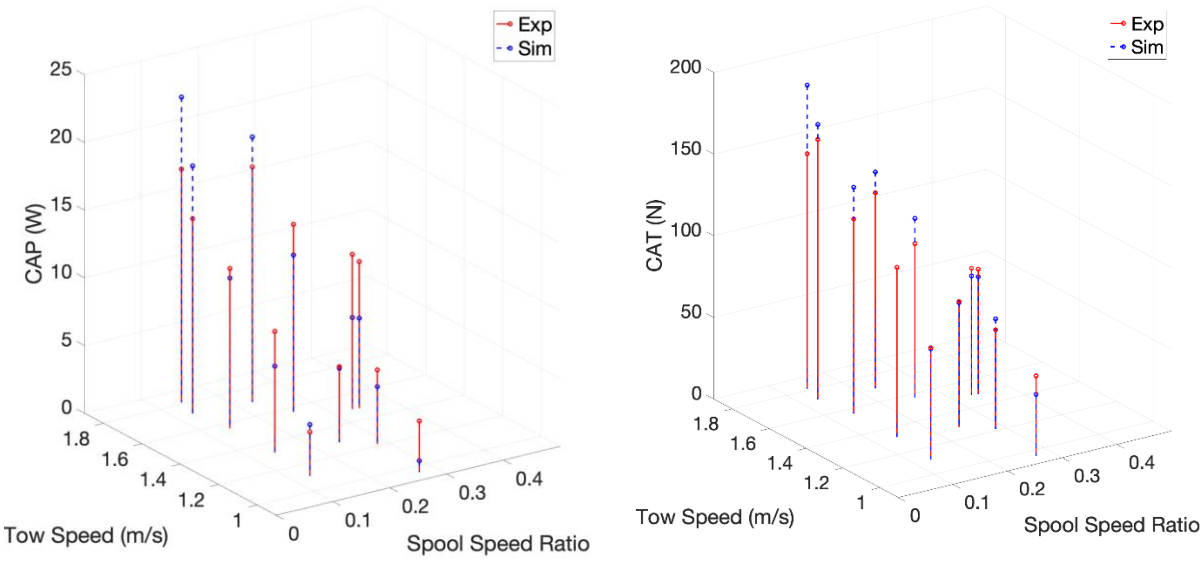

Figure 91: Cycle-averaged power and tension surfaces, with comparisons between experiments and simulations.

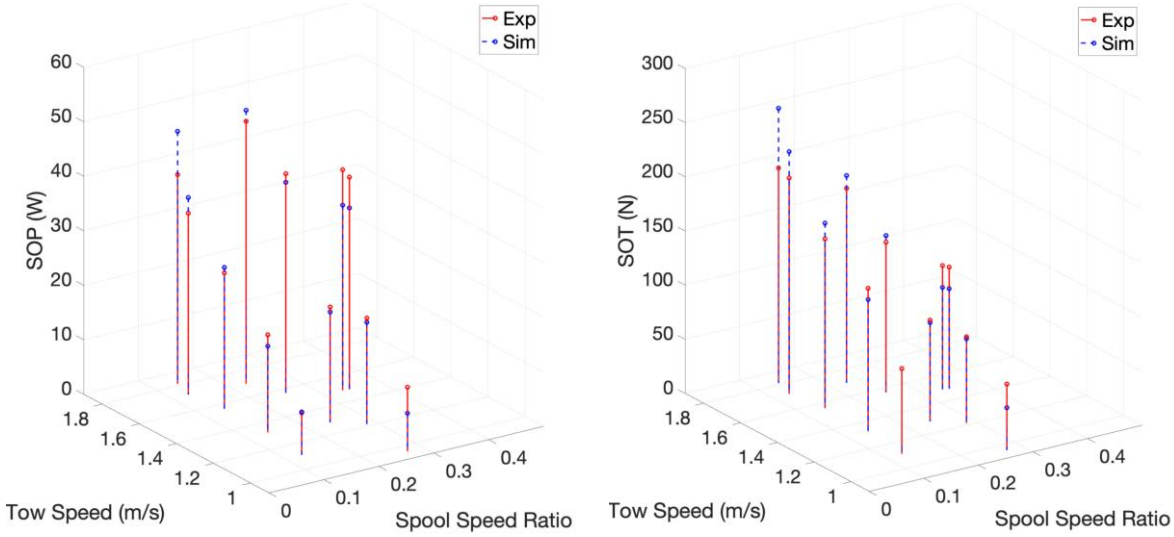

Figure 92: Spool-out-averaged power and tension surfaces, with comparisons between experiments and simulations.

Evidence of ILC efficacy: As noted earlier, ILC was run at every combination of tow speed and spool speed ratio to optimize the kite's flight control parameters. Figure 93 provides evidence of the efficacy of ILC, showing the progression of cycle-averaged power from the initial spool-out/spool-in cycle to the final (converged) result, along with "before and after" time traces.

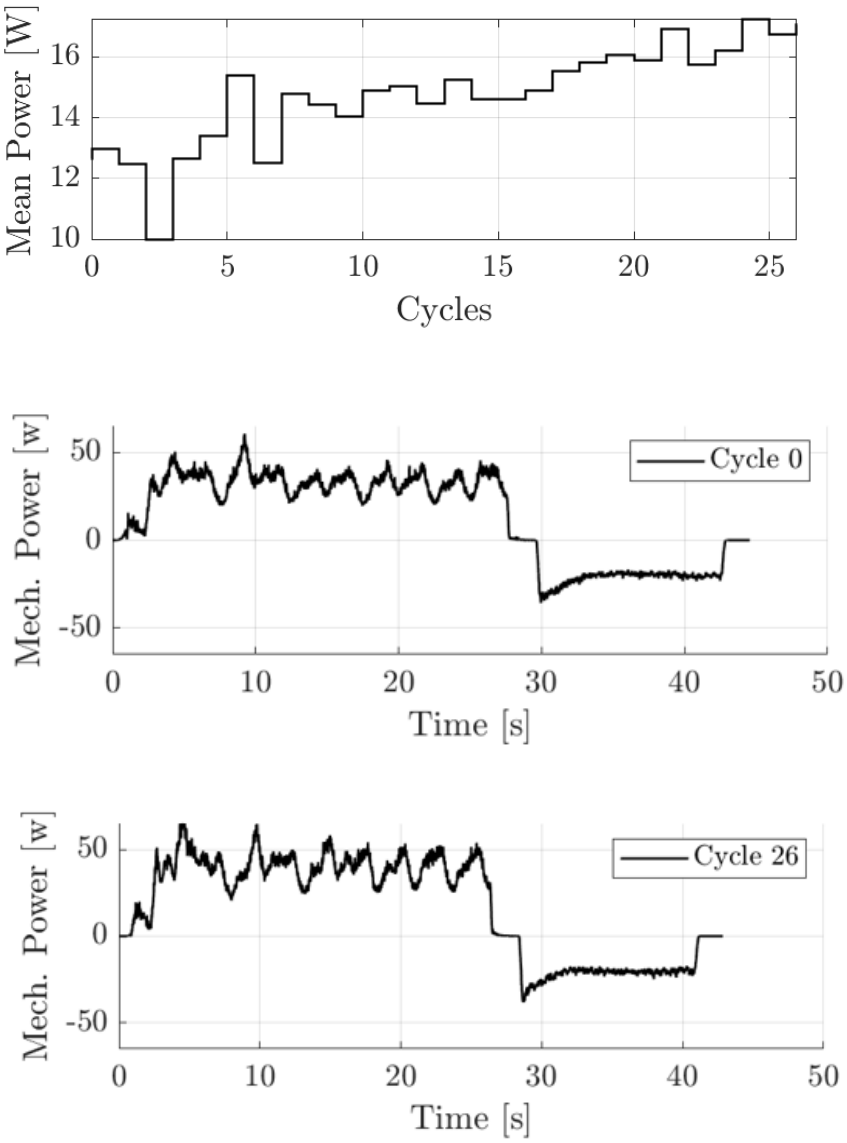

Figure 93: Select ILC results, corresponding to a 1.75 m/s tow speed. The top plot shows the progression of cycle-averaged power output, whereas the bottom two plots provide a "before and after" picture of the mechanical power time series.

9.4 Full-Scale Projections

The metrics under consideration for techno-economics were the power to mass ratio, the peak/cycle-averaged power, the capacity factor, and the levelized cost of energy. The original targets for budget period one were to have a power to mass ratio of 0.15 kW/kg at a rated flow speed of 2 m/s, a capacity factor of 60 percent or more, and a projected LCOE of $0.20/kWh or less. These targets were achieved at the end of budget period one for the 100 kW design. A second 200 kW design was also presented that that missed capacity factor targets but improved on the power/mass ratio and LCOE. These metrics for the previous 200 kW design as well as for an updated design will be shown at the end of this section. The end of project targets were to have a power to mass ratio of 0.2 kW/kg at a rated flow speed of 2 m/s, a capacity factor of 70 percent or more, and a projected LCOE of $0.15/kWh or less.

Since the end of budget period one, there have been improvements to the hydrodynamic characterization of the kite, as well as control improvements in the form of greatly improved path selection, and an angle of attack controller. The results presented at the end of budget period one considered only surface deployment (off floating platform). Results now consider both surface and seabed deployment. For seabed deployment, there exists a tradeoff between shallow depth/long tether/high flow operation and deep depth/short tether/low flow operation. Now, to generate the projections for techno-economic metrics a power surface is used, shown in Figure 94.

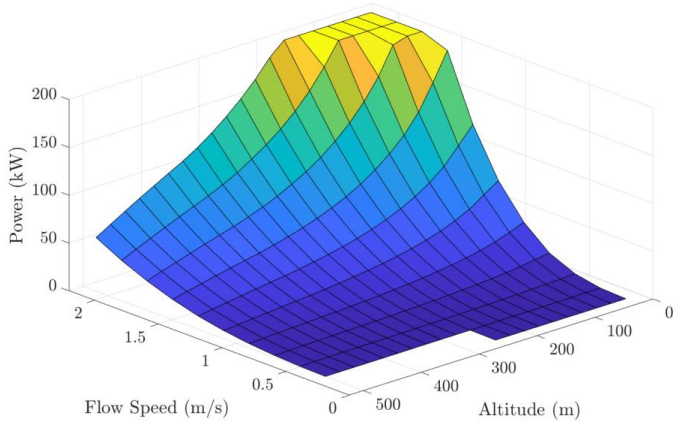

Figure 94: Power surface.

The power surface enables optimal depth selection, which was previously not available. As before candidate sites were investigated, shown below in Table 26.

	Coordinate	Depth (m)
Location 1	[35.138, -75.106]	222
Location 2	[35.133,-75.079]	271
Location 3	[35.138,-75.2106]	264
Location 4	[35.156,-75.134]	102

Table 26: Candidate locations

Additionally, a tidal site (Snipe Island, 60m seabed depth) was investigated. A summary of the results can be seen in Table 27 below.

Site	Surface or Seabed	LCOE ($/kWh) – Go/no-go	LCOE ($/kWh) – Updated	$P(2\frac{m}{s})$/mass – Go/no-go	$P(2\frac{m}{s})$/mass - Updated	Capacity factor (%) – Go/no-go	Capacity factor (%) – Updated
2	Surface	0.1191	0.0775	0.144	0.2767	40.32	61.41
3	Surface	0.1381	0.0828	0.144	0.2767	37.47	57.50
4	Surface	0.1594	0.0975	0.144	0.2767	30.11	48.84
1	Surface	0.1255	0.0806	0.144	0.2767	38.26	59.12
2	Seabed	N/A	0.1486	0.144	0.2767	N/A	32.30
3	Seabed	N/A	0.1352	0.144	0.2767	N/A	35.20
4	Seabed	N/A	0.1847	0.144	0.2767	N/A	21.58
1	Seabed	N/A	0.2207	0.144	0.2767	N/A	25.78

Table 27: Techno-economic metric results. Green indicates meeting end of project goal, orange indicated meeting budget period one goal, and red indicates missing goal.

The results of table two are for a 200 kW system. While the capacity factor targets are now quite achieved, they can be trivially satisfied by lowering the system's rated power to 100 kW. Large improvements in all of the metrics can be seen from the projections at the go/no-go point at the end of budget period one to now. Additionally, all of the surface deployments at the candidate locations achieve the LCOE and power to mass ratio targets. The results for deployment off of an existing Gulf Steam surface for a Blue Economy application can be seen in Table 28.

Site	Surface or Seabed	LCOE ($/kWh) – Go/no-go	LCOE ($/kWh) – Updated	$P(2\frac{m}{s})$/mass – Go/no-go	$P(2\frac{m}{s})$/mass - Updated	Capacity factor (%) – Go/no-go	Capacity factor (%) – Updated
2	Surface	0.1191	0.0662	0.144	0.2767	40.32	61.41
3	Surface	0.0980	0.0707	0.144	0.2767	47.37	57.50
4	Surface	0.1594	0.0832	0.144	0.2767	30.11	48.84
1	Surface	0.1255	0.0687	0.144	0.2767	38.26	59.12

Table 28: Techno-economic metric results for deployment off of an existing Gulf Steam surface for a Blue Economy application. Green indicates meeting end of project goal, orange indicated meeting budget period one goal, and red indicates missing goal.

As in Table 2, while the capacity factor targets are now quite achieved, they can be trivially satisfied by lowering the system's rated power to 100 kW. Additionally, in Table 3, it can be seen that the LCOE and power to mass ratio targets are achieved.

The results for a tidal deployment at Snipe Island can be seen in Table 29. While there are no requirements given by the SOPO for this site, it is interesting to see the techno-economic projections.

Surface or Seabed	LCOE ($/kWh) – Go/no-go	LCOE ($/kWh) – Updated	$P(2\frac{m}{s})$/mass – Go/no-go	$P(2\frac{m}{s})$/mass - Updated	Capacity factor (%) – Go/no-go	Capacity factor (%) – Updated
Seabed	0.1537	0.1103	0.144	0.2767	30.22	41.27

Table 29: Techno-economic metric results for Snipe Island Tidal site. Note that the initial scope of work did not focus on tidal installations; thus, no targets were set for this case.

10 Technology-to-Market Pipeline Development

10.1 Invention Disclosures

One of the primary needs in establishing a credible math toward the commercialization of our undersea kite technology is identifying the unique and valuable intellectual property (IP) emerging from this project. To that end, the team has been proactive in filing invention disclosures with the university through the project. The team has filed four invention disclosures, three of which are presently still under evaluation by the university, and one of which has proceeded to the point of the university filing a patent. These inventions are as follows:

- *Optimal Control Techniques for Spooling Phases of Undersea Kite Energy Generation (Patent filed under the title "Kite-Based Energy Generation Control Systems and Related Methods"):* This invention focuses on multi-cycle and intra-cycle spooling mechanisms for maximizing energy harvesting in spool-out/spool-in operation. The claims of the invention pertain both to the optimal control techniques and the unique control hardware configuration that renders these techniques possible.
- *Novel Experimental Towing Apparatus (invention disclosure under review by the university):* This invention focuses on the mechanical and electrical control hardware, along with the control algorithms, that make pool-based and open-water tow testing possible using the team's customized setup.
- *Systems and Methods for Kite-Based Energy Harvesting with Ultra-Long Tethers (invention disclosure under review by the university):* This invention focuses on control techniques, with and without the aid of supplemental tether fairings, for flight path and turbine control optimization in the presence of very long tethers that exhibit substantial curvature. The concept here is that, by isolating the motion of the tether to a very small fraction of the tether's length, the tether as a whole will experience a fraction of the drag (and associated power loss) that would be experienced with the whole tether moving. On very long tethers, where tether drag dominates kite drag, minimizing tether drag is of paramount importance, as is discussed further in the Lessons Learned section.
- *Active Wing Morphing of an Energy-Harvesting Kite (invention disclosure under review by the university):* This invention focuses on physical hardware and control methods for actively changing the geometry of a kite's wings as a function of the environmental conditions and tether length.

Both span-wise and chord-wise morphing strategies are considered. The ability to reconfigure the kite's geometry is important, since (i) greater structural loads at high flow speeds and low tether lengths demand reductions in wing area, and (ii) longer tether lengths render high lift more important than wing efficiency, since tether drag dominates, thereby demanding a different wing geometry than at lower tether lengths.

10.2 Publications

As a university-led team, one of the greatest ways to facilitate technology-to-market development is through dissemination of modeling tools and results to a wide audience. Not only has the team made all of its modeling and control code (developed in a MATLAB/Simulink environment) open-source via its GitHub repository; it has also published 22 peer-reviewed papers as a result of this project. These have been uploaded to the MHK Data Repository and are also listed at the PIs' lab websites and Google Scholar pages.

10.3 Manta Ray Program

Because the underwater kite technology can be classified as high-risk/high-reward, it is of great interest to seek out initial stakeholders who are willing to adopt this level of risk. The Department of Defense is one such stakeholder, possessing a significant interest in acquiring autonomous underwater vehicle (AUV) technology that can support long-duration missions with large payloads by periodically recharging the AUV using the ambient energy source. So interested is the Department of Defense in this capability that its Advanced Research Projects Agency (DARPA) created the Manta Ray program to pursue long-endurance, high-payload technologies in 2019 through its Manta Ray program.

Because of the ability of underwater kite technology to execute high-speed orbits many times faster than the prevailing flow, kites represent an ideal technology for harvesting energy in very limited current environments, even below 0.5 m/s. Furthermore, because defense missions are not designed around areas with the greatest current resource but are rather designed around what is strategically required, the use of technologies that can harvest limited flow resources is highly desirable. It is for this reason that the NC State team partnered successfully with Pacific Marine Technologies ("PacMar" Technologies) to develop a long-endurance AUV that periodically parks itself on the seabed and deploys an energy-harvesting kite to recharge its on-board batteries. The team is now in Phase 2 of this multi-year program and is scheduled to deploy a full-scale demonstration in a designated representative environment within the next year.

10.4 Discussions with Minesto

Finally, the team is engaged in periodic discussions with the leadership at Minesto, particularly with regard to the establishment of a North American entity and the development of kite technology for current energy harvesting applications, requiring very long tethers and therefore deviating from the current DeepGreen and Dragon Class technologies from Minesto, which are targeted at shallower tidal environments.

11 Lessons Learned

11.1 Regarding the Benefits and Limitations of Scaled Testing

One of the hallmarks of the testing campaign pursued in this project was its progressive nature. Water channel experiments provided an inexpensive means of validating flight dynamic behavior, whereas pool-based tow testing provided a highly accessible means of validating and refining the control system prior to proceeding to the open-water, in spite of the limited available tow length. It was also understood at the outset of the project that the earlier, smaller-scale test facilities had limitations. It would be impossible to instrument the 3D printed water channel-scale models with control surfaces, and the pool testing tow length would not enable iterative learning, at least in a continuous sense.

While many of the limitations of earlier rounds of testing were recognized, some were overlooked at the outset of the project but recognized when testing got underway. For water channel testing, not only is it impossible to replicate the control mechanisms found at larger scales, but it is also impossible to replicate anywhere near the level of cross-current flight performance that can be achieved at larger scales. This arises because of (i) the dimensional constraints of the water channel, (ii) the bandwidth limitations of the DC motor actuators for the tethers, and (iii) the Reynolds number limits of the water channel (while this last factor was recognized at the outset of the project, it was only when this factor was combined with the first two that the full extent of the performance limitations were recognized). The consequence of this limitation was that, while the water channel provided a means of confirming the accuracy of the team's dynamic model, it did not do so in a particularly representative environment, leading to a risk that the model refinements made based on water channel testing alone would result in good agreement between the model and date in the water channel but poor agreement at larger scales. In short, this means that while the water channel is a valuable tool for initial verification of the model's predictions, it alone cannot be used to gain full confidence in the predictive capabilities of the model. At the tow testing scale (both in pool testing and open-water testing), it was anticipated that the 1/10-scale model would replicate (at scale) full-scale behavior. While the 1/10-scale model indeed came much closer than the water channel models in reflecting full-scale behavior, and serves as a much more solid platform for model validation, the model's size constraints required sacrifices to the outer mold line that made it less hydrodynamically efficient than a full-scale system. In particular, in order to accommodate the on-board control electronics, an enlarged cylindrical fuselage was used, which carried a higher drag coefficient than the full-scale fuselage. Through follow-on funding, the team will be pursuing 3/8-scale testing in the winter, which will enable the characterization of a kite with an accurate outer mold line in more representative conditions to a full-scale deployment. It is important to note that the water channel tests and 1/10-scale tests represented very important de-risking steps toward pursuing 3/8-scale testing, as the latter stage of testing enables characterization in a more representative environment but also provides less flexibility (in terms of accessing the test site, test vessel availability, and personnel availability).

11.2 Regarding the Profound Implications of Tether Drag and Mitigation Thereof

The team's multi-link tether model has always provided the capability of considering tether drag when simulating the kite's dynamics. What the team did not realize at the outset of the project, however, was how significant the implications of tether drag would be. In particular, the team focused its attention on the use of Dyneema for the tether, initially assuming a safety factor just greater than one. After discussing tether design and safety factors with several vendors (e.g., Linden), it was found that a more typical safety factor used in marine applications is on the order of **6** (although numbers from several airborne wind

energy companies imply safety factors between 2 and 3). Such a high safety factor drives up (significantly) the required tether diameter, making operation on long tethers challenging, even if they are faired (though completely faired tethers are generally not possible to operate in spool-out/spool-in operation). It is important to note that the implications of tether drag are much more pronounced in underwater kites than in the sister technology of airborne wind energy systems. This is because of the stark density differences, which mean that the same amount of power is available at a lower flow speed (and therefore a lower spooling speed) in water than in air. Because mechanical power is equal to the product of spooling speed and tension, this implies a higher tension in water than air (typically an order of magnitude larger), thereby demanding a much greater tether diameter.

Because tether drag is such an important consideration for long tether lengths, the team has undertaken several measures to quantify the impact of tether drag and mitigate it:

Investigation of vortex-induced-vibrations ("strumming") via water channel experiments: As is detailed at length in Section 6.3, controlled motion experiments in the water channel not only involved the kite, as proposed in the original project plan, but also a characterization of the tether. This was for the specific purpose of identifying "lock-in" frequency, in addition to other frequencies at which strumming would contribute a marked increase in tether drag beyond the drag coefficient of 1 expected from a cylinder perpendicular to (a component of) the flow.

Investigation of morphing kite strategies for variable-length tether operation: When the tether length varies, the drag coefficient contributed by the tether, referenced to the kite's fixed wing area, varies as well. That means that the relative contribution of tether drag to total drag changes from a small value at low tether lengths to a large value at high tether lengths. The consequence of this is that the optimal wing geometries at those two tether lengths differ. At low tether lengths, a highly efficient wing is desirable. However, at long tether lengths, maximization of wing lift (at the expense of wing drag) is paramount, since tether drag plays a dominant relative role. The team investigated chord-wise morphing strategies for maximizing power in variable tether lengths, simulating the performance of a chord-wise morphing kite using the Mid-Atlantic Bight, South Atlantic Bight (MAB-SAB) Regional Ocean Model. Results in Figure 95 (left) show a marked improvement as a result of chord-wise morphing. Further details regarding the methodology and results for online morphing are provided in [22] for an airborne wind energy system. A publication discussing morphing for an underwater kite is under review at the time of this report.

Investigation of control strategies for tether motion isolation: In addition to actively morphing the kite geometry in variable-length tether operation, one can dramatically decrease the influence of tether drag in fixed (long)-length tethers through careful path optimization. In particular, the team examined path optimization techniques that minimize the *effective tether length*, i.e., the length of tether that, if perfectly straight, would yield the same drag coefficient as the curved tether. This strategy is essentially equivalent to finding flight paths that keep the majority of the tether stationary and therefore unaffected by drag. Figure 95 (right) shows the result of an optimized flight path for minimizing effective tether length, as compared with a baseline flight path. Further details regarding the underlying mathematics pertaining to effective tether length, along with additional insights, are available at [23].

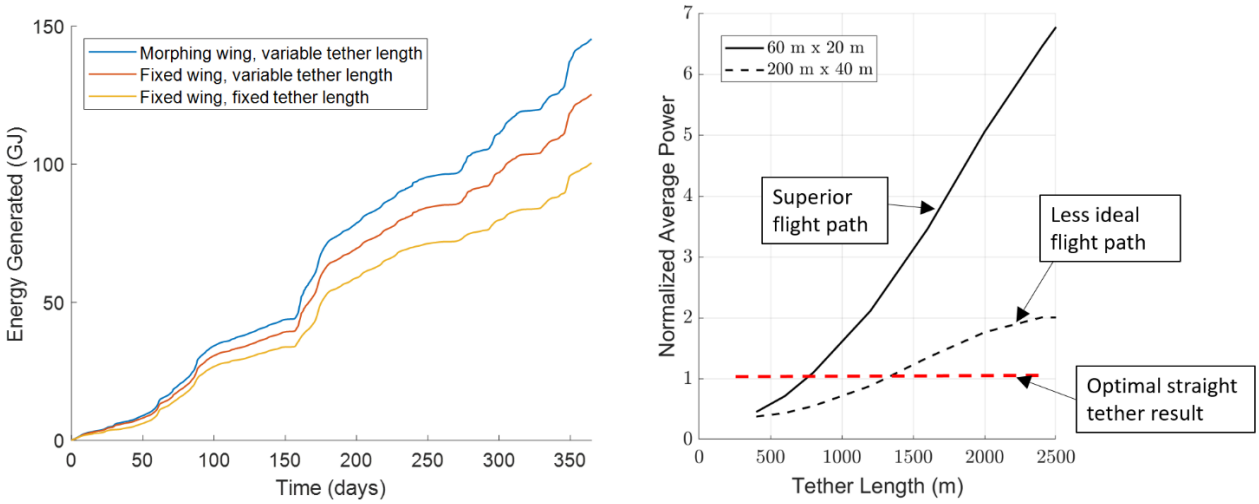

Figure 95: Preliminary simulations of performance sensitivity to (i) morphing based on the MAB-SAB model (left) and (ii) flight path parameters (right – dimensions in legend specify the figure-8 width and height; power is normalized by the straight-tether theoretical maximum) for >400m tether operation.

11.3 Regarding Generator Conversion Efficiencies in Cyclic Spooling Operation

One of the most significant observations from lake-based tow testing was the stark difference between observed mechanical and electrical power. While the team always generated net positive mechanical power and sometimes generated net positive electrical power, it also performed several tests where net electrical power was negative. It is important to identify the sources of these conversion efficiency losses prior to moving forward with product and control system design, and this sub-section aims to address this.

Previous analysis by the University of Maryland (UMD) showed that mechanical power at the power take-off (PTO) motor's shaft (i.e., with mechanical friction losses accounted for) can be used as a surrogate for electrical power in the PTO system. Laboratory hardware-in-loop experiments showed that there was significant discrepancy between the mechanical measured at the spool (as opposed to the motor shaft) and electrical power for a scaled representative (optimized in previous studies) spooling trajectory (Figure 96). Both power signals were integrated over time, and the discrepancy persisted: for an average mechanical power of 15.33W, only 0.16W of average electrical power was produced (Figure 97).

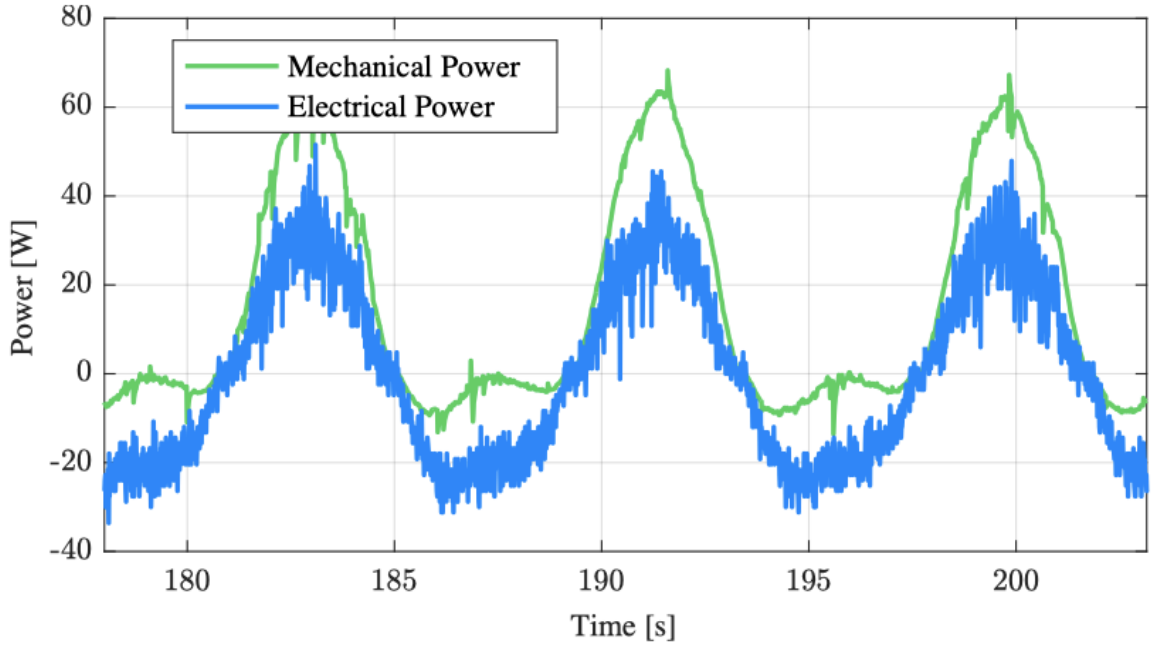

Figure 96: Measured spooling mechanical power and electrical power of PTO during three periods

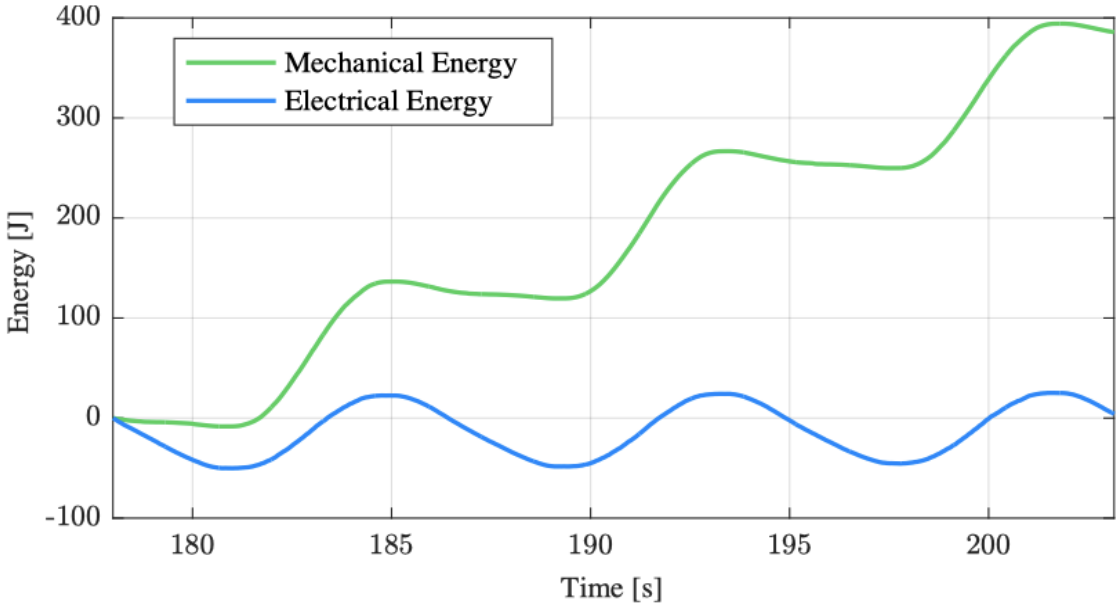

Figure 97: Generated mechanical and electrical energy during three periods

To understand the cause of the power loss (difference between spooling mechanical and electrical power), a simple relationship, as seen in the equation below, was fitted to this loss. The mechanical loss was approximated as the rotor speed squared, and the electrical loss was approximated as the square of the armature current. Here, R is the armature resistance, and b is an effective damping coefficient. The

power loss fit allows us to predict electrical power (at the PTO setup's battery) very accurately from measurements of spooling mechanical power, armature current, and motor/generator speed.

$$P_{loss} = ||P_{mech} - P_{elec}|| = Ri^2 + b$$

Parameter identification for the armature resistance and damping coefficient makes it clear that the main reason for the discrepancy between spooling mechanical power versus electrical power is mechanical friction in the PTO setup, and not motor/generator resistance. Therefore, mechanical power *at the motor* can be a useful surrogate for electrical power in MHK optimization work.

	Parameter Estimate	Contribution 3 parameter
Armature Resistance	4.949Ω	0.15Ω
Damping Coefficient	$5.741 \times 10^{-4}\mathrm{N\,m\,rad^{-1}\,s}$	$1.0 \times 10^{-4}\mathrm{N\,m\,A^{-1}}$
Motor Constant	$0.256\mathrm{N\,m\,A^{-1}}$	$0.0838\mathrm{N\,m\,A^{-1}}$

Table 30: Parameter identification results

A similar analysis was carried out using data from the lake tests. Raw data showed that there are still discrepancies between the spooling mechanical power versus harvested electrical power and that the mechanical loss is partially governed by the changing tether length, as seen in Figure 98.

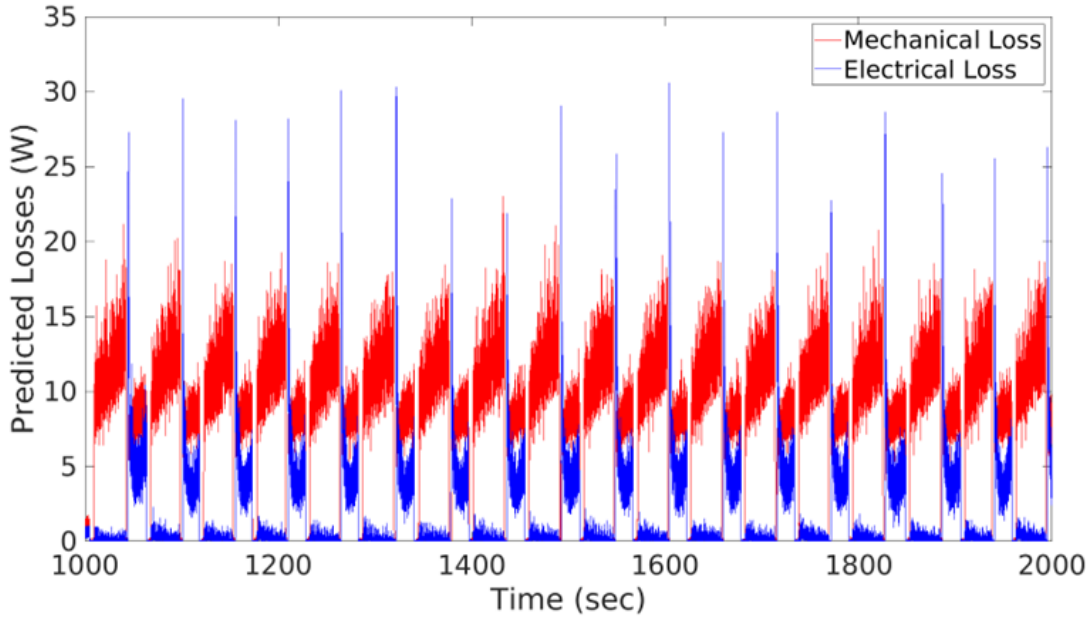

Figure 98: Predicted mechanical and electrical loss over time

The regression equation used for the lake test analysis takes the following form, where y and $\hat{y}$ are the real and estimated power loss, respectively. Mechanical power loss is now a function of the rotor speed and the length of the tether.

$$y = P_{tether} - P_{battery}$$

$$\hat{y} = P_{mech} + P_{elec}$$
$$P_{mech} = \theta_1\omega_{out}^2 + \theta_2 l\omega_{out}^2 + \theta_3\omega_{in}^2 + \theta_4 l\omega_{in}^2$$
$$P_{electrical} = \theta_5 i^2$$
$$P_{battery} = Vi$$
$$P_{tether} = T\dot{r}$$

The analysis showed that the real and predicted loss followed each other quite closely – see Figure 99. The analysis also showed that there was a 82% correlation between the estimated and measured power losses. Figure 100 illustrates this correlation, with the loops in the figure most likely caused by unmodeled dynamics.

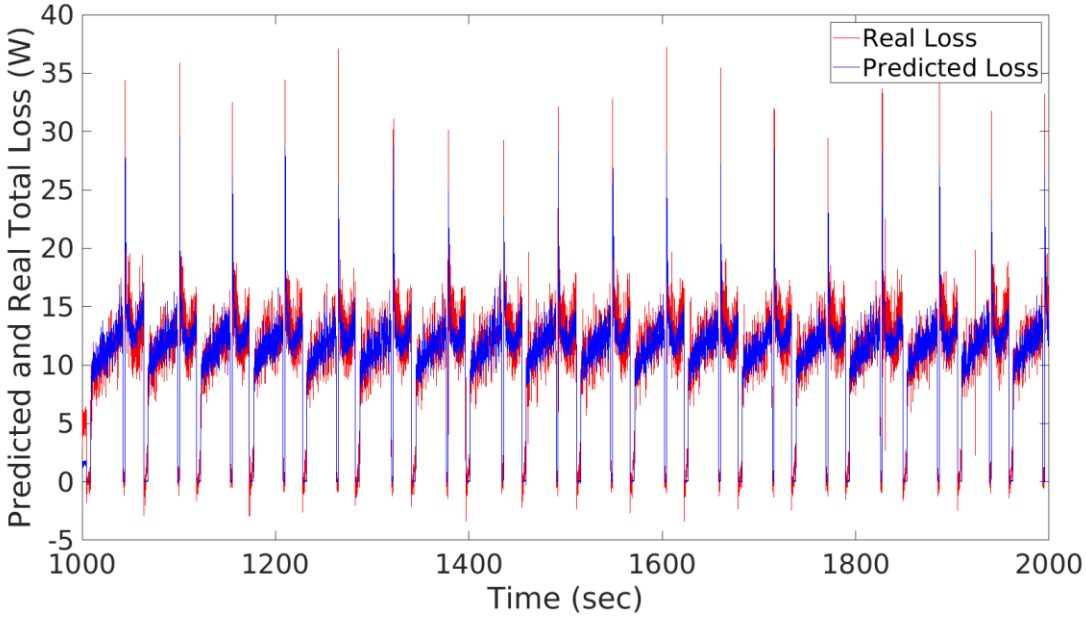

Figure 99: Real and predicted total loss over time

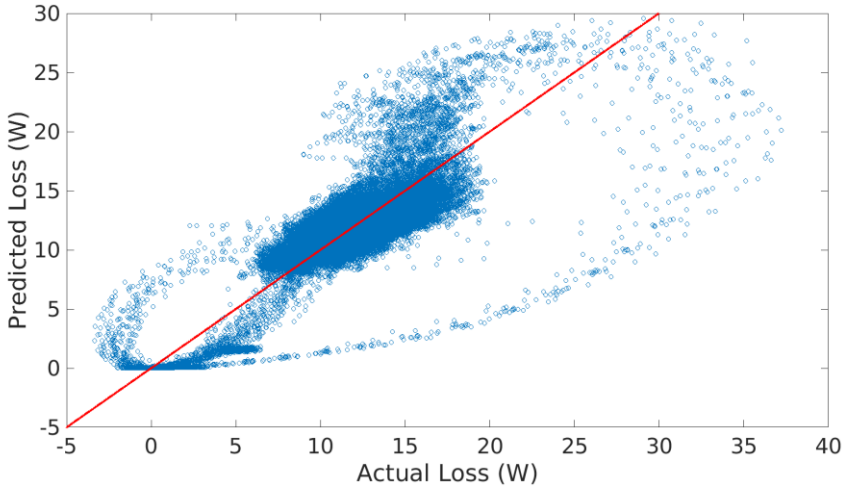

Figure 100: Linear regression fit for predicted and actual loss

The data set used for the above analysis corresponded to lower tension values, on the order of 40N during reel-in and 120N during reel out. With these lower tension values, raw mechanical power at the spool is

on the order of 20 Watts or so. For this particular set of lake test results, the estimates of mechanical and electrical power loss suggest that the NC State team's improvements in the PTO design were successful in reducing mechanical losses by 25-50% compared to the earlier/first PTO prototype built at UMD.

The team has submitted some of the above results as a peer-reviewed paper, accepted for presentation in MECC 2022 [24]. To summarize the team's findings to date regarding discrepancies between mechanical and electrical power:

1. The team's results, from both benchtop PTO testing and lake testing, show that there is a significant difference between mechanical power *as measured at the spool* versus electrical power *at measured at the battery connected to the PTO system*.
2. The above discrepancy – or power loss – can be accurately captured using a simple model that treats it as a quadratic power loss due to a combination of mechanical friction and electrical impedance effects.
3. The above modeling/fitting work shows that the majority of power losses occur due to mechanical friction, as opposed to electrical impedance. This is true for both the benchtop PTO tests and the lake tests.
4. Therefore, mechanical power *at the electric motor's shaft (without gearing)* is a reasonable representative for electrical power, and can be legitimately used for trajectory analysis/optimization.
5. The team's effort to reduce mechanical friction in the lake test setup at NC State, compared to the benchtop PTO setup at UMD, appear to have been successful in cutting 25-50% of mechanical friction effects.
6. Examining the above insights from the perspective of scalability provides a strong motivation for the use of direct-drive electric machines (as opposed to geared brushless DC motors) as this MHK technology is scaled to larger and larger scales.

12 Conclusions

This project has led to the development of open-source dynamic models, designs, and controllers for energy-harvesting underwater kites, all of which have been experimentally validated at multiple scales. While the research effort has focused on cyclic spooling operation as the mechanism for energy generation, the tools developed are also applicable to systems with on-board rotors. To the best of the team's knowledge, this represents the most comprehensive underwater kite modeling, design, control, and validation effort that has taken place in the United States in a way that has resulted in entirely open-source designs and models that can be used widely across the marine energy community.

Through this project, the team has established several follow-on activities, based on the connections made as a result of the research effort and the lessons learned. First, the team has continued its kite development through the DARPA Manta Ray program, partnering with PacMar Technologies in the development of an underwater kite for powering a long-duration, high-payload AUV. Second, the team has engaged in periodic discussions with Minesto regarding potential North American partnerships. Third, as a result of identified efficiencies associated with electromechanical conversion, the team has identified higher-efficiency conversion strategies for spooling operation and has also begun to investigate fully mechanical paths for using cyclically harvested energy to serve on-site needs such as desalination.

13 References

[1] V. Neary, M. Previsic, R. Jepsen, M. Lawson, Y. Yu, A. Copping, A. Fontaine, K. Hallett and D. Murray, "Methodology for Design and Economic Analysis of Marine Energy Conversion (MEC) Technologies," Sandia National Laboratories, Albuquerque, NM, 2014.

[2] M. Cobb, N. Deodhar and C. Vermillion, "Lab-scale experimental characterization and dynamic scaling assessment for closed-loop crosswind flight of airborne wind energy systems," *ASME Journal of Dynamic Systems, Measurement, and Control,* vol. 140, no. 7, 2018.

[3] C. Vermillion, M. Cobb, L. Fagiano, R. Leuthold, M. Diehl, R. Smith, T. Wood, S. Rapp, R. Schmehl, D. Olinger and M. Demetriou, "Electricity in the air: Insights from two decades of advanced control research and experimental flight testing of airborne wind energy systems," *Annual Reviews in Control,* vol. 52, pp. 330-357, 2021.

[4] N. Deodhar, A. Bafandeh, J. Deese, B. Smith, T. Muyimbwa and C. Vermillion, "Laboratory-scale flight characterization of a multitethered aerostat for wind energy generation," *AIAA Journal,* vol. 55, no. 6, pp. 1823-1832, 2017.

[5] P. Pyakurel, J. VanZwieten, M. Dhanak and N. Xiros, "Numerical modeling of turbulence and its effect on ocean current turbines," *International Journal of Marine Energy,* vol. 17, 2017.

[6] D. Bull and P. Jacob, "Methodology for creating non-axisymmetric WECs to screen mooring designs using a Morison equation approach," in *Oceans 2012*, 2012.

[7] J. Reed, M. Cobb, J. Daniels, A. Siddiqui, M. Muglia and C. Vermillion, "Hierarchical control design and performance assessment of an ocean kite in a turbulent flow environment," in *IFAC World Congress*, 2020.

[8] J. Reed, M. Muglia, M. Cobb and C. Vermillion, "Dynamic Characterization, Flow Modeling, and Hierarchical Control of an Energy-Harvesting Underwater Kite in Realistic Ocean Conditions," *International Marine Energy Journal,* 2023.

[9] K. Naik, S. Beknalkar, A. Mazzoleni and C. Vermillion, "Fused geometric, structural, and control co-design framework for an energy-harvesting ocean kite," in *American Control Conference*, 2021.

[10] K. Naik, S. Beknalkar, J. Reed, A. Mazzoleni, H. Fathy and C. Vermillion, "Pareto Optimal and Dual-Objective Geometric and Structural Design of an Underwater Kite for Closed-Loop Flight Performance," *ASME Journal of Dynamic Systems, Measurement, and Control,* vol. 145, no. 1, 2022.

[11] J. Reed, J. Daniels, A. Siddiqui, M. Cobb and C. Vermillion, "Optimal exploration and charging for an autonomous underwater vehicle with energy-harvesting kite," *American Control Conference (ACC). IEEE,* p. 4134–4139, 2020.

[12] S. Rapp, R. Schmehl, E. Oland, S. Smidt, T. Haas and J. Meyers, "A Modular Control Architecture for Airborne Wind Energy Systems," *AIAA SciTech,* p. 1419, 2019.

[13] M. Cobb, J. Reed, M. Wu, K. Mishra, K. Barton and C. Vermillion, "Flexible-time receding horizon iterative learning control with application to marine hydrokinetic energy systems," *IEEE Transactions on Control Systems Technology,* vol. 30, no. 6, pp. 2767-2774, 2022.

[14] M. Cobb, J. Reed, J. Daniels, A. Siddiqui, M. Wu, H. Fathy, K. Barton and C. Vermillion, "Iterative learning-based path optimization with application to marine hydrokinetic energy systems," *IEEE Transactions on Control Systems Technology,* vol. 30, no. 2, pp. 639-653, 2021.

[15] M. Cobb, K. Barton, H. Fathy and C. Vermillion, "An iterative learning approach for online flight path optimization for tethered energy systems undergoing cyclic spooling motion," in *American Control Conference*, Philadelphia, PA, 2019.

[16] J. Daniels, J. Reed, M. Cobb, A. Siddiqui and C. Vermillion, "Optimal cyclic spooling control for kite-based energy systems," in *IFAC World Congress*, 2020.

[17] M. Muglia, H. Seim and P. Taylor, "Gulf Stream Marine Hydrokinetic Energy Off Cape Hatteras, North Carolina," *Marine Technology Society Journal,* vol. 54, no. 6, pp. 24-36, 2020.

[18] A. Siddiqui, K. Naik, M. Cobb, K. Granlund and C. Vermillion, "Lab-scale, closed-loop experimental characterization, model refinement, and validation of a hydrokinetic energy-harvesting kite," *ASME Journal of Dynamic Systems, Measurement, and Control,* vol. 142, no. 11, 2020.

[19] A. Abney, J. Reed, K. Naik, S. Bryant, D. Herbert, Z. Leonard, A. Vadlamannati, M. Mook, S. Beknalkar, M. Alvarez, K. Granlund, M. Bryant, A. Mazzoleni, H. Fathy and C. Vermillion, "Autonomous Closed-Loop Experimental Characterization and Dynamic Model Validation of a Scaled Underwater Kite," *ASME Journal of Dynamic Systems, Measurement, and Control,* vol. 144, no. 7, 2022.

[20] Z. Leonard, S. Bryant, K. Naik, A. Abney, D. Herbert, H. Fathy, K. Granlund, A. Mazzoleni, M. Bryant and C. Vermillion, "Sensor Fusion Observer Design and Experimental Validation for an Underwater Kite," in *American Control Conference*, Atlanta, GA, 2022.

[21] J. Reed, A. Abney, K. Mishra, K. Naik, E. Perkins and C. Vermillion, "Stability and Performance of an Undersea Kite Operating in a Turbulent Flow Field," *IEEE Transactions on Control Systems Technology - accepted,* 2023.

[22] J. Fine, J. Reed, K. Naik and C. Vermillion, "Predictive Control of a Morphing Energy-Harvesting Kite," in *IEEE Conference on Control Technology and Applications*, Trieste, Italy, 2022.

[23] A. Abney and C. Vermillion, "Drag-Mitigating Dynamic Flight Path Design for an Ultra-Long Tether Underwater Kite," in *Modeling, Estimation, and Control Conference*, Jersey City, NJ, 2022.

[24] M. Alvarez Tiburcio, B. Debapriya, K. Behzad and H. Fathy, "Laboratory Simulation of Electricity Harvesting from an Underwater Kite," in *Modeling, Estimation, and Control Conference*, Jersey City, NJ, 2022.